UNIVERSITY OF Southampton

University of Southampton Research Repository
ePrints Soton

Copyright © and Moral Rights for this thesis are retained by the author and/or other copyright owners. A copy can be downloaded for personal non-commercial research or study, without prior permission or charge. This thesis cannot be reproduced or quoted extensively from without first obtaining permission in writing from the copyright holder/s. The content must not be changed in any way or sold commercially in any format or medium without the formal permission of the copyright holders.

When referring to this work, full bibliographic details including the author, title, awarding institution and date of the thesis must be given e.g.

AUTHOR (year of submission) "Full thesis title", University of Southampton, name of the University School or Department, PhD Thesis, pagination

http://eprints.soton.ac.uk

UNIVERSITY OF SOUTHAMPTON

Vertical Structure of Propagating Features

by

Aazani Mujahid

A thesis submitted in partial fulfillment for the degree of Doctor of Philosophy

in the
Faculty of Engineering, Science and Mathematics
School of Ocean & Earth Science

June 2010

UNIVERSITY OF SOUTHAMPTON

ABSTRACT

FACULTY OF ENGINEERING, SCIENCE AND MATHEMATICS
SCHOOL OF OCEAN & EARTH SCIENCE

Doctor of Philosophy

Vertical Structure of Propagating Features by Aazani Mujahid

The inter- and intra-annual variability of the western boundary North Atlantic 26.5 °N region has been central in the observations of the strength and structure of the Atlantic Meridional Overturning Circulation (AMOC). Interest in this work began when some recent work estimated the inter-annual fluctuations of the AMOC at 26.5 °N to be up to 3 Sv, and with a 25% reduction in strength over the last 50 years. There was increased need to understand both the short and long-term changes in the region and the responsible mechanisms for its variability. With the unique use of *RAPID-MOC* and *MOCHA* transatlantic mooring array in combination with satellite altimetry and transatlantic hydrographic observations, we find evidence that a significant amount of the variability can be accounted for by various mechanisms on different time-space scales including propagating features. Here we present simultaneous assimilation of surface and sub-surface observations that shows fresh insights into the contribution of the propagating features in the vertical structure of the temporal-spatial evolution in the western boundary 26.5 °N Atlantic. There is great prospect in using altimetry observations to reflect and infer the variability throughout the water-column - an effort vital in future interpretations of the AMOC fluctuations using altimetry and numerical models.

Contents

Page

List of Figures **vii**

List of Tables **x**

Acronyms **xi**

Declaration **xiv**

Acknowledgements **xvi**

1 Introduction **1**
1.1 Background 1
1.2 Outline of thesis 10

2 Dataset and Methods **13**
2.1 Introduction 13
2.2 Surface Satellite Datasets 14
2.3 Sub-Surface Dataset 15
2.3.1 The RAPID-MOC, MOCHA and Historical Arrays 15
2.3.2 Florida Straits Transport Datasets 25
2.4 Initial Recovery, Editing & Data Processing 26
2.5 Post Processing & Editing 26
2.5.1 Moored CTD Measurements 26
2.5.2 Current Meter (CM) Measurements 30
2.5.3 Dynamic Height(DH) Measurements 31
2.5.4 Bottom Pressure (BP) Measurements 33
2.5.5 Sea Surface Height (SSH) Altimetry 36
2.5.6 Surface and Sub-Surface Anomalies 40
2.5.7 Ekman Transport Datasets 41
2.5.8 Geostrophy and Mid-Ocean Transport Datasets 42
2.6 Methods 42
2.6.1 Interpolation in Gaps 42
2.6.2 Correlation and Cross Correlation 43
2.6.3 Gridding 45
2.6.4 Low Pass Filtering 47
2.6.5 Westward Filtering 48
2.6.6 Characterizing Propagating Features 50

2.6.7 Spectral Analysis 50
2.6.8 Summary 52

3 The Structure and Dynamics of Low-Frequency Variability 55
3.1 Chapter Overview 55
3.2 Low Frequency Variability 55
3.2.1 Theory and Mechanisms 56
3.2.2 Importance 58
3.2.3 Observing RW propagation 59
3.2.4 Discrepancy between observations vs. model propagation 64
3.2.5 Conclusions and Recommendations 66
3.3 Spectral Analysis 67
3.3.1 Altimeter Sea Surface Height (SSH) Datasets 67
3.3.2 Mooring Sub-surface Datasets 68
3.4 Spatial-Temporal Evolution of Features in Altimeter Sea Surface Height (SSH) Datasets 70
3.5 Spatial-Temporal Evolution of Features in Mooring Sub-surface Datasets 78
3.5.1 Currents and Temperatures 78
3.5.2 Bottom Pressures 86
3.6 Summary 89

4 The Use of Vertical Projection of Data and Statistical Modes in Improving Assessments of Variability 91
4.1 Chapter Overview 91
4.2 Introduction 92
4.3 Vertical Normal Mode (VNM) 92
4.3.1 Theory and Derivations 93
4.3.2 VNM and Rossby Waves (RWs) 98
4.4 Empirical Orthogonal Functions (EOF) Modes 104
4.4.1 Theory and Derivations 104
4.5 Results and Discussion 106
4.5.1 Meridional Velocity Modes 106
4.5.2 Temperature Modes 112
4.5.3 Dynamic Height Modes with Bottom Pressure 112
4.6 Summary 115

5 Assimilating Altimetric and Mooring Data 121
5.1 Chapter Overview 121
5.2 Introduction 121
5.3 Results and Discussion 122
5.3.1 Comparing SSHA and DHA Observations 122
5.3.2 Decreasing variability at the western boundary 123
5.3.3 Crossbasin local baroclinic variability 126
5.3.4 Variations with Transport Fluctuations 130
5.4 Summary 134

6 Conclusions and Future Work 135

6.1 Overall Summary and Conclusions 135
6.2 Limitations and Future Work 139

References **140**

List of Figures

Figure		Page
1.1	Schematic of the 2004 mooring array deployed by RAPID-MOC and MOCHA	2
1.2	Schematic overview of AMOC	3
1.3	Components of the NADW within the AMOC	4
1.4	Global estimates of heat transport	5
1.5	Model outputs of AMOC strengths	7
1.6	Global ocean circulation	8
1.7	Decrease in inter-annual AMOC mass transports and mean heatflux component across 25 °N from 1957 to 2004	9
1.8	Observational datasets used in thesis	10
2.1	Altimeter data merged in DUACS	15
2.2	Location of RAPID-MOC and MOCHA arrays during the 2004 to 2005 deployment	17
2.3	Cross section of RAPID-MOC and MOCHA arrays during the 2004 to 2005 deployment	18
2.4	Bathymetry of the Bahamas escarpment	19
2.5	Historical moorings off Bahamas	22
2.6	Time series of historical and present-day moorings off Bahamas	23
2.7	Resolution of historical and present-day moorings off Bahamas	24
2.8	Flowchart of early data processing steps	27
2.9	Challenge in correcting long term drift	35
2.10	Example of long term drift in bottom pressure time series	36
2.11	Spatial distribution of SSHA standard deviation	38
2.12	Spatial distribution of SSHA error	39
2.13	SSH standard deviation and error	40
2.14	Linear interpolation of gaps in dataset	43
2.15	Dataset spatial and temporal gridding	45
2.16	Example of new gridded datasets	47
2.17	Longitude/Time (Hovmöller) plot of SSH DUACS observations	49
2.18	SSH dataset at 26.5 °N, 20 to 80 °W Atlantic before and after interpolation and westward filtering	50
2.19	Range of spatial and temporal scales of motions	52
3.1	'First Mode Baroclinic' Rossby Wave	59
3.2	General importance of Rossby waves to the world oceans	60

3.3 Hovmöller (longitude/time) diagram of zonal section samples of Sea Surface Height (SSH) . . . 62
3.4 SSH PSD . . . 68
3.5 Meridional velocity PSD . . . 69
3.6 Past and present Hovmöller plots of SSHA . . . 71
3.7 Historical SSHA time series . . . 73
3.8 Time lag results from cross-correlation of SSHA from 1992 to 2006 . . . 75
3.9 Time shifted SSHA time series . . . 76
3.10 Standard deviation in SSHA variability at 26.5 °N . . . 78
3.11 Vertical plot of meridional velocity time series . . . 80
3.12 Vertical plot of temperature time series . . . 81
3.13 Mean meridional and temperature flow . . . 83
3.14 Vertical plot of meridional velocity anomalies . . . 84
3.15 Vertical plot of temperature anomalies . . . 85
3.16 Vertical plot of historical ACCP1 anomalies . . . 87
3.17 Bottom pressure time series . . . 88

4.1 Vertical normal modes . . . 105
4.2 Example of the original data matrix format . . . 106
4.3 Comparison of vertical structure of modes . . . 107
4.4 Meridional velocities EOF modal structure . . . 108
4.5 Meridional velocities anomalies and ECs . . . 111
4.6 Temperature EOF modal structure . . . 117
4.7 Temperature anomalies and ECs . . . 118
4.8 Dynamic height with bottom pressure EOF modal structure WB2 . . . 119
4.9 Dynamic height with bottom pressure EOF modal structure WB3 . . . 119
4.10 Dynamic height with bottom pressure EOF modal structure WB5 . . . 120
4.11 Dynamic height with bottom pressure EOF modal structure EB1 . . . 120

5.1 Temporal variability of SSH versus DHA at WB2 . . . 123
5.2 Temporal variability of SSH versus DHA at WB3 . . . 123
5.3 Temporal variability of SSH versus DHA at WB5 . . . 124
5.4 Standard deviation in SSHA variability at 26.5 °N . . . 125
5.5 Standard Deviation in Sea Surface Height and Dynamic Height Variability at 26.5 °N . . . 126
5.6 Baroclinic transport variability near the western and eastern boundaries 127
5.7 Local compensation of baroclinic variations at the western boundary . . 129
5.8 November 2004 Event in Temperature Datasets at Mooring Site WB2 . 130
5.9 Vertical structure of the mid-ocean transport per unit depth profile during November 2004 at WB2 . . . 131
5.10 Correlation of the residual bottom pressure variations after subtracting the variations due to baroclinic transport variability to the Gulf Stream Transport . . . 132

List of Tables

Table Page

2.1 Position of the western boundary moorings studied and instruments available . . . 19
2.2 Specifications of Seabird SBE37 Microcats . . . 28
2.3 Specifications of Aanderaa RCM11 . . . 30
2.4 Specifications of Sontek Argonaut MD . . . 31
2.5 Specifications of InterOcean Systems S4AD . . . 31
2.6 Specifications of Teledyne RDI 75kHz Longranger ADCP . . . 31
2.7 Available Bottom Pressure Recorders . . . 34
2.8 Specifications of Seabird SBE26 Wave and Tide Recorder . . . 34
2.9 Specifications of Seabird SBE53 Bottom Pressure Recorder . . . 35

3.1 Comparison of Barotropic versus Baroclinic Modes . . . 58
3.2 Spectral results from meridional velocity and SSH . . . 69
3.3 Cross correlation results of SSHA . . . 74
3.4 Range & mean of meridional velocity & temperatures of WB2, WB3 and WB5 . . . 79
3.5 Variability in Bottom Pressure Datasets . . . 88

4.1 First three EOF modes and the % variances explained at individual moorings WB2 and WB3 . . . 109
4.2 First three EOF modes and the % variances explained at individual moorings WB2, WB3, WB5 and EB1 . . . 114
4.3 Correlation between surface dynamic height (DH) and bottom pressure (BP) observations at Western boundary mooring sites. . . . 115

5.1 Comparison of Sea Surface Height and Dynamic Height Standard Deviation . . . 124
5.2 Standard Deviation of Baroclinic Transport (Sv) . . . 128

Acronyms

AC Antilles Current
AMOC (North) Atlantic Meridional Overturning Circulation
ACCP Atlantic Climate Change Programme
ADCP Acoustic Doppler Current Profiler
AOML Atlantic Oceanic & Meteorological Laboratories
AVISO Archiving, Validation and Interpretation of Satellite Oceanographic Data, France
BODC British Oceanographic Data Centre
BP Bottom Pressure
BPA Bottom Pressure Anomalies
CSIRO Commonwealth Scientific & Industrial Research Organisation
CTD Conductivity, Temperature, Density
DH Dynamic Height
DHA Dynamic Height Anomalies
DUACS Developing Use of Altimetry for Climate Studies (since changed to Data Unification and Altimeter Combination System)
DWBC Deep Western Boundary Current
EC Expansion Coefficients
EOF Empirical Orthogonal Functions
ERS European Remote Sensing
FCTP Florida Current Transport Programme
FFT Fast Fourier Transform
AMOC Meridional Overturning Circulation
(M)ADT (Map of) Absolute Dynamic Topography
MOCHA Meridional Overturning Circulation and Heat-flux Array
(M)SLA (Map of) Sea Level Anomaly
NADW North Atlantic Deep Water
NASA National Aeronautics and Space Administration
NCAR National Center for Atmospheric Research
NCEP National Center for Environmental Prediction
NERC National Environmental Research Council
NSF National Science Foundation
NOAA National Oceanic & Atmospheric Administration
NOCS National Oceanography Centre, Southampton U.K.
PCA Principal Component Analysis
PC Principal Component
PSD Power Spectrum Density
RAPID-MOC Rapid Monitoring the Atlantic Meridional Overturning at 26.5 °N
RT Radon Transform
RW Rossby Waves
SSALTO Ssalto multimission ground segment
SSH Sea Surface Height
SSHA Sea Surface Height Anomalies
STACS Subtropical Atlantic Climate Studies
SVD Singular Value Decomposition
THC Thermohaline Circulation
T/P Topex/Posidon
UNESCO United Nations Educational Scientific and Cultural Organization
WATTS Western Atlantic Thermohaline Transport Study
WB Western Boundary

Declaration

This dissertation describes my own original work except where acknowledgment is made in the text. To the best of my knowledge it is not substantially the same as any work that has been, or is being submitted to any other university for any degree, diploma or other qualification.

Published work in (Bryden et al., 2009) which combined the analysis of sea surface height, bottom pressure and dynamic height was a joint effort by all authors. A. Mujahid provided sea surface height, H.L. Bryden provided bottom pressure, S. Cunningham and T. Kanzow provided dynamic height. Key results from this thesis work are: (i) sea surface height and dynamic height correlation at the same time and amplitude scales; (ii) variability in sea surface height and dynamic height decrease as the western boundary is approached.

Acknowledgements

My greatest heartfelt thanks, especially to my supervisor Harry Bryden who has been the main driving force and my greatest supporter through thick and thin. To Adrian Martin, as well as my advisors Ian Robinson and the late Peter Killworth - for your insights and patient guidance, I am very grateful.

Most of the effort of writing this thesis has been done at the National Oceanography Centre, Southampton (NOCS). I kindly thank the institution and my sponsors, the Malaysian Public Services Department *Jabatan Perkhidmatan Awam* (JPA), as well as my employers *Universiti Malaysia Sarawak* (UNIMAS) for their gracious financial support.

The material for this thesis has also been drawn from many sources. I am indebted to many colleagues for their co-operation and aid, assisting a non-physical oceanographer to understand this fascinating science. The individuals from NOCS and RSMAS to name a few - Joel Hirschi, Torsten Kanzow, Guillaume Charria, Stuart Cunningham, Paolo Cipollini, Darren Rayner, Bill Johns, Lisa Beal, Jon Molina and Zoltan Szuts are gratefully acknowledged. Figures 4.8 to 4.11 and selected graphs in Chapter 5 that were published in a paper in Ocean Science were professionally prepared by Mary Woodgate-Jones, and I gratefully acknowledge her help.

For being my light in the storms, and my rock in the rough waters - many thanks to my family in Malaysia, my husband Moritz and a very good friend Caroline for their encouragement, love and support. Without forgetting, to all my friends and acquaintances met during my 5 years in Southampton.

Thank God for curry-nights...

Chapter 1

Introduction

1.1 Background

The RAPID-MOC - '*Monitoring the Atlantic Meridional Overturning at 26.5 °N*' is a project that is part of the Rapid Climate Change thematic programme, under which an extensive amount of observational data in this thesis is obtained. Science is always better served with substantial funds committed and so, this U.K. National Environmental Research Council project was in joint support with the U.S.A. funded MOCHA ('*Meridional Overturning Circulation and Heat-flux Array*') enabling funding for a unique array of 22 trans-Atlantic moorings including 9 full depth moorings (Fig.1.1) deployed and serviced annually since Spring 2004 and continuously improved from year to year. At present, it is extended until 2014 to obtain for the first time, a continous high resolution decadel time series under the RAPID-WATCH Programme, please see the official website at *http : //www.noc.soton.ac.uk/rapid/rw*.

The mooring arrays are favoured (Fig.1.1) over the repeated hydrographic sampling strategy as that option can prove to be expensive, and would only detect decadal changes (Baehr et al., 2004) as well as being temporally limited. Continuous monitoring is driven by the need to further our understanding of the health status of the North Atlantic Meridional Overturning Circulation (AMOC) using continuous 'real' measurements. This includes monitoring of the possible small-scale variability (timescales of less than a year) to long term changes in the future. The project aim was to establish

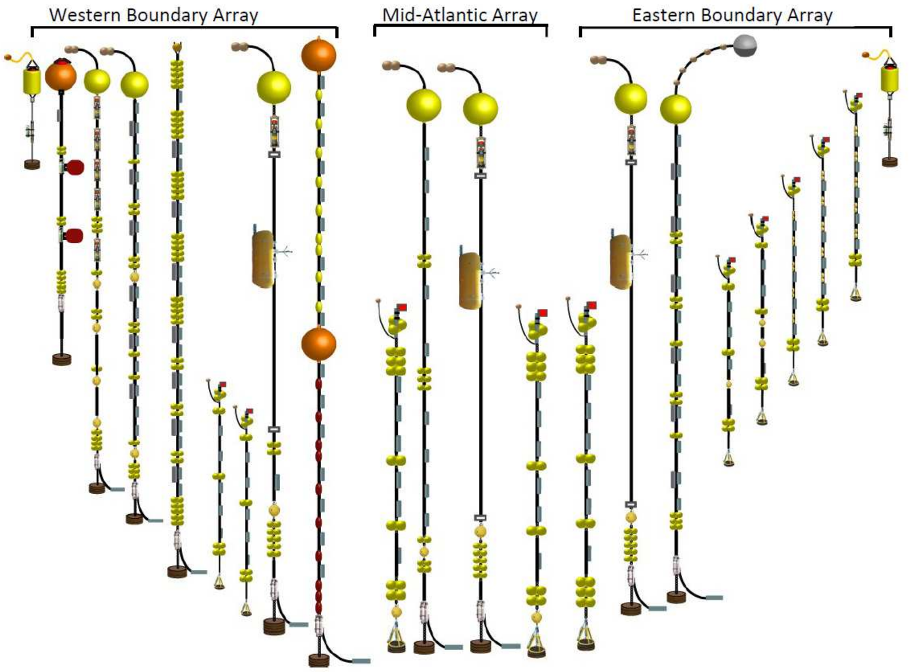

FIGURE 1.1: Schematic of the 2004 mooring array deployed by RAPID-MOC and MOCHA which consists of the western boundary array, the mid-Atlantic array and the eastern boundary array (Courtesy of RAPID-MOC).

a robust operational prototype array to enable the direct and continuous monitoring of the strength and structure of the AMOC in the western subtropical North Atlantic at 26.5 °N. This is unlike previous observations systems, which were too infrequent, with high uncertainty and thus unable to detect the important changes in the AMOC (Deutsch et al., 2002). The reader is directed to Chapter 2 for further explanation on the datasets used in this thesis.

Definitions of the North Atlantic Meridional Overturning Circulation (AMOC) vary slightly between authors but generally it is defined as the total zonal integral (across an ocean basin) of the northward/ southward flow (mass or volume transport) as a function of depth and latitude (Talley, 2003; Rahmstorf, 2006). The North Atlantic Meridional Overturning Circulation - known hence forth in this thesis as the AMOC, is conceptually entangled with the Thermohaline Circulation (THC) - often labelled as a North Atlantic limb of the global oceanic 'conveyor belt'. Although the AMOC can be broken into two components i.e. (i) the wind forced Ekman component; and (ii) the density-driven THC, they are not two separate circulations though they may have distinctively different forcing mechanism.

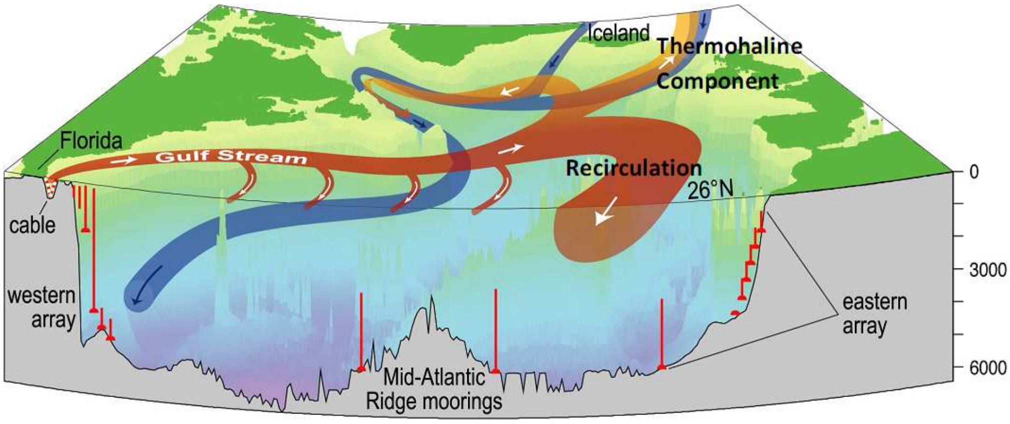

FIGURE 1.2: Schematic overview of the North Atlantic Meridional Overturning Circulation (AMOC) at 26 °N with the components measured using the Rapid-MOC and MOCHA trans-Atlantic array (Courtesy of Louise Bell and Neil White, CSIRO).

The Thermohaline Circulation (THC) is the stronger element of the AMOC (Hirschi et al., 2003; Baehr et al., 2004) forced by difference in surface density driven by temperature (heat) and salinity changes (Gill, 1982). As seen in Fig.1.2, the THC transports the warm surface saline waters (red) northwards from the tropics to the high latitude northern Atlantic and shores of north-west Europe. The warm water then cools (cooling induced deep convection) and sinks to the ocean floor as a cold, dense water mass (blue) known as the North Atlantic Deep Water (NADW) which returns back southward at depths into the tropics and creates an overturning cell. Sinking happens in two areas of high latitude deep water formation i.e. (i) the Labrador Sea (between Greenland and Canada creating Upper North Atlantic Deep Water, UNADW) and, (ii) the GIN Sea (between Greenland, Iceland and Norway creating Lower North Atlantic Deep Water, LNADW). The two distinct layers of the NADW are depicted in 1.3(a) and briefly differentiated in Fig.1.3(b). This sinking of cold, dense water is thought to be the most important part of the THC in the North Atlantic (Broecker, 1991), and is the primary driving force of the THC (Colling, 2002). To discover the strength of the THC, the observable AMOC is measured as a proxy. Firstly, this can be obtained from the vertical integration of the warm upper waters, to determine the total northward flow which defines the strength of the AMOC. This is possible because the North Atlantic basin is nearly closed to the North, and so the net northward flow of warm upper waters is equal to the net southward flow of the cold deeper waters each about 15

Sv. Secondly, the strength of the AMOC can also be estimated by integrating vertically upward from bottom, the southward flow of cold waters. Results showing a reduced NADW flow will be indication of reduced 'sinking' or overturning (as well as changes in density structures), and thus an impact of reduced northward flow in the AMOC from low to higher latitudes. From observation of both UNADW and LNADW separately, we can determine which areas have reduced deep water formation.

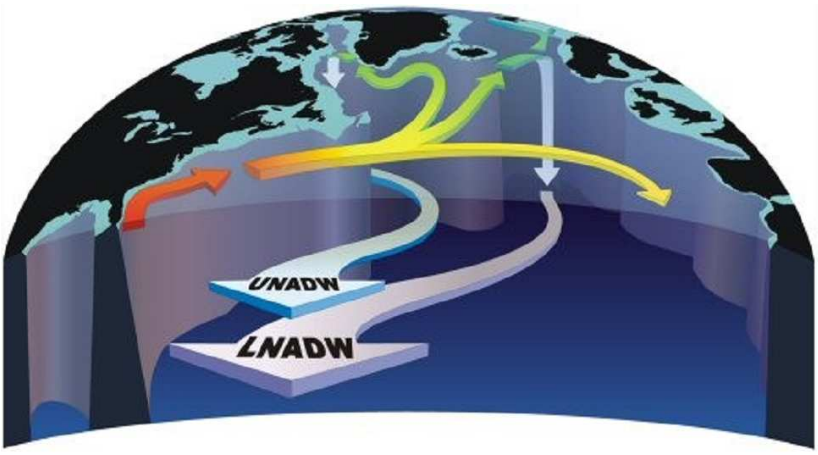

(a)

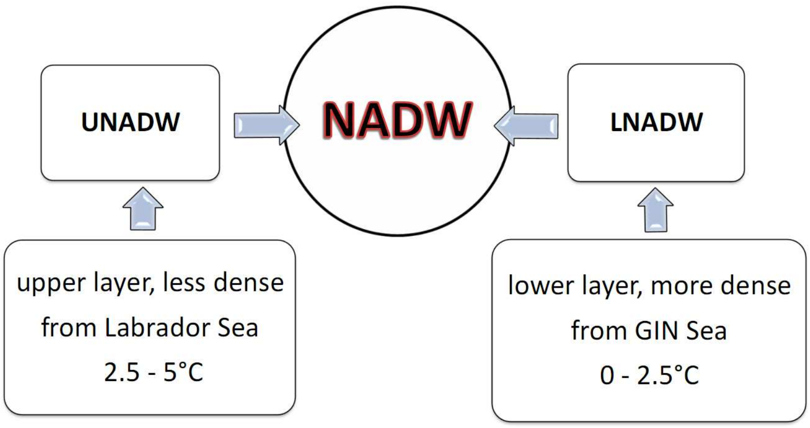

(b)

FIGURE 1.3: (a) The vertical structure of the AMOC depicting the UNADW and LNADW (Courtesy of RAPID/ NERC); (b) Brief comparison of characteristics of both NADW components of upper North Atlantic Deep Water, UNADW (created in the Labrador Sea) and lower North Atlantic Deep Water, LNADW (created in the GIN Sea - between Greenland, Iceland and Norway).

The AMOC is largely studied for its importance for the local and global climate. It accounts for the primary mechanism for heat transport and almost all the oceanic northward heat transport in the Atlantic (Hall and Bryden, 1982; Bryden, 1993), see Fig.1.4). Direct oceanographic measurements in the 1950s and 1970s by Hall and Bryden (1982) led to the estimate of the heat transport at 25 °N to be 1.22 PW (1 PW: 10^{15}W). Several other inverse calculations agree that the AMOC carries most of the maximum 1 PW, heat transport that represents about 20 - 30 % of the global atmospheric and ocean heat flux northwards across 25 °N (Roemmich and Wunsch, 1985; Trenberth and Solomon, 1994; Lavin et al., 1998; Ganachaud and Wunsch, 2000; Bryden and Imawaki, 2001; Dong and Sutton, 2001; Baehr et al., 2004; Bentson et al., 2004). This is largely responsible for the milder climate in North Western Europe compared with similar latitudes in the Pacific (Rahmstorf, 2003), and where there is no AMOC (Manabe and Stouffer, 1988; Broecker, 1991; Vellinga and Wood, 2002; Baehr et al., 2004). On a larger scale, this is important because the earth's stable climate largely depends on such mechanisms of heat transport by the coupled ocean-atmosphere system. Models such as by Trenberth and Caron (2001) and Czaja and Marshall (2005) show that at lower latitudes, both the atmosphere and ocean (wind and thermohaline-driven) contribute equally to the total poleward heat transport, however at latitudes higher than 30 °, the atmospheric contribution amounts to roughly 90%.

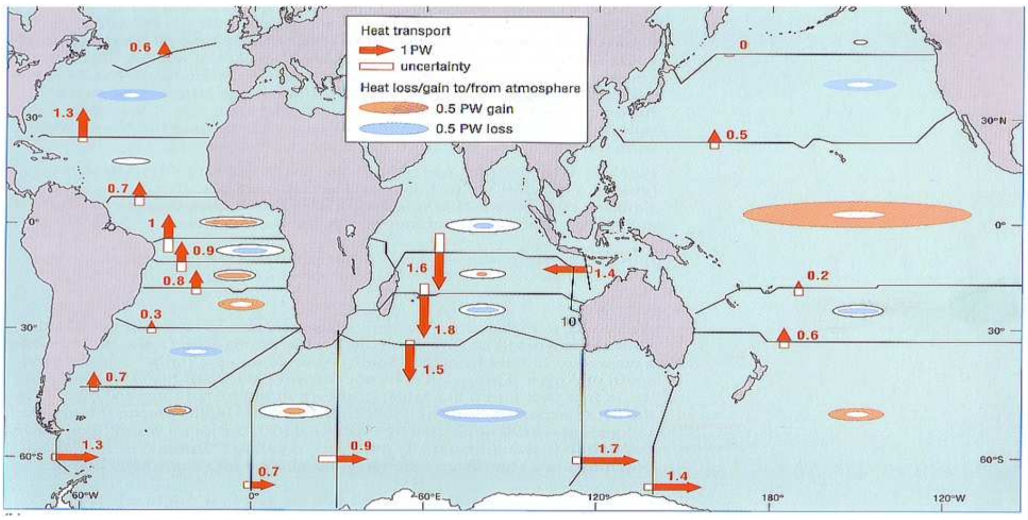

FIGURE 1.4: Global estimates of heat transport, as well as areas losing/gaining heat to/from atmosphere. About 1.3 PW of heat is transported northwards at 26 °N (Colling, 2002)

Model comparison studies e.g. Rahmstorf and Ganopolski (1999); Wood et al. (1999); Marotzke (2000); Stocker (2000); IPCC (2001); Bentson et al. (2004); Johnson and Marshall (2004); Gregory et al. (2005), suggest that the THC will slow down or even shut-off - as soon as 2100 - under the global warming effect of increasing anthropogenic CO_2 on the climate (see Fig.1.5 for examples of varying results). According to Bentson et al. (2004), the North Atlantic region has experienced surface temperature variations of 5 to 10 °C on multi-annual to decadal timescales which are linked to the AMOC. Some authors go further by suggesting the slowdown of the North Atlantic THC (i.e. the AMOC) might already be occurring (Häkkinen, 2001; Bryden et al., 2005b). According to Rahmstorf (2006), although general ideas of the mean meridional north-south AMOC flow have been produced, not much is known about its fluctuations and further climatic contributions. It has been increasingly important to understand and improve assessment of changes in the AMOC and associated risks of rapid climate change. It is an encouraging fact that the AMOC can be easily diagnosed from a model and in principle can be measured in the ocean. So what is the present status of the AMOC? Unfortunately, the present AMOC 'health' status is not such a simple story.

Long term trends and changes remain a great challenge to observe and interpret using recent datasets. Although there are various maps of global ocean circulation e.g. Fig.1.6 by Ganachaud and Wunsch (2000), speculations on the 15 to 25 % uncertainty also still exist. There is little knowledge about possible long-term changes in the AMOC and their causes mainly due to a lack of observations (Dong and Sutton, 2001). This makes the projections from model outputs unreliable as they are difficult to compare with the present state of observations. From sparse transatlantic shipboard hydrography along 25 °N (between 1957 to 1992), Lavin et al. (1998) concluded that the zonally averaged meridional transport and large scale velocity field were similar, and the structure of the baroclinic circulation did not change a great deal (Lavin et al., 2003). Further sparse transatlantic shipboard hydrography as reviewed by Bryden et al. (2005b) in the past 50 years (between 1957 and 2004) had conflicting results reflecting: (i) the weakening of AMOC strength by 5 to 6 Sverdrup (1 Sv = 10^6 m^3/s) or around 30 % from half century ago; (ii) a change of meridional heat transport across 25 °N by 0.3PW, as illustrated in Fig.1.7. These observational findings are based on 'snapshots'

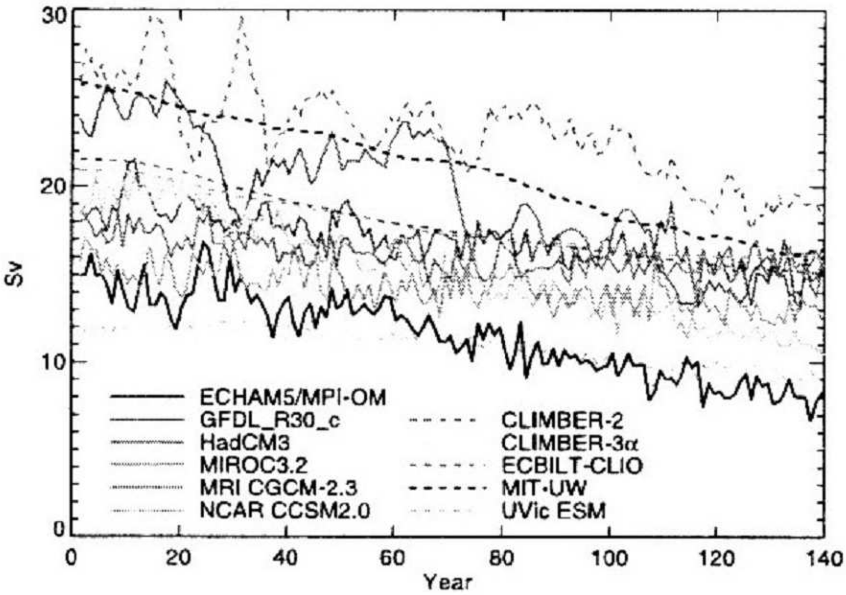

(a)

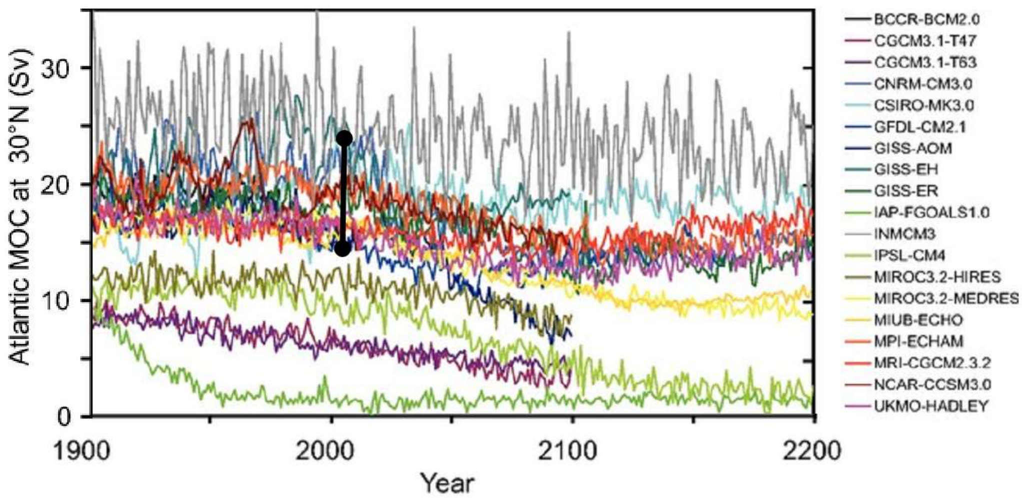

(b)

FIGURE 1.5: (a) Eleven different model outputs of AMOC strength over 140 years taking into account the projected anthropogenic CO_2 levels (4x current levels) by Gregory et al. (2005); (b) Nineteen model outputs of the AMOC strength at 30 °N from 1850 to 2100 taking into account the projected anthropogenic CO_2 levels adapted from IPCC (2007). Black bold line represents observed AMOC variability from initial 3.5 years of RAPID observations with a mean AMOC of 18.5 Sv with a standard deviation of ± 4.9 Sv.

of the ocean and may not be representative and cannot be interpreted as long term trends. Adding to that, there has been no continuous AMOC transport dataset of real measurements, and so neither the short term variability nor the inter-annual variability are known.

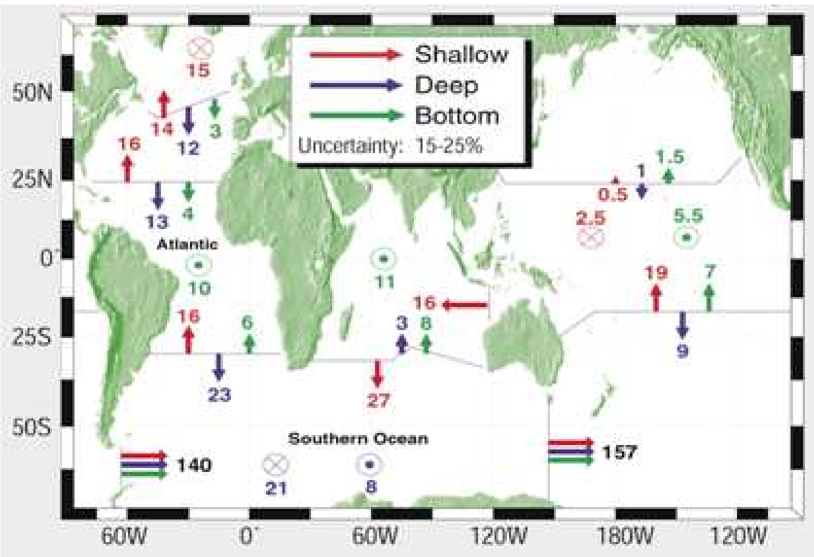

FIGURE 1.6: Global ocean circulation map depicting strength of shallow, deep and bottom flow with uncertainty of 15 - 25 %. Estimates at 26 °N are: 16 Sv of northward shallow flow; 13 Sv of southward deep flow; and 4 Sv of bottom flow (Ganachaud and Wunsch, 2000).

Possible disturbances such as ocean eddy and natural fluctuations in the strength of the circulation system must be considered (Schiermeier, 2005). Recent numerical model simulations by Hirschi et al. (2006) and A. Brearley (*Personal Communication*) suggest that on short timescales there is a link between baroclinic transport components and westward moving transport anomalies (possibly long baroclinic Rossby waves) which could contribute several Sverdrups to the AMOC variability. Häkkinen (2001) showed that sea surface height variability outside the western boundary current region is determined by local and remote wind stress forcing.

All possible contributions in observations must be accounted for especially including the possibility of propagating features. By further examining the vertical structure, and dynamics of the propagating features especially their interaction at the boundaries, we hope to create some basic knowledge on the vertical modal structure which can improve estimates and interpretations of the transport fluctuations in the overturning circulation.

Focus of early research by the RAPID-MOC was on observing the strength and variability of the AMOC at 26.5 °N by using these observational findings. As mentioned earlier, Bryden et al. (2005b) suggested a 30 % weakening of the annual average

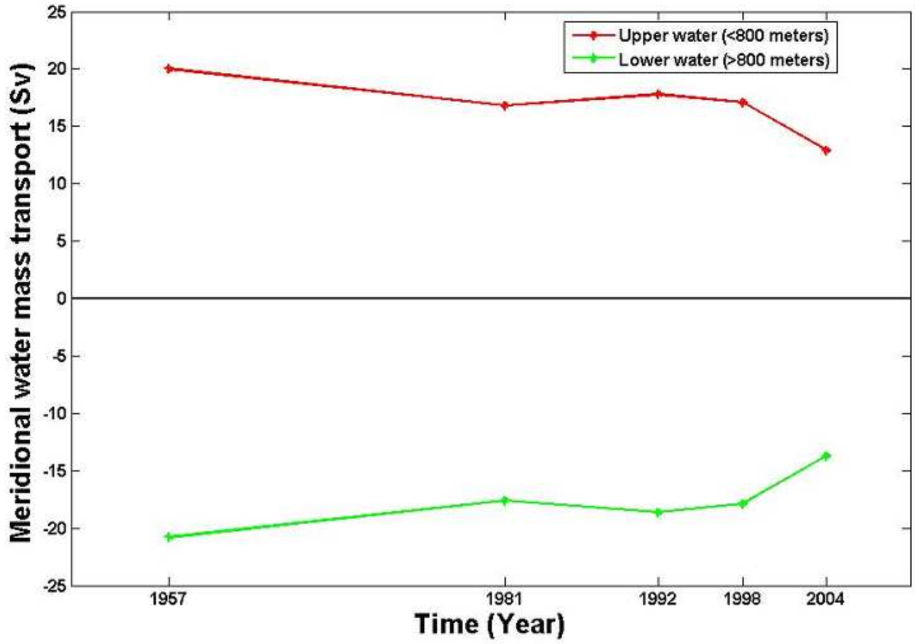

(a)

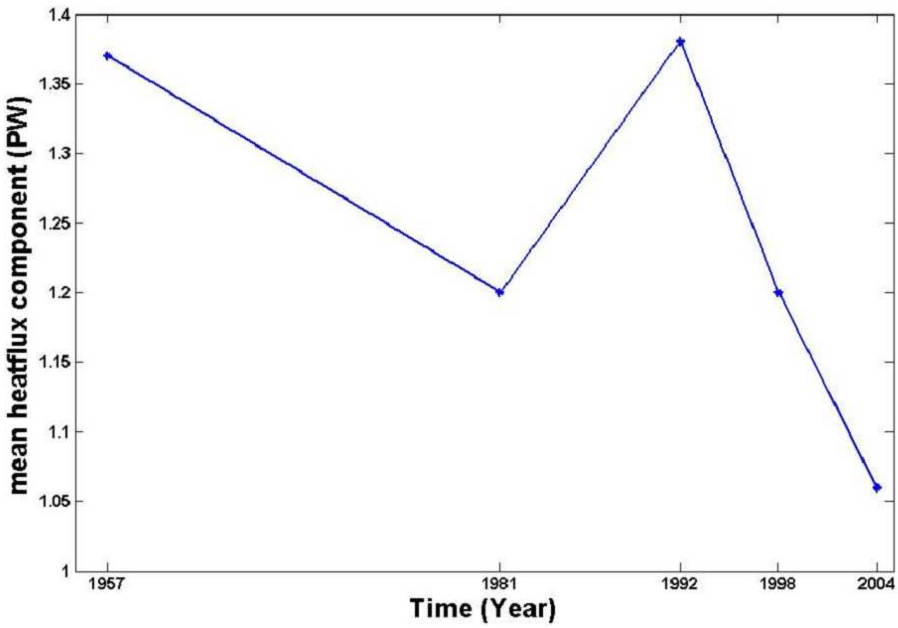

(b)

FIGURE 1.7: (a) About 50 % decease in inter-annual meridional water mass transport (Sv) in the lower (below 800 m in green) and upper (above 800 m in red) water masses from 1957 to 2004; (b) Weakening by 0.3 PW in mean heat-flux component across 25 °N. Both figures constructed based on tables in Bryden et al. (2005b)

overturning of the AMOC from 1957 to 2004. Although the net northward transport in the Gulf Stream (GS) did not vary much over the time period, the net southward

NADW transported at depths (between 3000 m and 5000 m) had decreased by 50 % and the southward recirculation of thermocline waters as the mid-ocean transports had increased by 50 %. Cunningham et al. (2007) have used the first year mooring observations to study the temporal variability in the AMOC, determining large sub-annual variability at all depths thus rendering short term monitoring difficult. Kanzow et al. (2007) have demonstrated that the array is effectively monitoring the basin-scale circulation by showing that the array measurements satisfy mass conservation.

1.2 Outline of thesis

The thesis aims to better understand the possible effects of slowly-varying propagating features to the dynamics and variability at western boundary 26.5 °N and ultimately the AMOC. For the first time, we have substantial unprecedented measurements from unique simultaneous combination of the spatial-temporal observations of various sub-surface and surface properties (Fig.1.8).

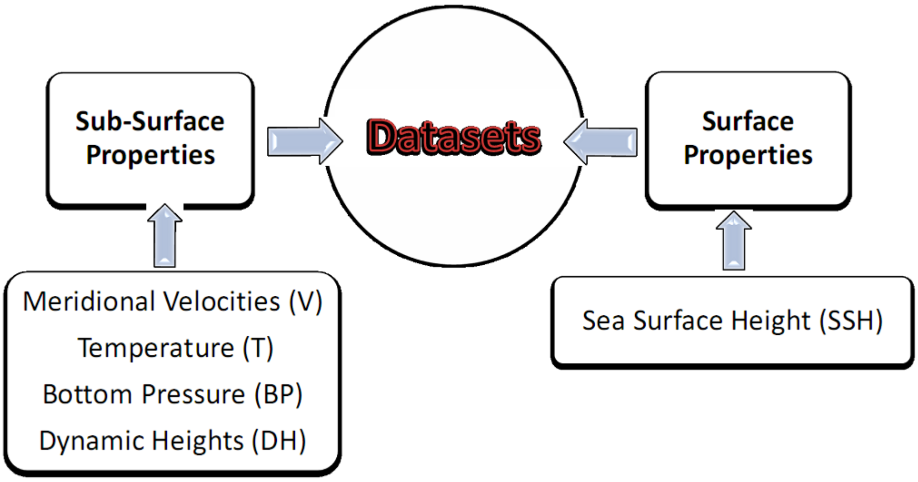

Figure 1.8: Combination of observational datasets used in this thesis which consist of various surface and sub-surface properties.

Results will show fresh insights into exploring the contribution of propagating features to the vertical structure of temporal-spatial evolution in the western boundary at 26.5 °N and its relative contribution to the observed intra- (short term) and inter- annual (long term) temporal variability in AMOC. Work here is therefore critical for future interpretation of AMOC fluctuations.

Results are sub-divided so that specific aspects can be studied, documented and considered separately. A number of challenging aims are posed:

- To observe the temporal-spatial variability of the propagating features near the western boundary at 26.5 °N derived from mooring datasets of sub-surface properties and from satellite altimetry surface properties.
- To quantify the relative contribution of propagating features to the western boundary at 26.5 °N from observed temporal-spatial evolution on various timescales from i.e. shorter (monthly and seasonal) to longer (intra and inter-annual) timescales.
- To determine the relationship between surface and sub-surface properties for better future interpretations of the observations of AMOC fluctuations.

We begin the thesis, (Chapter II: Dataset and Methods) by documenting the datasets used and methods employed. This includes: (i) an introduction to the surface datasets (sea surface height datasets from altimetry) and sub-surface datasets (present and historical mooring array); (ii) basic data recovery, editing and data processing; and (iii) methods used in further analyses.

Chapter III: Structure and Dynamics of Low Frequency Variability characterise the temporal-spatial variability of propagating features from altimetry and sub-surface properties from moorings in the western boundary Atlantic at 26.5 °N. We also determine the possibility of tracking propagating features observed in temporal-spatial variability.

Chapter IV: The Use of Vertical Projection of Data and Statistical Modes in Improving Assessments of Variability then describes the vertical modal structure derived from the observations and the boundary conditions imposed. From these, we determine the extent to which statistical vertical modes compare to theoretical vertical modes of variability. We also determine the quantitative amount which propagating features contribute to the observed temporal-spatial AMOC variability.

The penultimate section, Chapter V: Assimilating Altimetry and Mooring Data contains investigations into studying the temporal-spatial variability of various sub-surface signals (e.g. dynamic height, and bottom pressure) versus the surface signals (sea surface height from altimeter datasets) in the western boundary 26.5 °N. Ultimately, we evaluate the inter-relationship between the surface and sub-surface properties on various time scales. Results here define the prospect of using limited surface datasets to reflect and infer the sub-surface signals.

Finally, Chapter VI: Conclusions & Future Work will discuss the overall conclusions of the sections. We aim to determine the answers to questions posed earlier, suggest possible future analyses to complete the chapter and draw final conclusions to the thesis.

Chapter 2

Dataset and Methods

2.1 Introduction

This chapter provides information on the background of different datasets available, how different datasets could be and are used, as well as the various methodologies employed. These include: (i) an introduction to the surface datasets i.e. sea surface height from altimeter datasets, as well as sub-surface datasets from mooring datasets; (ii) basic data recovery, pre- and post- processing and data editing; and finally (iii) the methods employed in further analyses. A guide to information on the performance and errors to be expected in the records from the comparisons of various instruments were done but not included in this thesis.

Observations in this thesis involve the opportunistic use of time series observations from:

- The sea surface height (SSH) dataset from Developing Use of Altimetry for Climate Studies (DUACS), see Section 2.2.
- Daily QuikScat wind stress values to estimate Ekman Transport (T_{EK}) datasets, see Section 2.5.7.
- Mooring datasets from the first year deployment of the 'Monitoring the Atlantic Meridional Overturning at 26.5 °N (RAPID-MOC) and 'Meridional Overturning Circulation and Heat-flux Array' (MOCHA) mooring array at the western boundary 26.5 °N as well as some historical moorings, see Section 2.3.1.
- Datasets available from the Florida Current Transport Programme (FCTP) to derive Florida Straits transport (T_{FS}) datasets, see Section 2.3.2.

2.2 Surface Satellite Datasets

Altimeter datasets for Sea Surface Heights (SSH) are comprised of: (i) the historical altimeter datasets (1992 to 2004) from TOPEX/Poseidon (T/P) satellite altimeter; (ii) present up-to-date altimeter datasets (2004 to 2006) from DUACS (Developing Use of Altimetry for Climate Studies). Figure 2.1 depicts the merged DUACS altimeter data from the following satellites: (i) ERS (European Remote Sensing); (ii) T/P (TOPEX/Poseidon); (iii) Envisat; and (iv) Jason. The SSALTO/DUACS User Handbook for (M)SLA and (M)ADT Near-Real Time and Delayed Time Products has further details and can be found at the AVISO (Archiving, Validation and Interpretation of Satellite Oceanographic Data, France) official website (*http://www.aviso.oceanobs.com/fileadmin/documents/data/tools/hdbk_duacs.pdf*). Rigorous description of the data processing, mapping methods and standard corrections applied can be found in Le Traon and Ogor (1998) and Le Traon et al. (1998). The DUACS SSH datasets are on a Mercator spatial grid of 1/3 °longitude x 1/3 °latitude, with a temporal sampling of 7- days. Here we sub-sample the dataset near latitude 26.5 °N, longitudes 20° to 80 °W. The use of altimeter data offers the possibility to monitor movement and development of features over large spatial and temporal domains as well. Their inclusion into large scale oceanic studies and models provide a key element for both modelers and operational oceanographers and into future ocean forecasting systems. Please refer to Section 2.6.3 for the methods used in preparing the SSH gridded datasets (bi-linearly interpolated onto 26.5 °N).

Other surface datasets from satellites include the Ekman transport (T_{EK}) which is estimated using daily QuikScat wind stress values. Please refer to Section 2.5.7 for the methods used in preparing the Ekman Transport datasets.

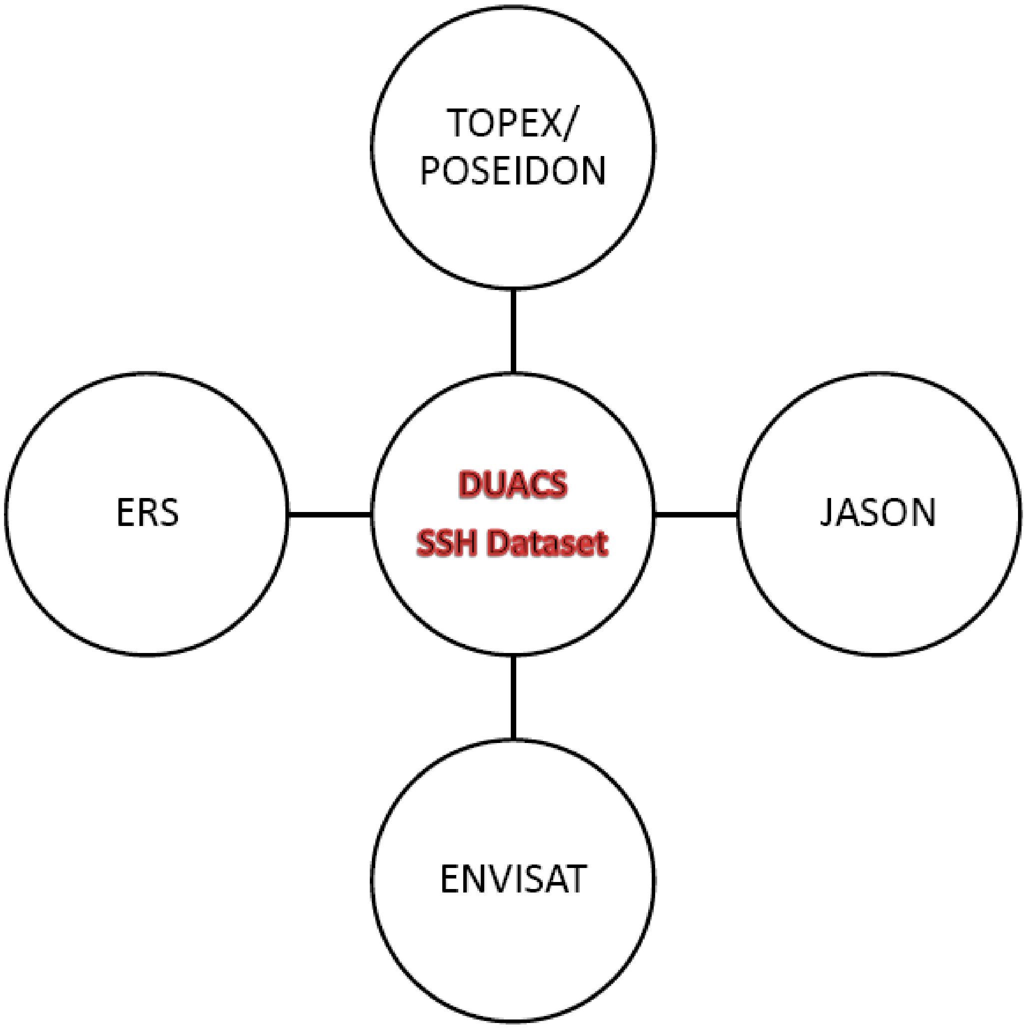

FIGURE 2.1: Altimeters merged in DUACS (Developing Use of Altimetry for Climate Studies) from ERS (European Remote Sensing), T/P (TOPEX/Poseidon), Envisat, and Jason satellites.

2.3 Sub-Surface Dataset

2.3.1 The RAPID-MOC, MOCHA and Historical Arrays

The full RAPID-MOC and MOCHA array of transatlantic pre-operational prototype mooorings (as seen in Fig.1.1) of 22 moorings have produced various key measurements in the first year operations from spring 2004 to 2005. These include measurements of velocity (from speed and direction), temperature, salinity (from conductivity, temperature and pressure), pressure and co-located bottom pressure. The hydrography cruises provide accompanying top-to-bottom CTD casts. Positions of the full mooring array are as in Fig.2.2. Further information on RAPID-MOC and MOCHA 2004 to

2005 deployments can be found in cruise reports by Cunningham (2005b,a). Please refer to Section 2.5.8 for the methods used in preparing the Mid-Ocean Transport datasets from the moorings.

The western boundary moorings used in this thesis are seen in Figure 2.3 and also summarized in Table 2.1 which briefly lists their positions and the primary instruments available. In this thesis, the analysed dataset from the first year mooring deployment used are: (i) Position B moorings - the full depth moorings WB2 and WB3 were placed there to capture the western boundary variability of the AMOC; (ii) Position E mooring - the full depth mooring WB5 was placed there to capture the meandering DWBC. From the fore-mentioned figure and table as well as Figure 2.4, note the position of WB2 at the foot of the continental slope close to an escarpment. Datasets from the WB2 mooring in the first year deployment have indicated a strong signature of shielding by the ridge protruding from the escarpment from below about 1600 m depths, further explained in Johns et al. (2008). This leads to possible recirculation with weak deep currents and so datasets from WB2 will be studied with extra caution.

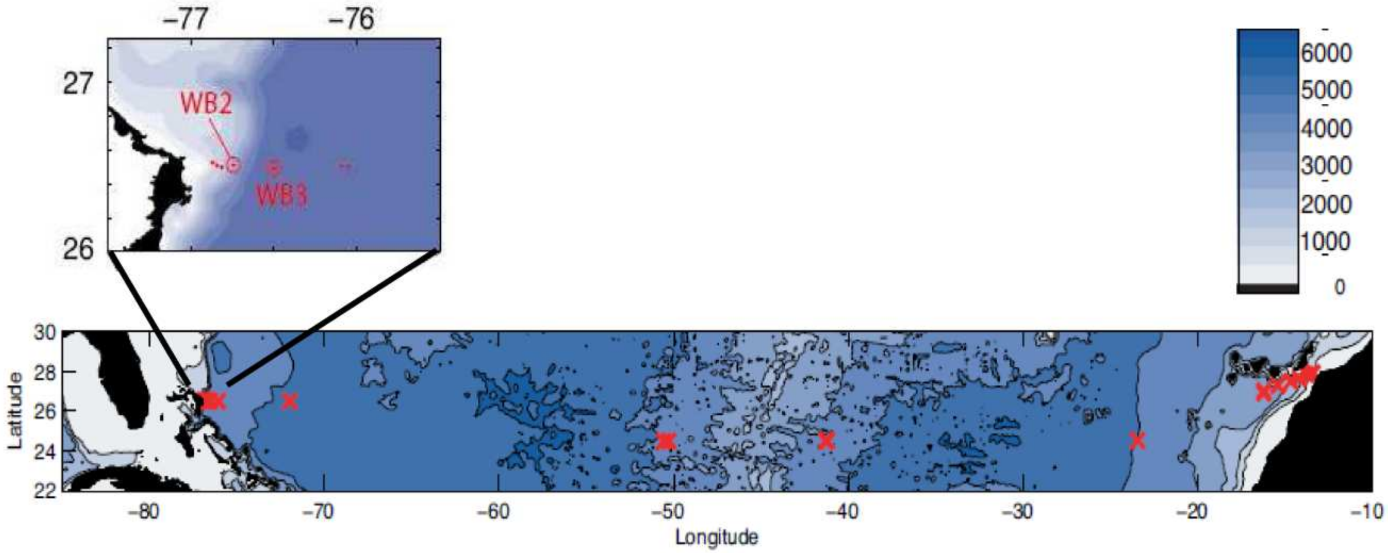

FIGURE 2.2: Location of RAPID-MOC and MOCHA arrays during the 2004 to 2005 deployment (Courtesy of RAPID-MOC and MOCHA): (a) Location of trans-Atlantic mooring array with individual moorings in relation to bathymetry at 26.5 °N, with an enlargement of the western boundary moorings

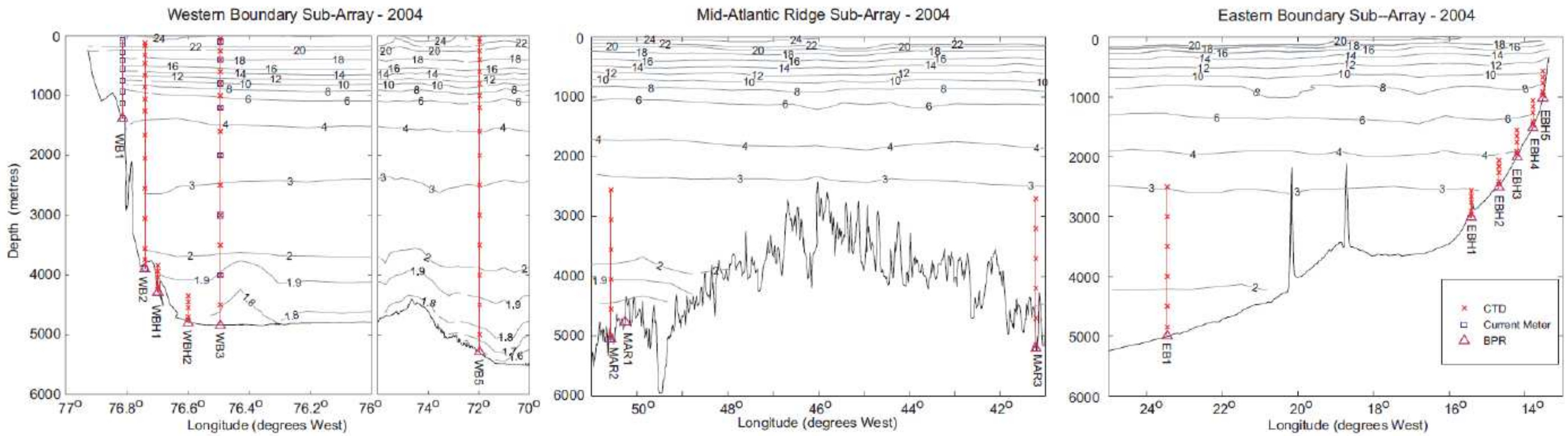

FIGURE 2.3: Cross section of RAPID-MOC and MOCHA arrays during the 2004 to 2005 deployment (Courtesy of RAPID-MOC and MOCHA): (b) Cross section showing vertical structure arrangement of CTD, current meter and bottom pressure recorder instruments along the mooring arrays. Of the 15 bottom pressure recorders and 12 dynamic height moorings, only the instruments successfully providing year long datasets are depicted here.

Table 2.1: Position of the western boundary moorings WB2, WB3 and WB5 studied and instruments available.

Mooring	Position	Instruments
WB2	60 km offshore at foot of continental slope, within rise of Bahamas escarpment at 26.52 °N, 76.74 °W	Current meters, temperature, salinity and pressure
WB3 a.k.a. BJB	27 km offshore of WB2, within 100 km of western boundary DWBC domain at 26.50 °N, 76.5 °W	Current meters, temperature, salinity and pressure
WB5 a.k.a. BJE	504 km offshore, 320 km offshore from WB3 at 26.49 °N, 71.97 °W	Temperature, salinity and pressure

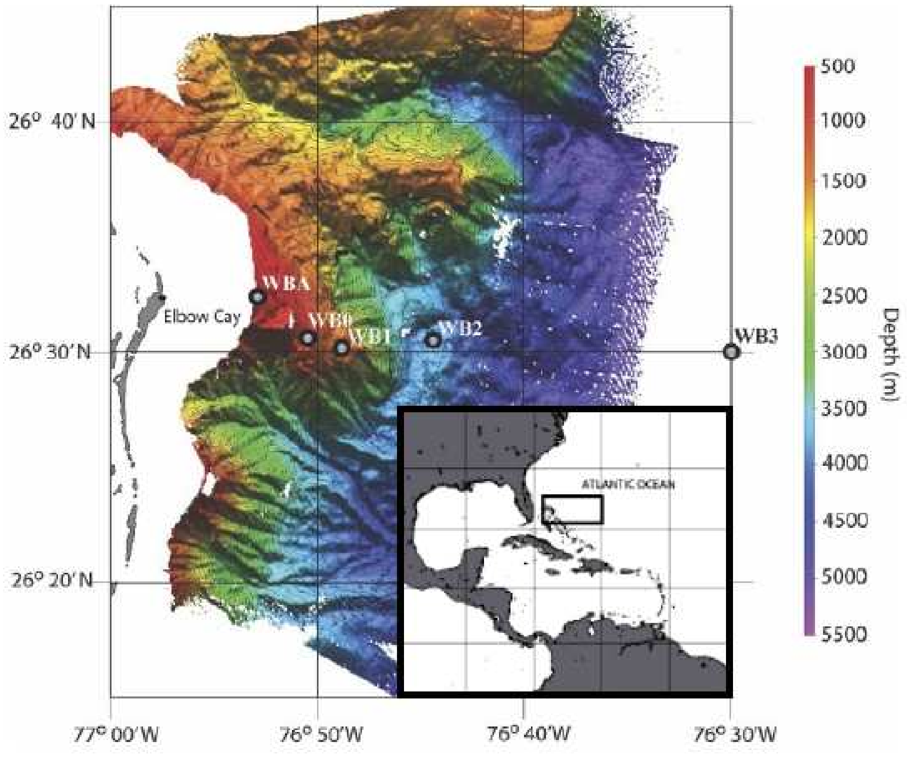

Figure 2.4: Insert shows the Western Boundary study area in relation to the American coast and the Bahamas Islands at 26.5 °NW Atlantic. The close up shows the bathymetry of the Bahamas escarpment off Abaco Island derived from SeaBeam acoustic bottom survey with positions of the RAPID-MOC and MOCHA Western Boundary area, adapted from Johns et al. (2008).

Supplementary baseline datasets to the western boundary RAPID-MOC and MOCHA mooring datasets at 26.5 °N include historical set of mooring arrays, ship observations and satellite datasets. A continuous series of 7 deployments forming an extensive 11 year historical moored current meter observations from off Bahamas exist (see Fig.2.5 and 2.6). These were funded by NOAA (National Oceanic and Atmospheric Administration) and NSF (National Science Foundation), from March 1986 to June 1997.

A summary of the historical western boundary moorings at 26.5 °N can be found in technical reports by Zantopp et al. (1989a,b, 1990, 1993, 1996, 1998a,b) and the scientific results can be found in Lee et al. (1990, 1996) and Fillenbaum et al. (1997). Namely the historical deployments are:

1. Subtropical Atlantic Climate Studies (STACS-7, -8, -10)
2. Western Atlantic Thermohaline Transport Study (WATTS)
3. Atlantic Climate Change Programme (ACCP-1, -2, -3)

The initial criteria that should be used for choosing complementary historical mooring datasets are:

1. Proximity of the historical moorings with present mooring sites
2. Availability of altimetry datasets for SSHA during mooring sampling times
3. Quality and resolution of time series datasets

Extending the time series of moorings along 26.5 °N using historical moorings would be beneficial to expand the length of the time series in an effort to increase statistical reliability in this study of low-frequency, slowly propagating features. All the processing and analysis done on any of the historical datasets used will be similar to those applied during the first year RAPID-MOC and MOCHA mooring deployment.

The placements of the instruments on each mooring are irregular on a vertical depth scale similar to the hydrographic quasi-logarithmic sampling, as seen here Fig.2.7. Generally, there is good full depth dataset at position B (60km offshore) and E (320 to 500 km offshore). Model studies by Hirschi et al. (2003) and Baehr et al. (2004) of the RAPID-MOC and MOCHA mooring design show that such sampling has the ability to capture the vertical structure and time history of the maximum AMOC. Thus the spatial variability should reflect the 'real' ocean structure (most rapid vertical changes at surface) and has sufficient resolution to capture the higher variability at the surface. The RAPID-MOC and MOCHA datasets have a higher degree of vertical resolution than the historical mooring arrays mentioned earlier (as example, Fig.2.7).

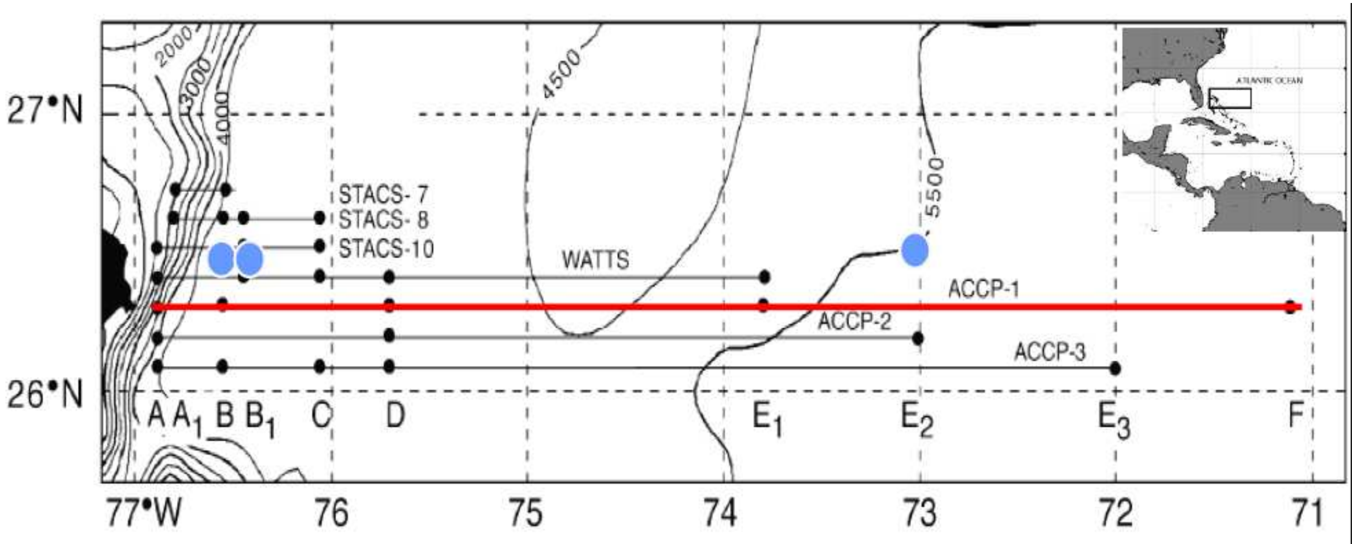

FIGURE 2.5: Positions of 11 year historical western boundary moorings off Bahamas at 26.5 °NW Atlantic. Insert shows the study area in relation to the American coast and the Bahamas Island. Indicated are the historical mooring ACCP-1 (red line) and the current moorings of RAPID-MOC and MOCHA (blue spots) at WB2, WB3 and WB5, adapted from Bryden et al. (2005a).

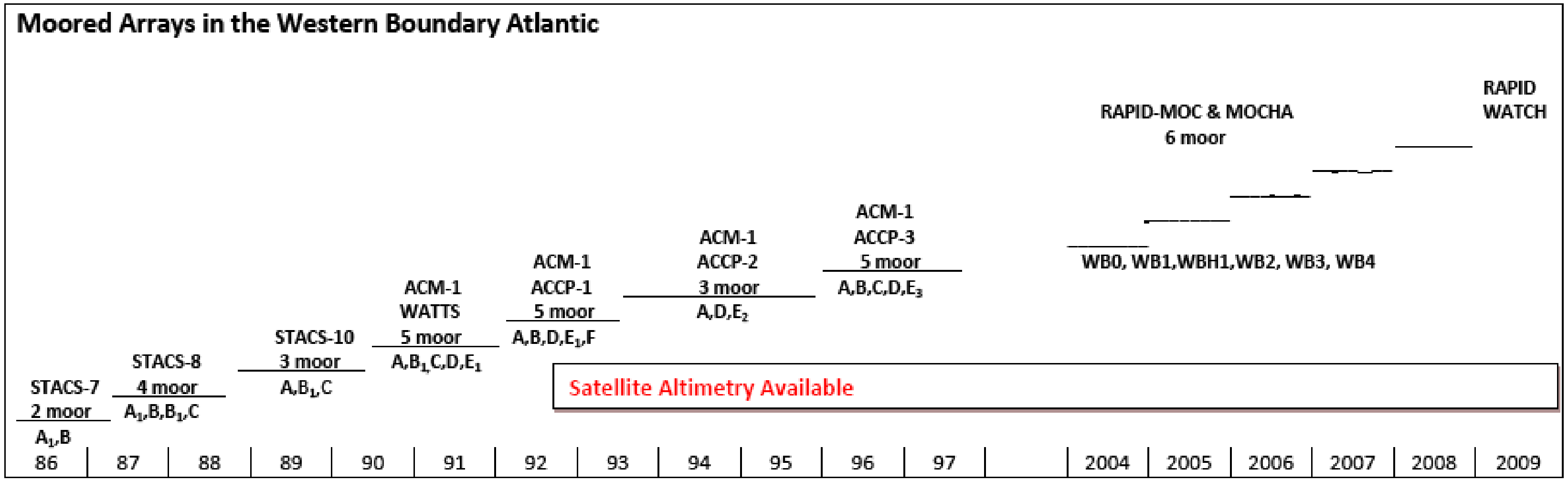

FIGURE 2.6: The different time series available from historical moorings off Abaco between the years 1986 to 1997 and present RAPID-MOC and MOCHA moorings from 2004 to 2008 which coincide with satellite altimeter dataset.

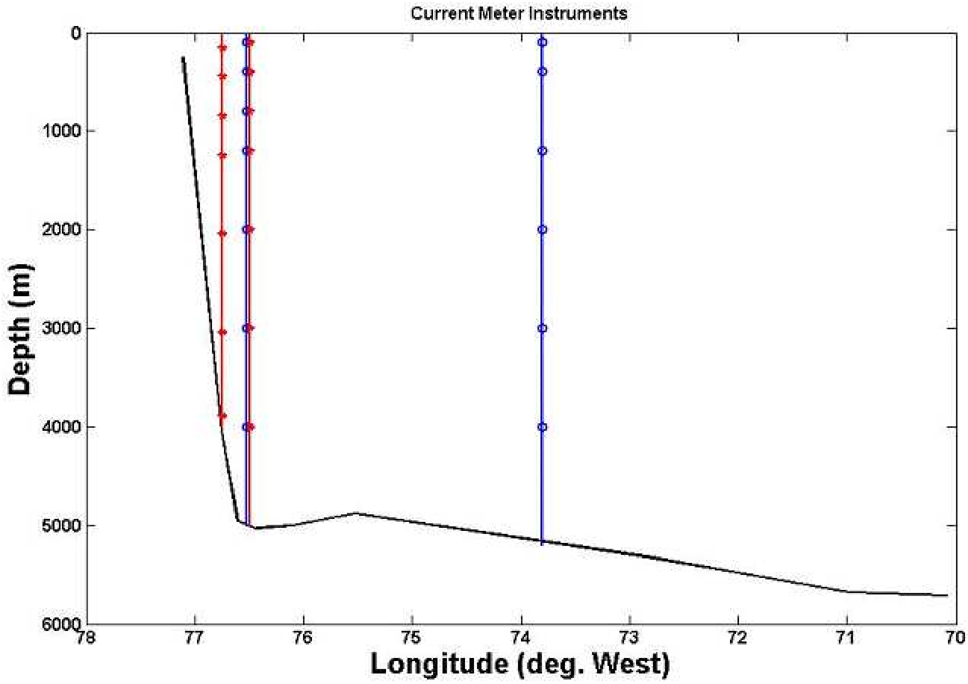

(a)

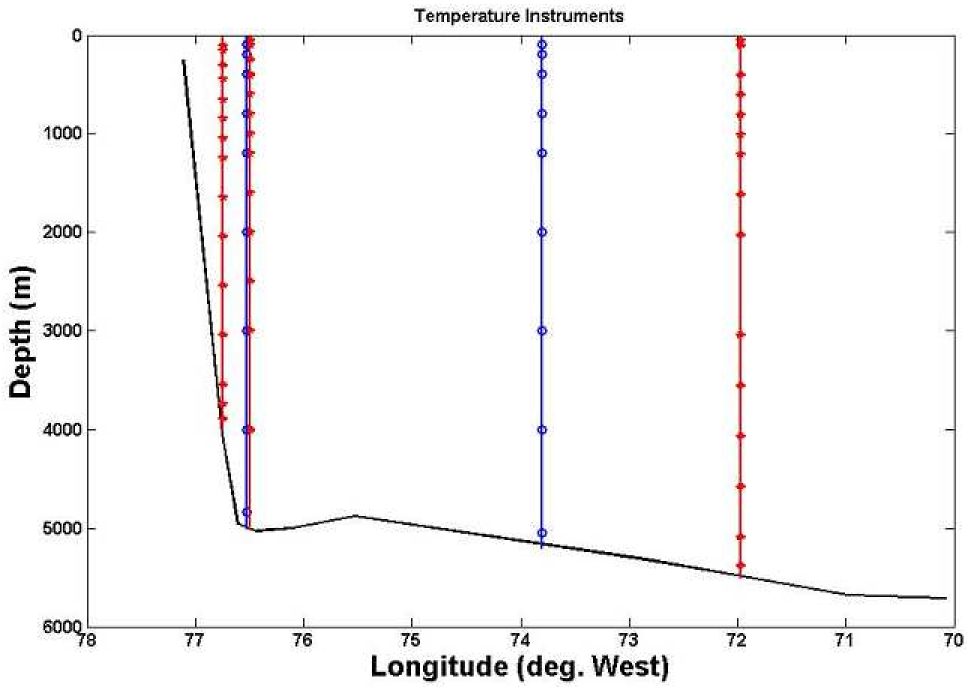

(b)

FIGURE 2.7: Full depth resolution for WB2 and WB3 array (red) and the ACCP-1B and ACCP-1E historical array (blue) of: (a) velocity current meter instruments; and (b) temperature instruments.

2.3.2 Florida Straits Transport Datasets

The Florida Current Transport Programme (FCTP) aims are to monitor the Florida Currents at 27 °N between Florida and the Bahamas, which flows through the Straits and eventually forms the Gulf Stream (Mooers and Fiechter, 2005). The primary measurements are voltage from disused submarine telephone cables that run between Miami and the Grand Bahama (Baringer and Larsen, 2001). The northward flow through the Florida Straits (T) is determined by measuring the voltage across the cable. This is possible as the current's salty seawater can conduct electricity, and when an electrical field is generated by the charged particles in the seawater passing through the Earths magnetic field (B), this field then induces a voltage (U) in the submerged telephone lines crossing the Florida Strait. The sub-annual shipboard calibrations are used to calibrate the measurements and the induced voltage can then be used as a continuous indicator for the strength of the ocean current through the straits.

Submarine telephone cables from FCTP provide an important supplement to the mooring array time series representing the Gulf Stream flow within the Florida Straits. This programme is funded and managed by NOAA (National Oceanic and Atmospheric Administration) and AOML (Atlantic Oceanic and Meteorological Laboratories). Daily time series data is freely available for download online from the official FCTP website (*http://www.aoml.noaa.gov/phod/floridacurrent/*). Datasets available from FCTP date from 1982 to the present day. The Florida Straits Transport time series had a large gap during the period of 4^{th} September to 28^{th} October 2004 due to Hurricane Frances and Jeanne activity which destroyed the cable measurement recording facilities. No other observations were available at the time due to the severe conditions (C. Meinen, *Personal Communication*) and so it was important for the gap in the data to be filled in order to calculate the overall AMOC. This was filled using interpolation methods as proposed by T. Kanzow and E. Grant (*Personal Communication*). Please see Section 2.6.1 for more information on the interpolation methods used.

2.4 Initial Recovery, Editing & Data Processing

Steps in producing calibrated and final science-quality-controlled measurements from the deployed mooring instruments are now discussed here. Most of the processing of the moored CTD and bottom pressure dataset was undertaken by members of the project in the RAPID-MOC team, whilst most of the processing of the moored current meters and ADCP data were undertaken by counterparts in the MOCHA team. All further data manipulation and calculations done in this thesis utilized Matlab © Software and the various associated toolboxes available for PCs.

Firstly, early processing steps were undertaken, as seen in the flowchart (Fig.2.8), after recovery of the instrument onboard the ship. Stage 0 (Zero) is where raw datasets are downloaded from various binary formats and using manufacturer-provided software as interface, they are processed into ASCII formats where possible (RDI format for ADCPs) and clock offsets are checked (due to setup errors) and time-step corrections are made. The next stage, Stage 1 (One) is where datasets are converted to standard ASCII Rapid Data Base (RDB) formats and named according to strict naming conventions agreed to by the project members for archiving. Here unit conversions into S.I. units are applied, associated data processing control files are prepared (providing information on the depths of the instruments, types of instruments, serial numbers and other various metadata about the time series), and further clock offset corrections are done. In Stage 2 (Two), the trimming of the launching and recovery periods, creation of overview sheets calculating the basic statistics and the producing of summary plots are done.

2.5 Post Processing & Editing

2.5.1 Moored CTD Measurements

Calibration datasets can be obtained from pre- and post- deployment of the mooring instruments. The instruments are attached to a CTD rosette frame and lowered

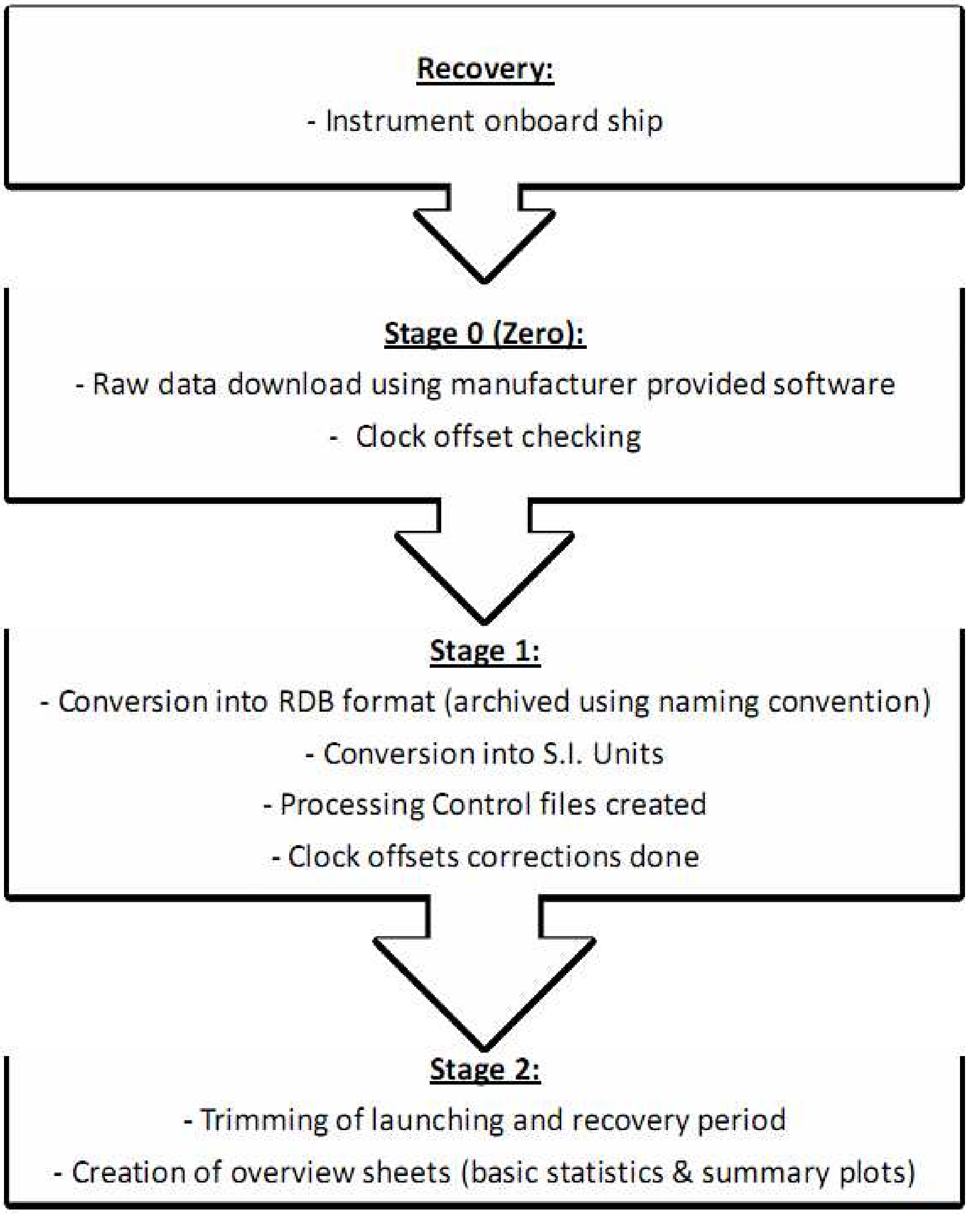

Figure 2.8: Flowchart of early data processing steps after recovery of instruments, to produce Stage 0 to Stage 2 datasets.

to predetermined depths to obtain valuable calibration data used to calculate high quality pre- and post- deployment calibration coefficients for each Temperature (T), Conductivity (C) and Pressure (P) sensors for each instrument profiled. As described by Kanzow et al. (2006) who used the dataset for their calculation of AMOC estimates, calibration of the instruments is essential in order to obtain accurate measurements and minimize the errors. Post-deployment calibration coefficients from the operations are important to determine possible drift (especially for the pressure sensor). Both pre- and post- deployment calibration coefficients can be applied either as an average offset, a linear trend or an exponential trend depending on the sensor and instrument.

The main CTD instrument used was the Seabird SBE37 Microcat with pumped conductivity sensor (specifications as in Table 2.2) and other back-ups were the in-built conductivity cells on the Aanderaa RCMs, InterOcean S4s, Nortek Aquadopps and Sontek Argonauts. The in-built cells provide information on temperature and salinity in addition to the currents at each level. However, back-up measurements from in-built sensors on the current meters are not used when dedicated CTDs are available. Moorings at positions WB2, WB3 and WB5 were to function as end-points for the purpose of inferring geostrophic currents to monitor the time varying dynamic height profiles. High resolution profiles are important at these mooring positions and so, these moorings have CTD recorders at each current measurement level as well as at additional levels throughout the water column.

TABLE 2.2: Specifications of Seabird SBE37 Microcats.

Measurement	Range	Accuracy	Resolution
P (dbar)	7000	7.00	0.14
T (°C)	-5 to 35	0.002	0.0001
C (mScm)	0 to 70	0.003	0.0001

Some redundancies for the CTD records were found in the first year of the RAPID-MOC and MOCHA deployment. On the same mooring, there were a few duplicate instruments at similar depths both able to record the CTD time series. Strain-gauge pressure sensors were equipt on most instruments to keep track of the mooring motion, and therefore the depths of the instruments can be determined at all times. This was especially useful in efforts to determine the best configurations and instruments for this prototype system. Instruments placed in close proximity allow the direct comparison of their performance. Not included in this thesis but previously done were: (i) comparisons of InterOcean S4 versus Aanderaa RCM 11 current meters time series; (ii) comparison of CTD performance between dedicated temperature-conductivity sensors and current meters sensors. In general, the best CTD datasets were from the

Seabird SBE37 Microcats which have higher precision than the in-built CTDs of the current meters. These were used whenever possible for the following analyses.

Depths (in meters) on the instruments are mainly derived from measured hydrostatic pressure, P (in dbars) mentioned before from strain-gauge pressure sensors equipt on nearly all recording instruments. After calibrating, corrections can be made using Commonwealth Scientific and Industrial Research Organisation (CSIRO) seawater routines, as per UNESCO (1983). The standard routines need inputs of the parameters as mentioned individually and besides depth, corrections to potential temperature were also done. There is a nearly linear relationship between hydrostatic pressure, P and geometric depth, z taking into account the latitude (Equation 2.1). It was found that the vertical excursions of the instruments were occasionally very large due to the mooring being dragged down due to strong currents. However, records here have not been corrected for these motion effects as datasets are later grid binned according to associated depth records.

The general form to calculate depth (in meters) is given by the CSIRO seawater routines, where the inputs are P (pressure in dbars) and LAT (latitude in decimal degrees north):

$$depth = sw\_dpth \quad (P, LAT) \tag{2.1}$$

***In-situ* temperature measurements** have been converted into potential temperature, θ, taking into account the internal heating caused by the compression effect of hydrostatic pressure (adiabatic compression). Again, calculations used CSIRO seawater routines (Equation 2.2). T-S diagrams of CTD casts within 200 km of the mooring locations taken during the 2004 trans-Atlantic hydrographic cruise section (Cunningham, 2005a) are used to further calibrate and optimize the moored CTD datasets. Clearly outlying temperature points are removed and the corresponding conductivity and salinity values are set to NaNs.

The general form to calculate potential temperature relative to the reference pressure, uses CSIRO seawater routine where the inputs are S (salinity in PSU), T (temperature in °C), P (pressure in dbars) and PR (reference pressure in dbars) are as follows:

$$ptmp = sw\_ptmp \quad (S, T, P, PR) \tag{2.2}$$

2.5.2 Current Meter (CM) Measurements

The main current meter instruments consisted of a mix of Aanderaa RCM11s, Sontek Argonauts, InterOcean S4s, and Teledyne RDI ADCPs (specifications as in Table 2.3, 2.4, 2.5 and 2.6, with individual measurements of speed, SPD and Direction, DIR). After initial steps, corrections for speed of sound and magnetic variations are done. Most of the current meters (excluding InterOcean S4s and Aanderaa RCMs) were configured with a fixed speed of sound (e.g. 1500 ms^{-1}) and the measured sound speed was obtained using the measured values of pressure and temperature, and the regional values of salinity (35 psu). Corrected velocities are then obtained by multiplying the uncorrected velocities with the ratio of the measured sound speed with the fixed sound speed. Some current meter instruments needed transformation into true east and north components using local magnetic variation. The values for magnetic variation based on the median of the deployment and recovery times of each mooring can be obtained from NOAA's National Geophysical Data Center (NGDC) Magnetic Declination website (*http://www.ngdc.noaa.gov/geomag/declination.shtml*).

TABLE 2.3: Specifications of Aanderaa RCM11.

Measurement	Range	Accuracy	Resolution
SPD (cm/s)	0 - 300	± 1 or % 0.15	0.30
DIR (°)	0 to 360	± 5.00	0.35

Further calculations were then done as needed (such as on the Aanderaa RCM11s) to produce: (i) zonal (East-West) currents - also known as U-component in cms^{-1} (Equation 2.3); (ii) meridional (North-South) currents - also known as V-component

TABLE 2.4: Specifications of Sontek Argonaut MD.

Measurement	Range	Accuracy	Resolution
SPD (cm/s)	0 600	± 1 or % 0.5	0.1
DIR (°)	0 to 360	± 2.0	0.1

TABLE 2.5: Specifications of InterOcean Systems S4AD.

Measurement	Range	Accuracy	Resolution
SPD (cm/s)	0 100	± 2 or % 1.000	0.037 - 0.430
DIR (°)	0 to 360	± 2.0	0.5

TABLE 2.6: Specifications of Teledyne RDI 75kHz Longranger ADCP.

Measurement	Range	Accuracy	Resolution
SPD (cm/s)	0 500	± 1 or % 0.5	0.1
DIR (°)	0 to 360	± 2.0	0.01

in cms^{-1} (Equation 2.4). These were calculated from observed measurements of speed (SPD) and direction (DIR) using the following equations:

$$U = SPD^{*}cos(DIR + 180)^{*}(\pi/180) \ \ \text{unit cms}^{-1} \tag{2.3}$$

$$V = -SPD^{*}sin(DIR + 180)^{*}(\pi/180) \ \ \text{unit cms}^{-1} \tag{2.4}$$

Calculating meridional and zonal currents, from SPD (speed) and DIR (direction)

2.5.3 Dynamic Height(DH) Measurements

Dynamic height (DH) refers to the pressure associated with a column of water from which the horizontal variations in density (from variations in temperature and salinity) can be mapped to determine the dynamic topography and subsequently the geostrophic flow field (flow resulting from the balance between the horizontal pressure gradient and the Coriolis force). The measured vertical density profile time series obtained consisted of datasets from the self-logging conductivity, temperature and depth instruments (CTDs) on moorings distributed vertically to capture the higher vertical density gradient in shallower depths for more accurate interpolation of the density profile. More information of the calculations of DH can be found in Kanzow et al. (2007) and Johns et al. (2008).

DH is defined as the following equation 2.5:

$$DH(p_1, p_2) = \int_{p_1}^{p_2} \delta(T, S, P)dp \tag{2.5}$$

where p_1 and p_2 are the 2 reference pressure levels, δ the specific volume anomaly, T the temperature, S the salinity and P the pressure.

The vertical DH profiles at each mooring site are obtained from the vertical integration of the specific volume anomaly time series. Cunningham et al. (2007) describes the piecing together of DH profiles in the western boundary (from surface to 4820 dbar) and eastern boundary (from surface to 5200 dbar). Following the methodology described by Cunningham et al. (2007) and by Longworth (2007) the geostrophic mid-ocean transport (also known as the local baroclinic variability) are produced. The main moorings used are similar to Cunningham et al. (2007) which are WB2, WBH1, WBH2 and EB1, EBH1, EBH2 and EBH4. Firstly, for each moorings site, the temporal mean DH profile over the sampling year (March 2004 to April 2005) are prepared. Then, the geostrophic velocity anomaly profiles is calculated by firstly calculating the difference between the mean eastern and western dynamic height profiles, then secondly dividing the DHA profiles by the Coriolis parameter, f. Finally by applying vertical integration we obtain the geostrophic mid-ocean transport (also known as the local baroclinic variability) which must balance the mean Gulf Stream plus Ekman transport. Effectively, this constraint sets the mean reference level velocity and mean bottom pressure difference. Here, we can examine the DH anomalies (DHA) of departures from mean profiles at each mooring site and reflect upon the contribution to variability caused by changes in temperature and salinity at the western and eastern boundaries from this baroclinic variability.

2.5.4 Bottom Pressure (BP) Measurements

Listed are the available 15 bottom pressure (BP) gauges distributed from west to east in the first year deployment (2004 to 2005) and among them the 10 gauges used (four near the western and eastern boundary and two on the Mid-Atlantic Ridge) as adapted from Bryden et al. (2009). See Table 2.7 below for further notes on individual BP status, and Table 2.8 and Table 2.9 for specifications of the BP recorders, as in Mujahid et al. (2008).

Long term drift would still be evident in the bottom pressure datasets even after the early processing of de-spiking (see Section 2.5) and the employment of low-pass filtering (see Section 2.6.3) to remove the diurnal and semi-diurnal tides. However, there are a few challenges in removing long term drift (as depicted in Fig.2.9 and 2.10). The drift rate is especially large at the beginning of the records (during the period just after deployment as the sensor adjusts to the deep ocean high pressure, low temperature environment (Watts and Kontoyiannis, 1990)). The fit in the beginning of the records seems to be strongly influenced by any short term fluctuation in the pressure signal datasets. However, it was also found the drifting rate differs between instrument sensors (Fig.2.10) and between deployments. Care is needed to make sure the de-trending effort would not remove any long-period ocean signals. This is especially tricky in the first year of deployment because the signals of interests have similar timescales as the time series obtained (D. Rayner, *Personal Communication*).

Challenges after the first year deployment was to redeploy BPRs at the same levels, further complicating the effort of joining records in addition to sensor drift.

TABLE 2.7: Available Bottom Pressure Recorders.

Mooring	Notes
wb1	geographically unsuitable (shallow)
wb2	used
wbh1	used
wbh2	faulty (inconsistent with nearby records)
wb3	used
wb5	used
mar2	used
mar1	faulty (floated off bottom)
mar3	used
eb1	used
ebh1	faulty (spike mid-record)
ebh2	used
ebh3	used
ebh4	used
ebh5	geographically unsuitable (shallow)

TABLE 2.8: Specifications of Seabird SBE26 Wave and Tide Recorder.

Measurement	Range	Accuracy	Resolution
P (dbar)	6800	0.68	0.20
T (°C)	-5 to 35	0.02	0.01

Kanzow et al. (2006) simulated the error when using discreet single year records compared with two year records with a years overlap and found a significant improvement when using two year records. Because of this, after the initial deployment years, instruments were deployed into separate bottom-landers instead of being attached to each

TABLE 2.9: Specifications of Seabird SBE53 Bottom Pressure Recorder.

Measurement	Range	Accuracy	Resolution
P (dbar)	6800	0.68	0.30
T (°C)	-5 to 35	0.010	0.01

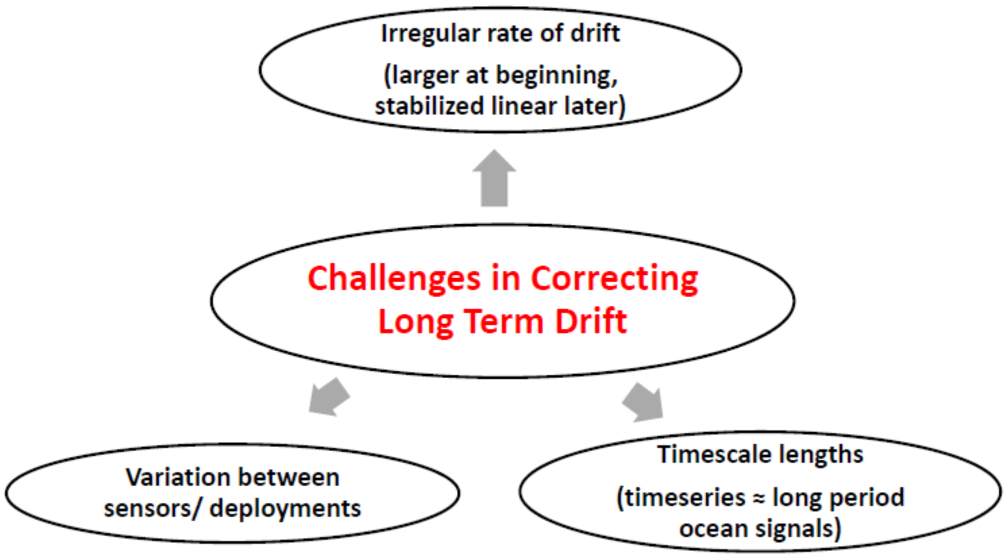

FIGURE 2.9: Challenges in correcting long term drift include irregular rate of drift in records, variation between instrument sensors and between deployments, and similar timescale lengths in time series with signals of interest. From Mujahid et al. (2008).

individual mooring with drop-off mechanisms. The present scheme has progressed to separate bottom-landers deployed for two year periods with a one year overlap at each lander site. Extra data such as these are vital in calculations allowing the levelling between BPRs of subsequent deployments and joining the records for drift removal. This alternative method was found to significantly improve the records. The final bottom pressure records are now overlapping and more reliable long term BP records are overcoming complications due to disjointed records.

There is a difference in fit between the approximated linear long term records to the fit at the beginning of records. The Watts and Kontoyiannis (1990) empirical exponential-linear relationship was used to remove this post-deployment drift in bottom pressure (Kanzow et al., 2006). Calculations to produce bottom pressure dataset

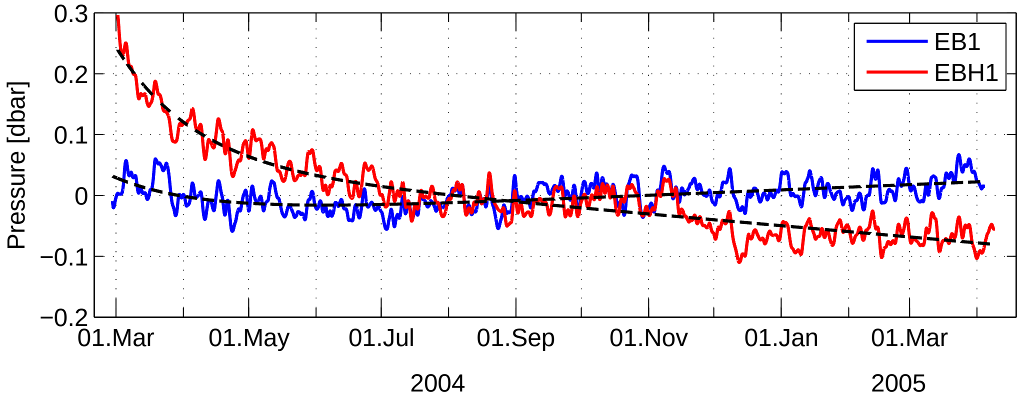

FIGURE 2.10: Example of long term drift in bottom pressure time series at EB1 and EBH1 from the first year deployment as from Kanzow et al. (2006).

where t is time since recording began and A, B, C and D are independent parameters estimated by the least squares as follows:

$$P_{drift}(t) = A(1 - e^{Bt}) + Ct + D \tag{2.6}$$

The estimated M_f 14-day and M_m 28-day tidal constituents of each BP record were also analysed to be subtracted from the individual BP records in addition to the earlier processing (std 0.011 dbar). As the exact depth at each bottom pressure gauge cannot be ascertained, the time-mean pressure was removed to effectively produce the bottom pressure anomalies (BPA) as in Section 2.5.6. For further work involving bottom pressure, low pass filtering of the semi-diurnal and diurnal tidal oscillations (high frequency tides) with the amplitudes in order of 1 dbar and the exponential drift with time as mentioned earlier (about 0.25 dbar) needed to be done.

2.5.5 Sea Surface Height (SSH) Altimetry

Firstly, the determination of the sampling error which exists within the sea surface height (SSH) datasets was identified. We begin by characterising the spatial distribution of the standard deviation (known henceforth in this thesis as std) and sampling error (known forth in this thesis as S.E.).

A spatial map depicting the distribution of the standard deviation of the Sea Surface Height Anomalies (SSHA) between 25 to 45 °N, 10 to 80 °W across the Atlantic basin was prepared as in Fig.2.11. The highest variability can be found at the western boundary latitudes north of 35 °N, increasing at the Mid Atlantic Ridge (MAR) near 40 °W and staying relatively high (due to western intensification). The highest variability is seen to be along-track of the Gulf Stream after it leaves the continental slope at around Cape Hatteras. In the zoomed version of the western boundary between 25 to 28 °N, 70 to 77 °W across the Atlantic basin, we can see the region of relatively low variability stays close to the western boundary, starting approximately around 70 °W but does not reach the extremities of the western boundary (which is 77 °W) and just 'hugs' close offshore along the coast. This is explored further in subsection 5.3.2.

Another spatial map depicting SSHA sampling error is prepared within the same region of between 25 to 45 °N, 10 to 80°W Atlantic, as seen in Fig.2.12. This was prepared to determine if the pattern of relatively low variability close to the western boundary is due to sampling error. We can see the patchy bands of error, with lesser error where the most satellite track crossings occur (i.e. min 0.02 = 2% error) and with increasing error farther from the crossings (i.e. min 0.1 = 10% error). At the coast, the errors increase slightly, but generally, most errors are removed. This is because during collating of DUACS datasets, any SSHA datasets from water depths shallower than 2000 m are discarded (H. Snaith, *Personal Communication*). Zoomed-into the similar region as before i.e. between 25 to 28 °N, 70 to 77 °W Atlantic, we can see that at 26.5 °N the errors are low (2%) at the mooring positions marked in black circles.

The final figure 2.13) shows that at 26.5 °N (in cyan) there is a decrease in the standard deviation of SSH whilst approaching the coast (especially from 25 to 27 °N) whereas the error still remains small and decreases. It is worth noting that the variability seen in the northern Bahamas is likely affected by Gulf Stream variability as it emerges from the Florida Straits. The errors are low (2%) at the mooring positions WB2, WBH1 and WB3 at the extremities of the western boundary which gives confidence that the SSHA time series close to the moorings at 26.5 °N are not significantly

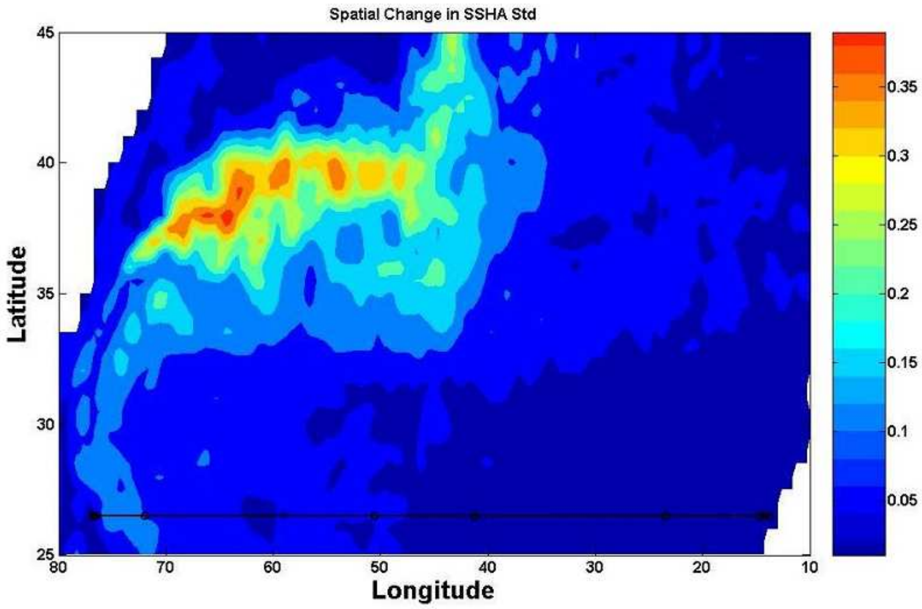

(a)

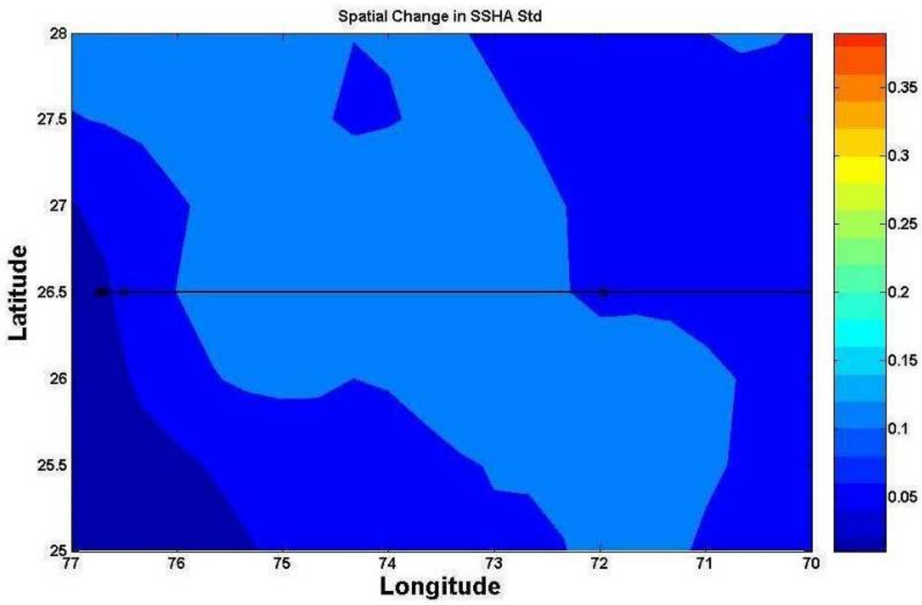

(b)

FIGURE 2.11: Spatial map depicting standard deviation of the Sea Surface Height Anomalies: (a) between 25 to 45 °N, 10 to 80 °W Atlantic which shows the high variability at the western boundary latitudes north of 35 °N; (b) Zooming into 25 to 28 °N, 70 to 77 °W Atlantic. It shows the high variability 'hugs' close offshore along the coast.

affected by sampling error and have reasonably high precision.

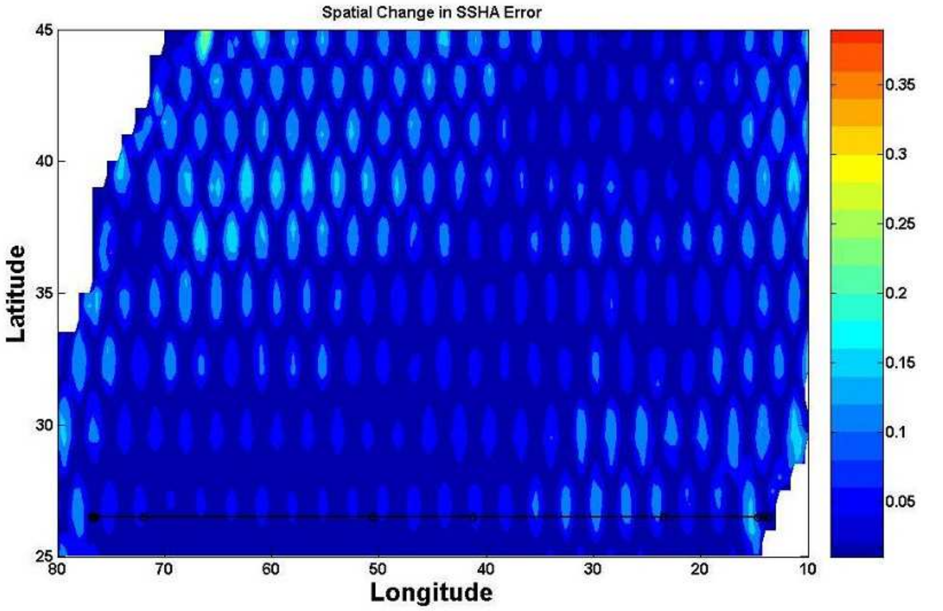

(a)

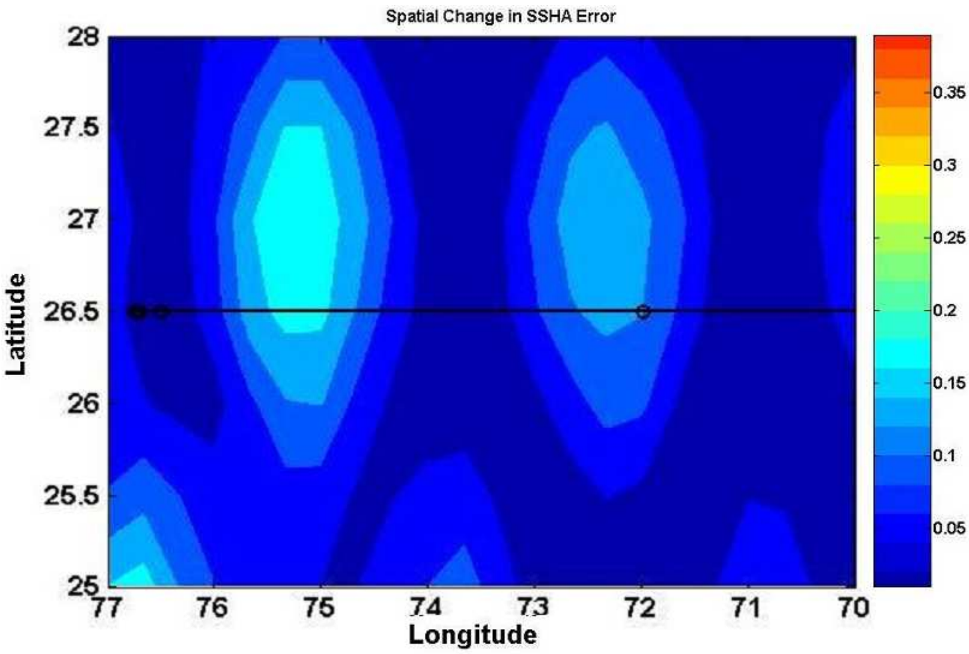

(b)

Figure 2.12: Spatial map depicting errors of the Sea Surface Height Anomalies between (a) 25 to 45 °N, 10 to 80 °W Atlantic with patchy bands of error, and lesser error where the most satellite track crossings occur (i.e. min 0.02 = 2% error) and with increasing error farther from the crossings (i.e. min 0.1 = 10% error); (b) Zoomed into 25 to 28 °N, 70 to 77 °W Atlantic, we can see that at 26.5 °N the errors are low (2%) at the mooring positions marked in black circles.

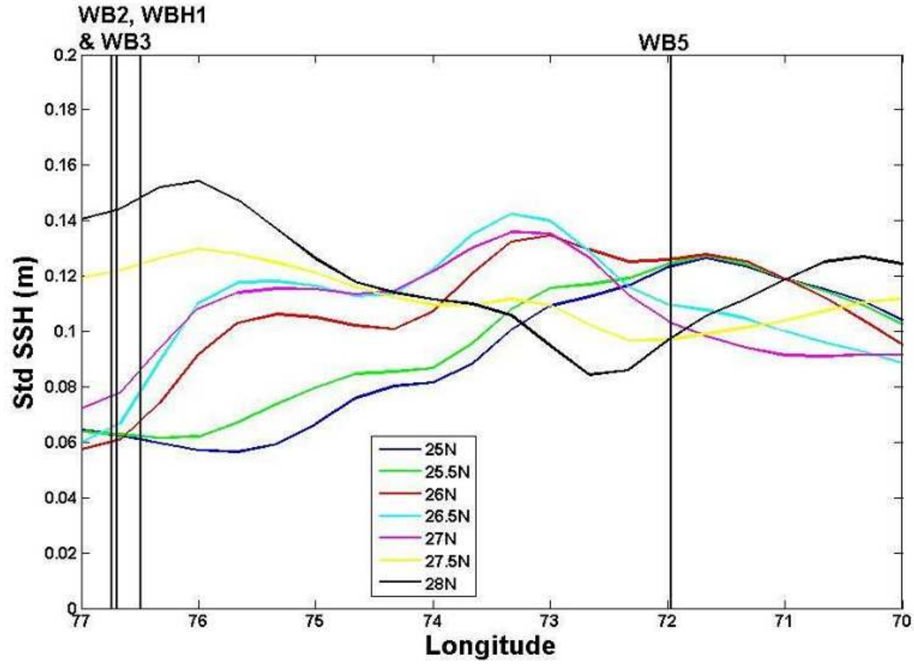

(a)

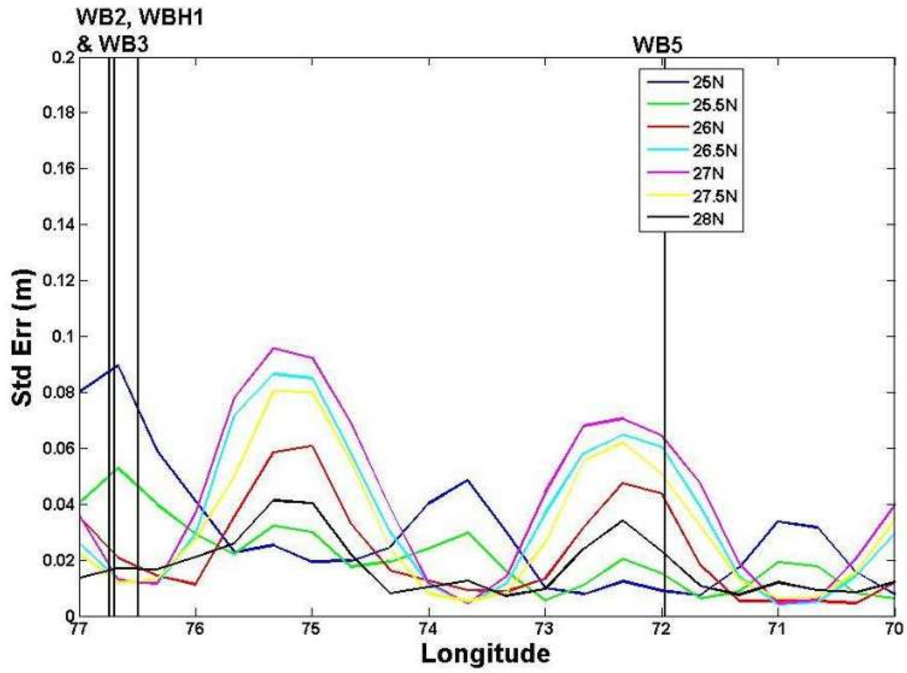

(b)

FIGURE 2.13: (a) SSH standard deviation between 25 to 28 °N, 70 to 77 °W Atlantic which show a decrease in the standard deviation of SSH whilst approaching the coast (especially from 25 to 27 °N); (b) SSH standard error between 25 to 28 °N, 70 to 77 °W Atlantic which also show decreasing error while approaching the coasts.

2.5.6 Surface and Sub-Surface Anomalies

The various anomalies to be calculated, i.e. XA of corresponding 'X' properties such as sea surface height, current speed, temperature, dynamic height and bottom pressure, are representative of change or departures from the long term mean (seasonal cycle of warming/ cooling removed). The anomalies are obtained by subtracting the long term time-mean at 26.5 °N from the daily time series at each longitude (20 to 80 °W). The most general form is as follows:

$$XA = dailyX - mean \quad (dailyX) \tag{2.7}$$

2.5.7 Ekman Transport Datasets

Different sources of windstress data can be used to calculate Ekman transport (T_{EK}). However for RAPID-MOC and MOCHA, daily QuikScat wind stress values were chosen as they provided easily available daily data which were also strongly correlated with National Centers for Environmental Prediction (NCEP) climatology (*http://www.cdc.noaa.gov/*) part of the NOAA NCEP-NCAR reanalysis project. QuikSCAT satellite daily wind-stress datasets were derived from the Sea Winds instrument upon the QuikSCAT satellite mission and can be obtained from the official QuikScat webpage (*http://www.winds.jpl.nasa.gov/missions/quikscat/index.cfm*). Because SeaWinds is a microwave radar, it can measure near-surface wind speed and direction under all weather and cloud conditions.

Ekman transport estimates were calculated in each case in the following Equation 2.8 from Gill (1982). The zonal winds stress values, τ are firstly divided by surface density, ρ and by the Coriolis parameter, f and then finally integrated zonally across the basin the latitude of study i.e. 26.5 °N.

$$T_{EK} = \int \tau/(\rho f) dx \tag{2.8}$$

To match the Ekman transports to the moorings datasets, the dataset was also gridded (method as in subsection 2.6.3) into 1 x 1 ° grids. Standard units for transport, i.e. of Sv ($1Sv = 10^6 m^3 s^{-1}$) are used and so the longitudes were converted into metres as shown by Equation 2.9.

$$\text{Distance (m)} = {}^{\circ} \text{ of longitude x } (111.2{}^{*}10^{3}) \text{ x } \quad cos^{*}(\text{latitude}) \tag{2.9}$$

2.5.8 Geostrophy and Mid-Ocean Transport Datasets

Geostrophy and Mid-ocean (or interior) transports are inferred from density measuring instruments on end-point moorings at positions: (i) east of the Bahamas; (ii) on both flanks of the mid-Atlantic Ridge; (iii) across the African continental slope as in Figure 2.2. Estimates of dynamic height were calculated in each case by following Equation 2.5 where specific volume anomaly is calculated at each depth from measurements of pressure, p, salinity, S, and temperature, T and finally by vertically integrating the specific volume anomaly time series over pressure to obtain the DH profiles at each mooring site at 26.5 °N (subsection 2.5.3).

2.6 Methods

Initial processing using manufacturer-provided software helped with data quality issues (removing spikes and outliers). To further improve datasets, post survey data processing and editing are done but they differ between instrumentation (e.g. moored CTD and current meters), moorings and deployments. Generally, de-spiking is done whereby spikes from datasets are removed if they are 10 times larger than the standard deviation ratio. Other spikes that are identified by visual inspection are removed by hand.

2.6.1 Interpolation in Gaps

Recovery of data during the first year deployment (2004 to 2005) was generally good. There were occasional 'short' errors in sampling for which small gap-filling and smoothing was required. Simple tests comparing various interpolation methods were done and with 'short' gaps (e.g. less than 24 hours or within 50 data-points) the fast and simple method of linear interpolation was found to be appropriate without creating 'false' datasets (Fig.2.14). However, the largest problems occurred on WB2 where current meters had short records due to battery failures. In such large gaps, flag values are inserted. The next step was then to extend the affected dataset using various methods including correlation to nearby instruments. All methods employed are in order to produce calibrated moored instrument time series which can then be low-pass filtered (see subsection 2.6.4) to remove tides and inertial oscillations yielding 12-hourly values.

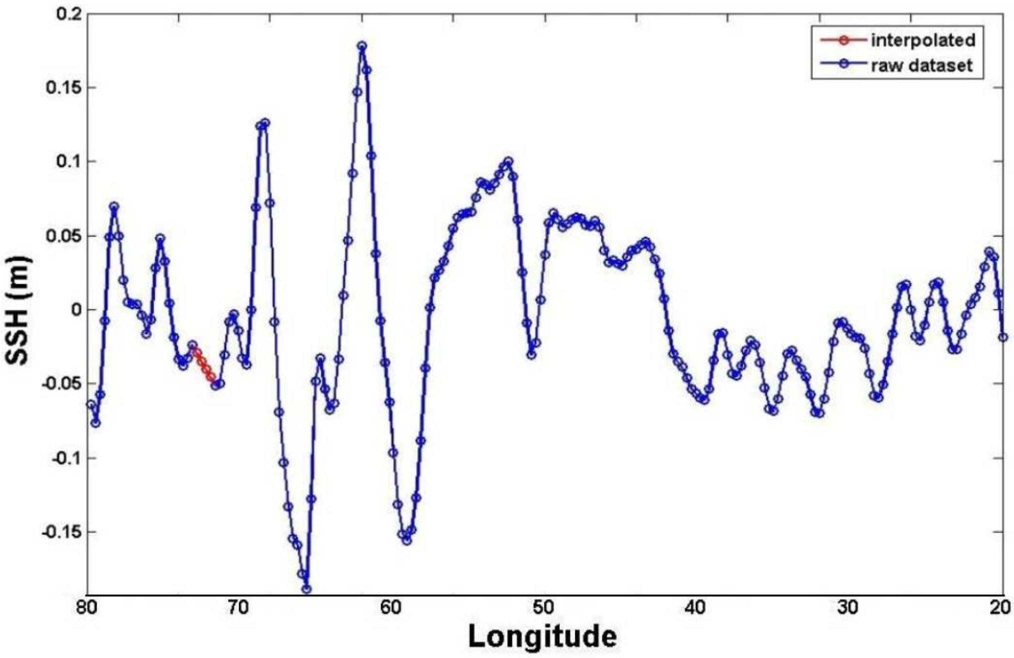

FIGURE 2.14: Linear interpolation of 'short' gaps in dataset. The red line is the SSH datasets points obtained from linear interpolation.

2.6.2 Correlation and Cross Correlation

This method was employed at various stages to determine the predicted statistical relationship between the observed datasets. For example, we first used the method to fill the larger gaps in time series, whereby we used the correlation method to determine the closest correlation to nearby instruments. The method of cross-correlation (or cross-covariance) refers to the covariance between two independent random vectors

(x, y). The product is a vector of values which can measure the degree of similarity between the x and y. Using the Matlab © Software, the function 'xcorr' was used. More details can be found in the Matlab © Software user help manual. In brief, the function estimates cross-correlation sequence between series x and y. The most general form is as the following Equation 2.10

$$[c, lags] = xcorr(x, y, maxlags,' option') \tag{2.10}$$

The first output i.e. the cross correlations sequence, c, is returned with a length of $2^{*}maxlag + 1$ vector, and the second output, $lags$ is a return vector of the lag which indicates at which c was estimated, with the range $[-maxlags : +maxlags]$. x and y are vectors containing the values of a function length, N $(N > 1)$. There is a specified maximum number of lags (in this case '$maxlags$' $= 100$) and a scaling option (in this case '$option$ is identically 1.0. The correlations at 0 lag occur in the middle of the sequence at $maxlag + 1$.

Degrees of freedom (known henceforth in this thesis as d.f.) were calculated using the following Equation 2.11 and significance checked against the standard degrees of freedom table (can be found online in STATISTICA © Software, electronic textbook StatSoft ($http://www.statsoft.co.uk/textbook/sttable.html$).

$$\text{Degrees of Freedom, } d.f. = \frac{N}{ac^2(lag = 0) + 2^{*} \sum ac^2(lag = 1 : Zi)} \tag{2.11}$$

where N are the number of points in the dataset; ac is the autocorrelation function; Zi the point where the autocorrelation function, Z crosses zero the first time; and lag as in the previous equation.

2.6.3 Gridding

Digital filtered data was sub-sampled into datasets of regular time bins of daily samples to form a low-frequency dataset. The vertically irregularly spaced dataset is then bi-linearly gridded into regularly-spaced 20 m bins (or meshgrids) to produce interpolated (and extrapolated) vertical profile time series for further analysis to study the spatial-temporal variability.

For example here, sea surface height (SSH), the method of gridding produces a new finer regularly spaced array datasets of Z values estimated from previously irregular or even regularly spaced XYZ observed values (in this case X and Y being either in space or time) as seen in Fig.2.15. In a case of previously irregular dataset, gridding fills the randomly spaced dataset consistently to create values where no data originally existed by extrapolating or interpolating from the nearby original Z values. In this current case, gridding was done to provide an interpolated Z value of SSH for the mooring positions (which fall in between originally observed gridded spaces) to a higher resolution. There are several methods of gridding (linear or nonlinear, statistical or geo-statistical), each of which calculates the new Z values using a different algorithm resulting in a somewhat different interpretation of the dataset. Also the speed of execution, smoothness of produced dataset and need for more memory in cases of large datasets need to be considered before deciding on the method.

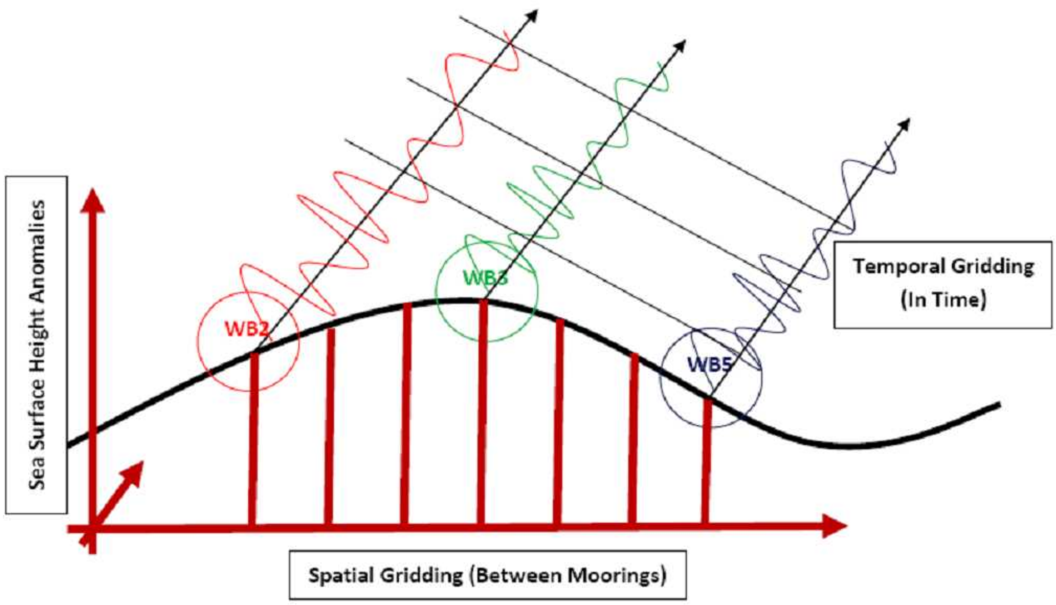

FIGURE 2.15: A depiction of spatial (between moorings) and temporal (in time) gridding within SSHA datasets as an example of the surface/ sub-surface dataset gridding.

The method chosen again was the linear interpolation algorithm to best represent the data. As it is a relatively straightforward method, it is also often thought to be not sophisticated enough to effectively interpolate an irregular dataset to an even grid. However, in this case we are essentially 're-gridding' regular SSH dataset to a higher resolution and this linear interpolation method is sufficiently precise, smooth and continuous. The advantages of this approach outweigh the disadvantages. Amongst the fastest and simplest methods, linear interpolation requires only the knowledge of the two nearest values, and assumes the constant rate of change between them and the new values are found to lie along a straight line between the values of the two nearest original data points. The SSH datasets thus reflects more precisely the SSH at the mooring positions without creation of 'new' or 'fake' points and only depend on the defined linear trend in the data. The one potential disadvantage is the possibility of the original dataset being wrongly reflected in the new gridded dataset as there is no guarantee that the original input data is 'weighted' bearing in mind there is no 'right' or 'wrong' choice. However, this can be overcome by increasing the number of grid point/ lines in the X and Y direction. This would increase the likelihood that the new grid nodes directly overlie the original data during interpolation.

We tested the different possible gridding methods and determined the best solution to be representative of the datasets. For example we can obtain sea surface height (SSH) dataset closest to mooring positions (WB2, WB3 and WB5) by gridding original SSH dataset to a higher resolution (spatially and temporally) using the simple and fast method involving linear gridding as mentioned. The new gridded SSH dataset is representative of the SSH at the mooring positions as they fall within the 'footprint' of the un-gridded SSH nearest to the mooring positions.

Using the Matlab © Software, the function 'interp2' was used where more details can be found its user help manual. In brief, the function performs a 2-Dimensional (2-D) polynomial technique which works to fit the original data with polynomial functions between data points and evaluate the appropriate function at the desired interpolation points. The most general form is as the following:

$$zi = interp2(x, y, z, xi, yi, method) \tag{2.12}$$

Where y is a vector containing the values of a function (the old un-gridded values in x or y i.e. space or time), x is a vector of the same length containing the points for which the values in y are given (the old un-gridded values in z i.e. SSHA). xi is a vector containing the points at which to interpolate (the new gridded values to fit in x or y i.e. space or time). The method is an optional string specifying an interpolation method which in this case is the linear method. This default method fits a different linear function between each pair of existing data points and returns the value of the relevant function at the points specified by xi and yi.

SSHA dataset closest to mooring positions can be obtained by gridding original SSHA dataset to a higher resolution (spatially and temporally) using the simple and fast method involving linear gridding, as seen in Fig.2.16. The new gridded SSH datasets are representative of the SSH at the mooring positions as they fall within the footprint of the raw un-gridded SSHA nearest to the mooring positions.

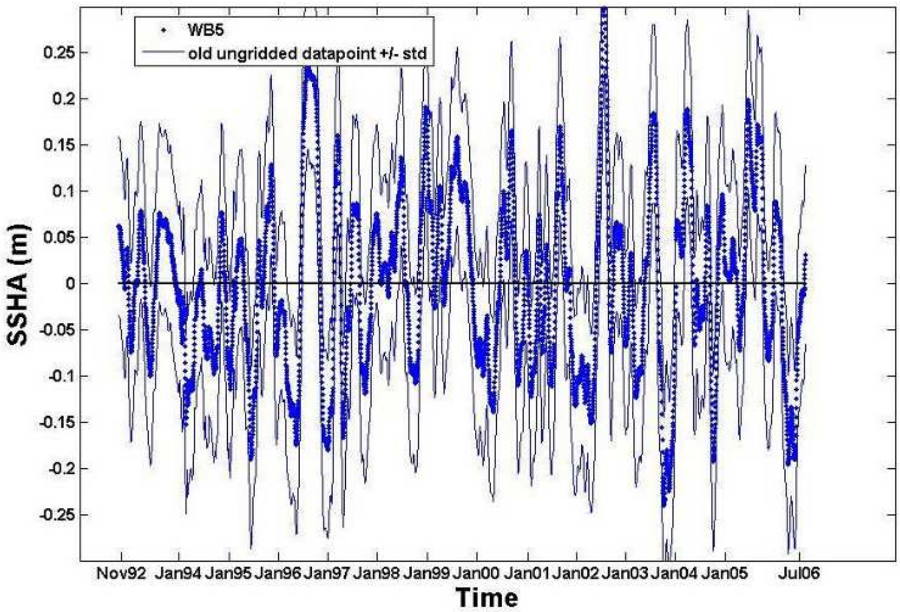

FIGURE 2.16: An example of the new gridded (dotted $*$) WB5 SSHA time series, within the standard deviation of the raw un-gridded SSHA dataset (lined in black).

2.6.4 Low Pass Filtering

The first step after the initial error handling for the mooring dataset is filtering in the time-domain. Previous studies by Lee et al. (1990, 1996) and Halliwell et al. (1991) have shown transport fluctuations to be associated with baroclinic upper ocean eddies propagating westward that modulate the mean northward Antilles Current (AC). Filtering in the time-domain using a two-day low-pass Butterworth digital filter was done to remove fluctuations with periods shorter than a day i.e. fluctuations with tidal periodicities and inertial oscillations.

2.6.5 Westward Filtering

For the DUACS SSH datasets, a common signal processing technique involves the two-dimensional Fourier transform (2D-FT) which reveals the spectral components of the data so that the signal can be examined in the wavenumber/frequency domain. The data is then zero-padded and westward filter function was used to isolate for westward only propagation to variability in the longitude/time plots. The filtered data takes its FFT2 transforms mentioned earlier, and forces the stationary and eastward propagating signals (the second and fourth quadrant in wavenumber/frequency space domain, including the fx, ft axes) to 0 (zero) and taking the inverse transform (G. Charria, *Personal Communication*). This is following methods prescribed by P. Cipollini (*Personal Communication*) and Cipollini (2003). The setup within the grid spacing has 'delc' in decimal degrees and 'delt' in decimal years. 'Annual' removes the signal from spectral bins around the annual peak thus allowing a more effective removal of the stationary quasi - annual signal. 'Hifreq' command removes all frequencies greater than cutoff spatial and temporal sampling frequency to remove high - frequency noise. This was set to a 0.5 cut-off value. Figure 2.17 and Figure 2.18 show the raw SSH dataset before and after westward filtering.

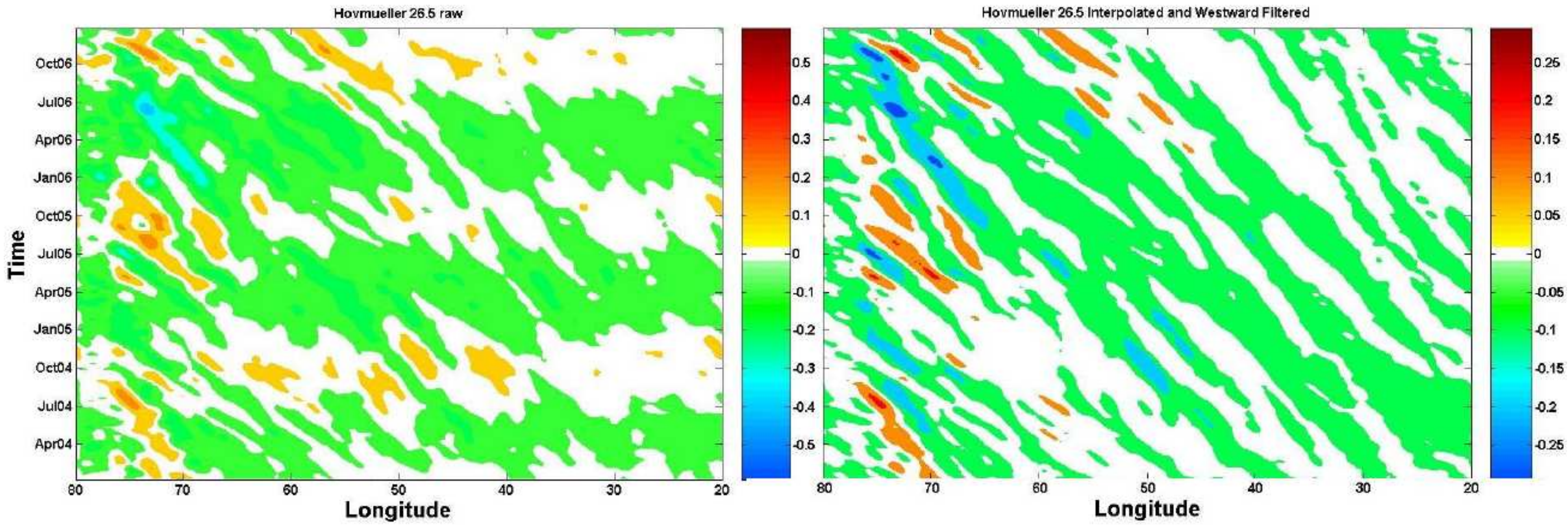

FIGURE 2.17: (left)Longitude/Time (Hovmöller) plot of raw SSH DUACS observations at 26.5 °N, 20 to 80 °W Atlantic.; (right) after interpolating and westward filtering

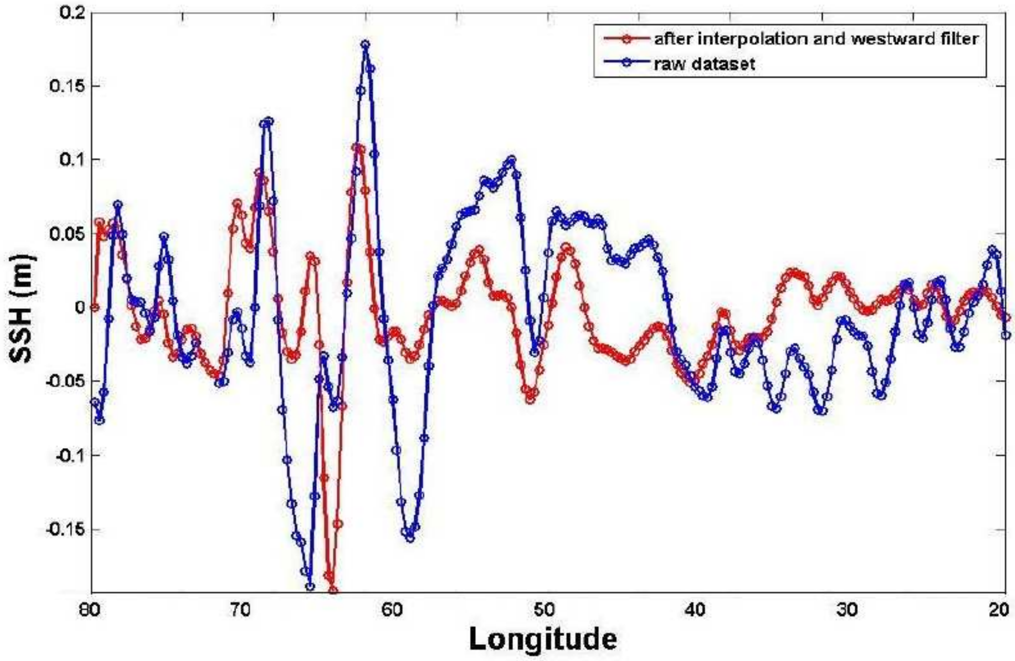

FIGURE 2.18: SSH dataset at 26.5 °N, 20 to 80 °W Atlantic before (blue) and after interpolation and westward filtering (red).

2.6.6 Characterizing Propagating Features

A 2-D Radon Transform (RT) works by computing the Rossby wave propagation speeds from the peaks in std of the RT of Hövmuller (longitude/time) plots. Speeds are computed over a spatial grid, with the ocean-land mask taken into consideration. Peak screening (from mean values) is determined using a method found in Hill et al. (2000) and is expressed as a number of RT std.

2.6.7 Spectral Analysis

The frequency power spectra of the various sub-surface properties have been further considered in an attempt to estimate the forcings and characteristics of the time series especially the contribution to the spectra resulting from large horizontal features.

There is a large spectrum of different oceanic phenomena, with their different associated spatial and temporal scales as reflected in Fig.2.19. According to Kantha and Clayson (2000), the baroclinic Rossby waves and short term climate changes are consistent with fluctuations at the annual to decadal periods which dominate the low-frequency end of the oceanic variability spectrum. The main purpose of time series analysis is to determine the variability in the dataset in terms of its dominant periodic functions. The results will visualise the 'shape' of the spectra and will help explain the dominant modes of the variability which are of interest.

The classical method of FFT (fast Fourier transform), is a common method of using the components from a Fourier analysis to form a periodogram that characterizes the spectral energy density of a time series which determines the main oceanic processes. This was done over a frequency domain (formal transform of the temporal time series) as opposed to the wavenumber domain (formal transform of the spatial time series) which has also been prepared for future use. The classical periodogram (FFT2 of autocorrelation data divided by N, length of series) can be a poor estimator of the power spectrum (limitations such as frequency resolution, poor statistical performance and leakage from rectangular windowing) but from preliminary tests (work not included here) the underlying period and amplitude can be accurately estimated with enough observations. However, to gain a better estimate of the spectrum and accuracy of the period cycle, the method of periodogram averaging (Welch-Bartlett method with Blackman windowing) was used. The Bartlett method works well even with short segments and low variability but smooths and thus loses resolution. The Welch creates an overlap but with a use of a window it can improve resolution even with low variability. Care had to be taken in the selection of windows and segment lengths: to gain better frequency resolution, there is a trade - off in increased variance of PSD. Choices such as a moving average (with segment length of 10 % data length, with overlaps of 40 to 50 %) can 'widen' the window to improve the frequency resolution and statistical performance, whilst using a non rectangular weighted window tackles the leakage problem.

A major limitation here, is the length of the time series. Only 1 year of Rapid *in-situ* observations are used and so we are limited to examining the phenomena with periods of less than a year. For SSH we do have long period (15 years) from altimetry

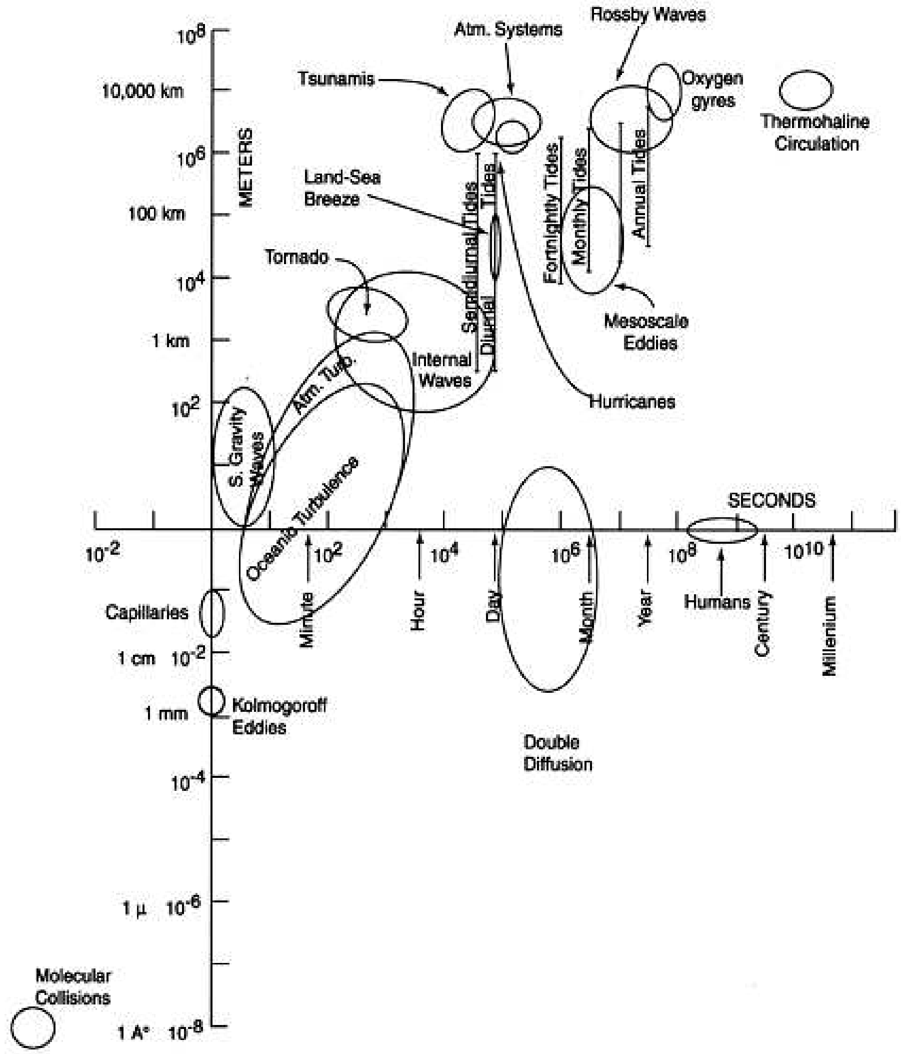

FIGURE 2.19: Range of spatial and temporal scales of motions in the atmosphere and oceans ranging over a 10-decade range in space and time (Kantha and Clayson, 2000).

data sampled at 7 days intervals, and so theoretically, we can study the phenomena with periods of 14 days to 15 years. So within this study, we emphasize westward propagating features (Rossby waves and eddies), which have time scales of 20 to 200 days. We can study both features using the longer altimetry datasets and also the year-long Rapid time series available.

2.6.8 Summary

This chapter in brief highlights the various datasets used and methods employed to obtain surface and sub-surface datasets including the historical datasets in the region of interest which are suitable to be used, the unprecedented high resolution trans-Atlantic mooring array of RAPID-MOC and MOCHA as well as supplementary satellite datasets. We have also covered the steps into basic data recovery, pre- and post-processing and editing of relevant moorings and satellite datasets to obtain high quality dependable data. In brief, we have also explained the methods and analysis techniques employed to obtain the results for further discussion in coming Chapters. It is worth noting again that studies for intercomparison of the performance and errors between various instruments used in the moorings were done but omitted in the thesis.

Chapter 3

The Structure and Dynamics of Low-Frequency Variability

3.1 Chapter Overview

This chapter characterises the temporal-spatial variability of low frequency propagating features. Observations are from altimetry and sub-surface properties of moorings especially in the western boundary Atlantic at 26.5 °N. To aid the understanding of the reader, we first briefly review low frequency variability especially Rossby Waves (RWs) and their importance, to provide a useful outline of the assumptions and present research on RWs. We then determine the quantitative amount or proportion which propagating features contribute to the observed temporal-spatial AMOC variability.

The aims of the chapter are highlighted to simplify the research:

1. To track propagating features from datasets of western boundary 26.5 °N derived from mooring datasets of sub-surface properties and from satellite altimetry.
2. To determine if the short and long term variability in the western boundary 26.5 °N are dependent on propagating features.

3.2 Low Frequency Variability

In recent years, there has been much interest in westward propagation of low-frequency fluctuations especially with the coming and maturity of satellite remote sensing providing a global picture. In most cases these fluctuations are Rossby waves (RW), also known as planetary waves (PW). This is a brief introduction to the present 'traditional' understanding of RW within the oceanographic field. This includes an introduction to the RW theory and mechanisms so we can understand how to study their features and characteristics. We aim to link present methods and tools of observing RW propagation, with advanced tools to characterise and understand their propagation. This is followed by a review of present research especially delving into the discrepancy between RW propagation from observations and models of RW propagation. Finally, we try to summarize present knowledge and determine the importance of observing the vertical structure of *in-situ* datasets in effort to enhance the understanding of the westward propagating features.

3.2.1 Theory and Mechanisms

The theory of RW is well known and further description can be found in Platzman (1968); Kuo (1973); Dickinson (1978); Gill (1982); Pedlosky (1987); Killworth and Blundell (2001). They are fundamental low frequency modes of large scale (hundreds to thousands of kilometers in wavelength) motions found in the atmosphere and the ocean. Their name 'planetary', also explains their origins which are in the restoring force which depends on the variation of the local vertical component of the earth's angular rotation with latitude, the so called beta effect.

In the oceans, they are thought to be generated (i) originally at the eastern boundary by large - scale wind and buoyancy forcing; (ii) over the ocean interior by wind stress variations associated with storms; (iii) by perturbations along the eastern boundaries caused by coastally trapped waves originating at low latitudes. Subsequently, they propagate freely away from their source regions and in some cases can cross the entire oceanic basin westward as they remain non-dispersive to first approximation. The characteristics of observed RW are the solitary wave forms (single 'bump' or trough) they seem to take over large horizontal scales (hundreds kilometers in wavelengths) when propagating westward, following the parallel lines of constant latitude. Global results by Cipollini et al. (2001) and Challenor et al. (2001) indicate this propagation is almost purely westward using 3-Dimensional (3-D) components of longitude, latitude, time in Radon Transform analysis of aligned troughs and crests. This non-periodic wave travels at slow propagation speeds which vary with latitude. The typical order is of a few cms^{-1} (few km per day), and at mid-latitudes (e.g. 30 ° North or South), it could take about four years to cross the Atlantic Ocean (P. Killworth, *Personal Communication*).

The phase speed and property of these westward propagating features can be determined theoretically using the equation for normal modes (full derivation will not be covered here). Simply, the normal mode equation can be derived by standard theory from the linearized equations of motion for large scale, low frequency motion about a state of rest. The equations need specified surface and bottom boundary conditions, and the solving of an eigenvalue problem that depends only on the local stratification. The solutions for this low frequency, long wavelength RW are zonally non-dispersive, i.e. the phase speed is independent of the wavelength. RW have two main modes or types: (i) single barotropic mode; (ii) countable infinity of baroclinic modes, which are summarized in Table 3.1.

Although this special class of waves are ubiquitous in the ocean basins (Chelton and Schlax, 1996; Cipollini et al., 1997), they were difficult to detect until the coming of the remote sensing techniques. The reason that these RW are difficult to observe in the ocean is the unusually large difference in the horizontal and vertical scales. Taking for example the schematic of a 'first-mode baroclinic' Rossby wave (Fig.3.1), we can see that the horizontal scale (wavelength) is of the order of 100's of kilometers whilst the amplitude of oscillation at the sea surface (sea surface height signature) appears as undulations in the order of 10 cm. This rather 'flat' wave profile makes conventional *in-situ* measuring techniques such as ship based 'snapshots' impractical. The few sparse *in-situ* measurements such as those by Jacobson and Spielberger (1998) have been made at the thermocline depth, which show significantly larger amplitude of wave signals.

TABLE 3.1: Comparison of Barotropic versus Baroclinic Modes.

Properties	**Barotropic**	**Baroclinic**
Mode numbers	Single, lowest mode	Countable infinity of higher modes exist due to density variations
Vertical Structure	Uniform vertically	Vertically variable. The first mode (normally most important) is surface intensified and depends strongly on the stratification profile. Horizontal velocity profile changes sign at the depth of the thermocline e.g. first baroclinic mode SSH variations are mirrored as thermocline depth variations, but larger and of the opposite sign (by about three orders, i.e. about 5 cm surface elevation variation would have a 50 m depression in the thermocline). Higher modes have additional changes of sign over depth
Depth dependence	Depth independent	Depth dependent
Propagating speeds	Fast propagating speeds (100 to 1000's cms^{-1}), $\sqrt{gH}$	Fairly slow propagating speeds (few cms^{-1}), decreasing with increasing mode numbers, , $\sqrt{g'H}$

3.2.2 Importance

The importance of RW to the world oceans is generally summarized in Fig.3.2. The main factor is their ability to transmit energy and redistribute momentum across basins. RW also play a major role in maintaining and/or changing western boundary currents (i.e. Gulf Stream) by western intensification of the circulation gyres and by pushing them off their usual course. This simple interaction with large-scale ocean circulation (which transports huge quantities of heat) could lead to an impact on the weather pattern and the climate system with a significant time lag. Some examples are the Jacobs et al. (1994), observations that a RW created from the 1982 to 1983 El Nino traveled across the North Pacific ocean basin for over 10 years, and influenced the Kuroshio Current by driving them northwards. By 1993, the after-effects of 1982

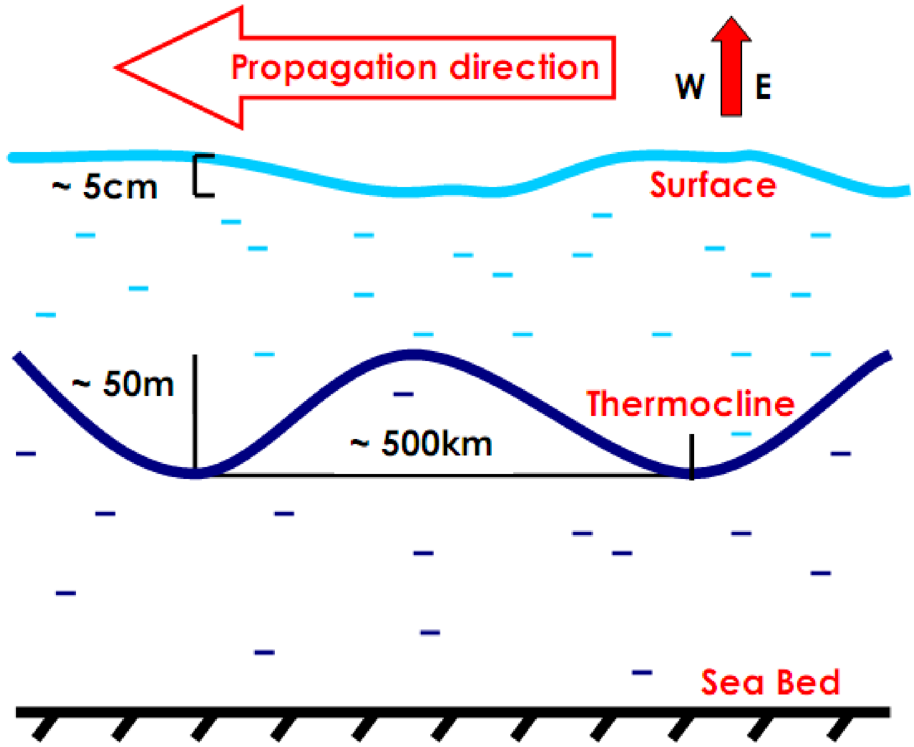

FIGURE 3.1: Schematic of 'First Mode Baroclinic' Rossby Wave, not to scale.

to 1983 changed North American continent weather patterns and may be responsible for events such as the Mississippi flooding (McPhaden, 1994). In the Atlantic, RW and similar physical mechanisms are important to study as they can cause changes to water mass formation and properties (heat and salt) transport within the tropical- to extra- tropical region which play an important role towards climatic changes in the THC (Chang et al., 2006). Besides these, there are suggestions that oceanic Rossby waves act to affect biology, e.g. Charria et al. (2006) as well as act as a 'Hay Rake' for ecosystem floating by-products (Killworth et al., 2004).

3.2.3 Observing RW propagation

A central problem in the study of RW is that there is an accepted theory for the phenomenon but scarce *in-situ* observational evidence for it. Early proof of the existence of baroclinic RW, was seen in variations of the sub-surface isotherm depths e.g. Emery and Maagard (1976), and White (1977). Since then, there have been more *in-situ* observations to prove the existence of RW and their effects, e.g. Jacobson and

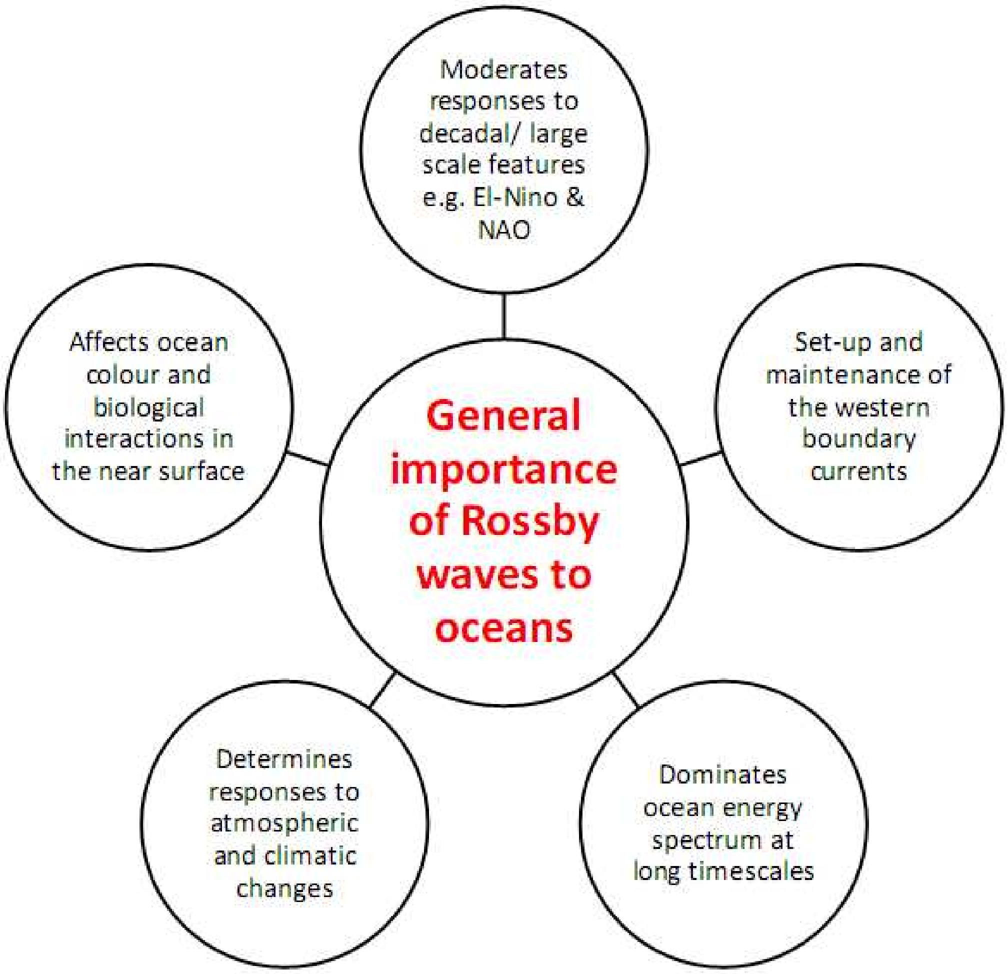

FIGURE 3.2: General importance of Rossby waves to the world oceans.

Spielberger (1998) and Fu and Chelton (2001) in the North Pacific. Pioneering studies such as these confirm the existence of the RW but limitations of *in-situ* sampling failed to provide enough to characterize the large-scale distributions and properties of Rossby waves.

Early TOPEX/POSEIDON (T/P) mission studies revolutionized the observation of RW after the satellite's launch in 1992. The altimeter primarily measures the height (Sea Surface Height, SSH) or sea level. Its global 10-day sampling interval of SSH anomalies was selected to avoid tidal aliasing into frequencies of the large scale oceanic variability. The anomalies are representative of change or departures from the long term SSH mean. Other corrections applied to remove atmospheric effects and variations from the geoid (oceanic signal removed from surface geoid) involve sophisticated processing techniques. Simple concepts and early T/P studies by Nerem et al. (1994);

Wang and Koblinsky (1995, 1996) identified RW in the world's oceans. But Chelton and Schlax (1996) were the first to observe their ubiquitous character, as well as the all important westward propagation of RW in extra - tropical regions and their propagation was faster than predicted by linear theory. Oddly enough, this special group of waves have much been studied theoretically since 1940s, when Carl-Gustav Rossby (Rossby, 1939) theorized their existence, yet there was scarce observational evidence in the ocean for their existence prior to the T/P mission **?**. Thus, it is dominantly the use of satellite remote sensing, which made measurements of RW characteristics (speed, wavelength, and period etc.) possible.

Since 1996, RW studies have moved on to the use of satellite borne radar altimetry e.g. NASA/CNES T/P mission or the ESA's ERS-1 and ERS-2 missions to measure SSH accurately to a few cm. The now standard method of observation is based on plotting Hovmöller (longitude / time) diagrams for a zonal section of SSH anomalies from each orbital cycle (Fig.3.3). This is on presumption that these features are RW which are travelling almost zonally (i.e. from east to west). The contours which slope upwards to the left are taken to represent RW as seen in Fig. 3.3. Some important case studies of altimeter data which have contributed to understanding the characteristics of RW include work by Polito and Cornillon (1997), Polito and Liu (2003) and Fu (2004), not forgetting also work by Chelton since Chelton and Schlax (1996), Chelton and Schlax (2003), and Chelton et al. (2007), which among others began quantifying direction of propagation and its rotation. Other extensive work has also been done by the previously known Laboratory of Satellite Oceanography (LSO) within the National Oceanography Centre, Southampton, especially by Killworth et al. (1997), Cipollini et al. (1997), Hill et al. (2000), Challenor et al. (2001), Quartly et al. (2003) and Hirschi et al. (2009). Further general reading can be found at their website (*http://www.noc.soton.ac.uk/lso/*).

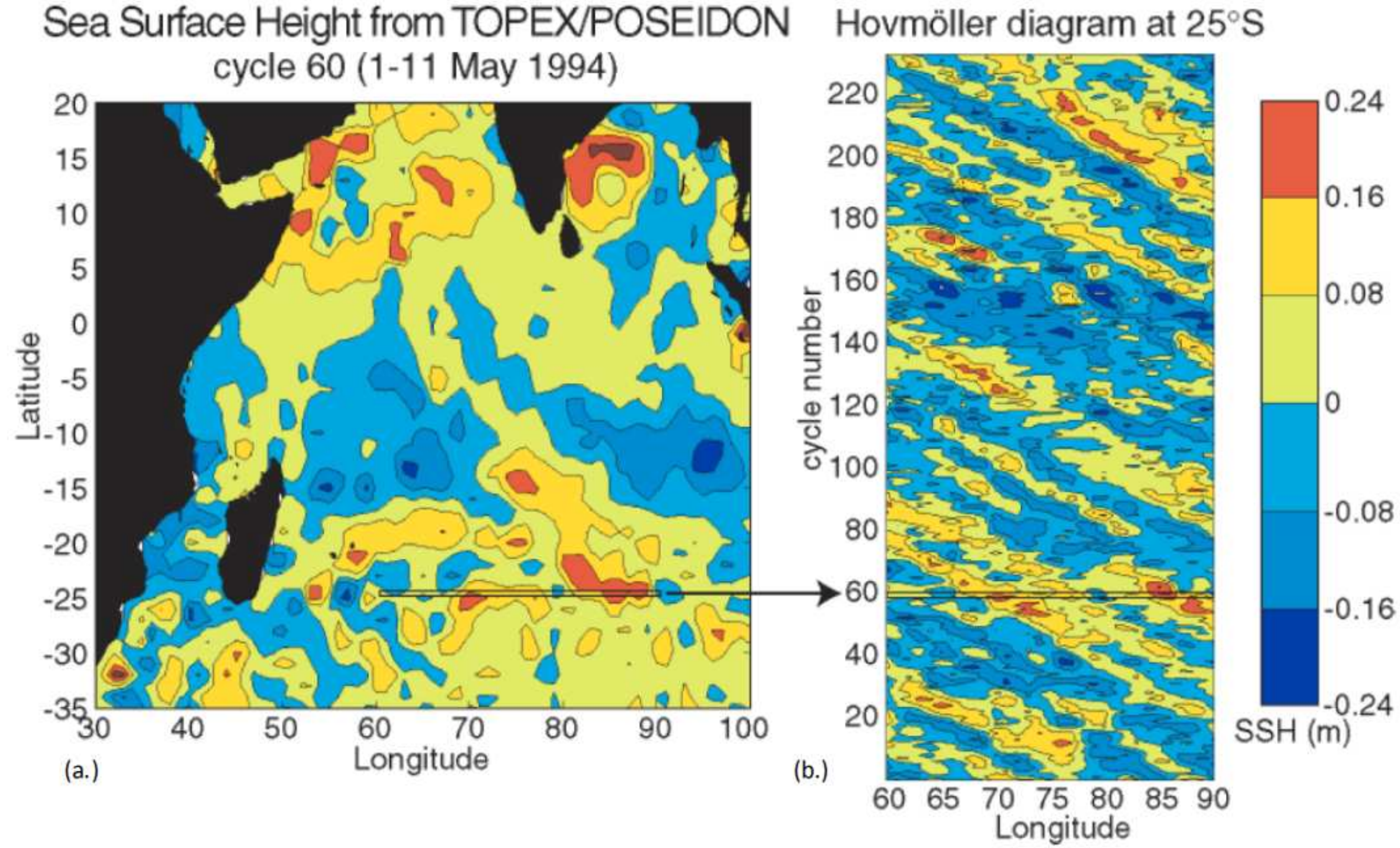

FIGURE 3.3: (a.) Surface maps of Sea Surface Heights (SSH) between Latitudes -35 to 20 °, 30 to 100 °E; (b.) Example of Hovmöller (longitude/time) diagram of zonal section samples of SSH at 25 °S, 60 to 90 °E. The waves are indicated by the diagonal alignment of crest and troughs going from the bottom right to the top left. We can then estimate the waves speed propagation by measuring the slope of the alignments.

Efforts to observe RW signatures within remote sensing have been extended to Sea Surface Temperature (SST) fields from AVHRR (Advanced Very High Resolution Radiometer) on the NOAA - 14 and from the ATSR (Along Track Scanning Radiometer) on the ERS-1 satellite. Cipollini et al. (1997) succeeded in comparing SST and SSH RW signatures at 34 °N in the Northeast Atlantic, proving that simultaneous SST/SSH observations can provide additional information on the modal structure of the waves. Hill et al. (2000) studied the global occurrence of RW using ATSR (referenced with respect to an in situ climatology) and the derived propagation speeds agree well with the predictions of the extended theory by Killworth et al. (1997) apart from some underestimated speeds at latitudes 10 - 15 °S, and at 30 - 40 °S which remain faster than predicted theory. This is probably due to the same reasons as observed in the SSH observations from T/P. Quartly et al. (2003) have also succeeded in finding evidence of RW signatures from SST data from TMI on board TRMM, which are passive microwave radiometers unaffected by cloud. However, observations only capture large scale events (in this case at 32 °S in the Indian Ocean) because the data has low resolution (tens of kilometers).

The study of RW in SST data is important as the thermal signature may not be as direct a representation of their dynamical characteristics as the SSH signals; however the SST signal is a reflection on the coupled ocean - atmosphere interaction. According to White et al. (1998) RW can affect this interaction, and in return have their own characteristics changed. Later, the propagating signals of RW also began to be detected in ocean colour data (Cipollini et al., 2001). Presently, the use of different satellite datasets is commonplace and the techniques to extract information such as the longitude/time plots and the relevant frequency or wavenumber diagram are almost standard (Cipollini et al., 2000b,a, 2004).

Unfortunately the studying of RW with altimetry also has its weaknesses. As mentioned before, there can be many bands of RW with different propagating characteristics. It is worth noting that according to Cipollini et al. (2004), most analysis has been restricted to the extra equatorial or mid latitude RW because their equatorial counterparts (between 5 °N and 5 °S latitude equatorial band) generally propagate at longer spatial scales and faster speeds due to ocean dynamics. These make them difficult to observe in satellite data (lacking resolution) and may require analytical techniques for their identification.

3.2.4 Discrepancy between observations vs. model propagation

Altimeter data offers the possibility to monitor movement or development of features, and by assimilating into models, should provide a key element into future ocean - forecasting system. However, RW can be hard to observe and the already few observations are usually diluted with 'white noise' can be difficult to eliminate and are further affected by other irrelevant dynamical events which need to be filtered out from the dataset. Models can help recreate some observed structures and may help in interpretation.

The idea of using models to compare theory and observation has increased in RW studies, especially for the study of precise mechanisms involved in the formation, speed and propagation of RW, which are still debatable. Realistic or semi realistic models can reproduce known mean circulations and seasonal variations which can help in understanding the importance of different variables (currents, bathymetric relief) as they can be changed with different runs of the model. How it works is that the models have initial conditions set, and then are 'spun up' until all the different strong signals which evolve towards equilibrium for anomalous RW conditions. However, the examination of the RW properties (formation, propagation and speed) are done with models which have current fields and background density structures in quasi-equilibrium with the remote atmospheric forcing.

Model development and analysis begun around the time of Chelton and Schlax (1996) sparked heated debate when concluding that at the mid - latitudes, there was a systematic discrepancy between the propagation of observations versus the predicted linear theory for the zonal phase speed (c_n) of these waves between 1/2 and 2 cycles per year. Various papers then appeared in attempt to explain why the propagation is faster than the predicted linear theory. Qiu et al. (1997) extending a previous study by White (1977) showed that motions which were the sum of a free wave plus a forced pattern could produce apparent zonal phase speeds near $2 * c_n$. Killworth et al. (1997) demonstrated that the presence of mean zonal flows could affect phase propagation in two ways, i.e. (i) through advection; and (ii) through the modification of the mean potential vorticity gradient (which is effectively the index of refraction for the waves). The most promising results to date are in the extended theory by Killworth et al. (1997) which managed to reduce the discrepancy in speed by taking into account the effects of the baroclinic background mean flow. The speeds predicted by this revised theory are in much better agreement with the observation at mid-latitude except for some residual discrepancy in the Southern hemisphere around 30 to 40 °S where the observed SSH speeds are underestimated. Since then, many have extended or clarified the theory. e.g. Dewar (1998); Liu (1999); de Szoeke and Chelton (1999); Zang and Wunsch (1999); Fu and Chelton (2001); Killworth and Blundell (1999, 2003b,a).

It is worth noting that the theoretical models do not specifically have the RW coded into the models and so this comparison of RW from theoretical models versus observations depends on how well the model dynamics are reproduced to reflect reality. The models are only relevant idealizations of the observed RW and are based on many assumptions of basic physics (series of solutions to the equations of motion on a rotating surface with varying surface forcing) which have nothing to do with setting specific adjustments of RW parameters. Instead, if the models and observations disagree, the different underlying environmental parameters need to be adjusted. Examples include: (i) a poor realization of the stratification (henceforth vertical shear) can be caused by weak vertical mixing or too few model layers; (ii) an odd depth structure of baroclinic modes could be an effect of errors in the bottom drag parameters (hence affecting bottom layers); (iii) weak signals or responses due to over-smoothing of the forcing fields; (iv) slow propagation which indicate the inability of the model to represent realistic vertical distribution of velocity and density structures.

3.2.5 Conclusions and Recommendations

We have to bear in mind the major weakness of remote sensing, i.e. its inability to sample sub-surface properties of the RW. The SSHA as seen in the satellite imagery only represent the surface signatures of RW. We can see that the surface signature for 1st baroclinic waves has amplitude reduced by about three orders of magnitude compared to the undulation of the thermocline. The thermocline sited at the bottom of the surface mixed layer is a region of stronger temperature and density change. Satellite imagery cannot capture the structure of the RW at depth. Hopefully, this short introduction to RW has given a fair overview to the theory and mechanism behind this phenomena and its importance to studies of large scale oceanic variability. Methods for studying RW *in-situ* have proven challenging and have been successful mostly using satellite observations. Using models, there have been many attempts to clarify the theory to match the observations, and currently the extended theory of RW propagation is at an optimistic position. However, with satellite observations being limited by sampling frequency, resolution and being a mere 'snapshot' of surface properties, would this be enough in future studies of RW? A representative and realistic vertical structure of RW has also yet to be produced by models. In an ideal scenario, the use of *in-situ* observations can capture the vertical structure of the ocean, at a position where there are known westward propagating features on a long timescale would be ideal to further studies of RW.

The opportunity lies with RAPID-MOC and MOCHA monitoring arrays which have a trans-Atlantic array of 22 moorings (including 9 full depth moorings) in the western subtropical North Atlantic at 26.5 °. RAPID-MOC and MOCHA aim to directly measure and continuously monitor the strength and structure of the North Atlantic Meridional Overturning Circulation (AMOC) as components of the thermohaline circulation (THC). This provides an extensive dataset to study propagating features especially in the western boundary moorings.

There is also great importance is studying propagation in the region. A recent numerical study from Hirschi et al. (2006) suggests that on short timescales there is a clear link between the westward moving pattern for transport anomalies at 26 °N and baroclinic components (similar propagation speeds to those of long baroclinic Rossby waves at this latitude) which could contribute several Sverdrups to the AMOC variability. With recent interest focused on the AMOC (Schiermeier, 2006) and the findings by Bryden et al. (2005b) that the AMOC at 25 °N may have slowed by around 30% - all possible contributions to long term trends must be accounted for including propagating features. And so it is important to study the effects of propagating features such as Rossby waves on AMOC variability. The next question is 'can we observe propagating features in these real-time mooring array datasets as well?'

3.3 Spectral Analysis

3.3.1 Altimeter Sea Surface Height (SSH) Datasets

Here, we performed spectral analysis to determine the dominant scales of variability in SSH datasets. To perform spectral analysis to expected low-frequency propagation, the dataset must have enough observations (extend over a few repeat cycles of the timescales). The SSH dataset spans 15 years. However the mooring RAPID-MOC and MOCHA time series are only just over a year. This is sufficiently long because with the method used (FFT Welch-Bartlett method of periodogram averaging with Blackman windowing), the dominant frequencies can still be picked out, but would be limited by the highest detectable frequency resolved from determining the interval between data points. Results here have been previously presented by Mujahid (2007).

The time varying spectral content of the SSH dataset at position WB5 (Fig.3.4), shows a periodicity of 52 days whilst the inshore positions at WB2 and WB3 both show a periodicity of 241 days. When comparing this to the expected range of temporal scales of motion (Fig.2.19), this would fit the expected scales of the low frequency propagating Rossby waves (months to years). However, it is observed that the dataset, especially in the offshore mooring WB5, are tainted with signals of eddies and the dataset will need to be low-passed filtered at a 30-day cut-off retaining the baroclinic propagation in the SSH signal but removing the higher-frequency variability as per Cromwell (2006).

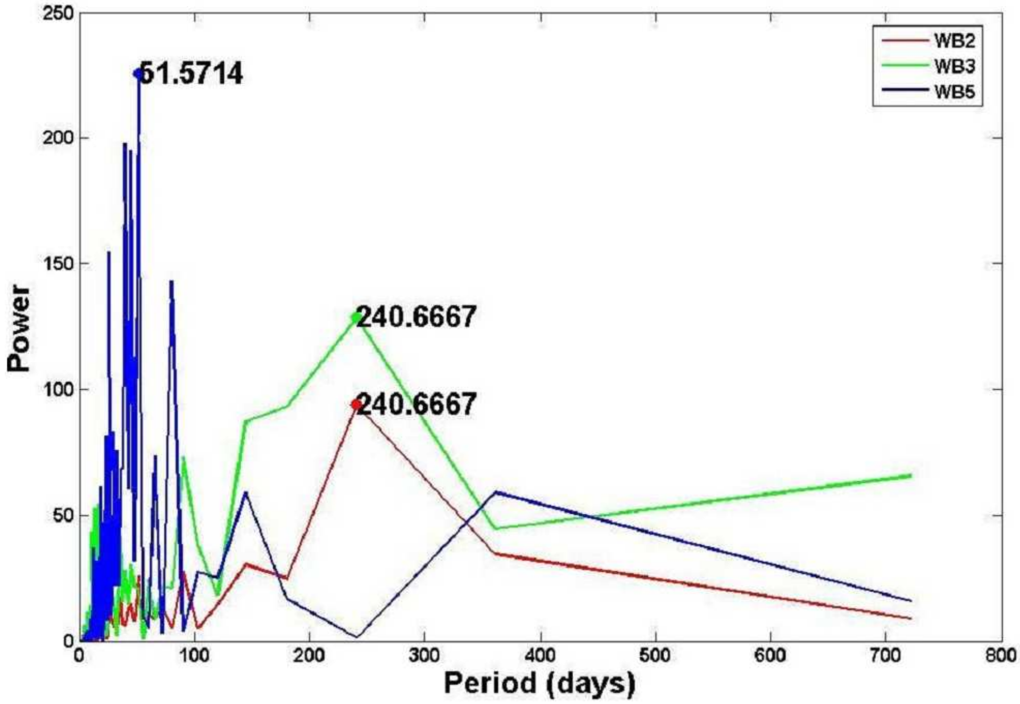

FIGURE 3.4: Periodogram of power spectrum density (frequency domain) derived from SSH datasets between 1993 to 2006. WB5 (Blue); WB3 (Green); WB2 (Red).

3.3.2 Mooring Sub-surface Datasets

For the sub-surface datasets, we have repeated the same method used as before in determining the dominant scales of motion in mooring datasets e.g. (FFT Welch-Bartlett method of periodogram averaging with Blackman windowing). However, in addition the mooring datasets are divided into the AC, upper surface ocean (above 800 m) to represent the Antilles Current and the DWBC, 800 m below (representing the lower deep ocean). In spectral analysis of the meridional velocities (Fig.3.5) and summarized in Table 3.2, we find that at WB3, the AC and DWBC both show the same periodicity of 135 days. For the inshore mooring site of WB2 however, the surface AC has periodicities of 101 days whilst the DWBC was more variable, and significantly different with periodicities of 45 days.

Spectral analysis of the extensive SSH dataset (end 1992 to mid 2006) at the western boundary mooring positions resulted in findings of high frequency variability

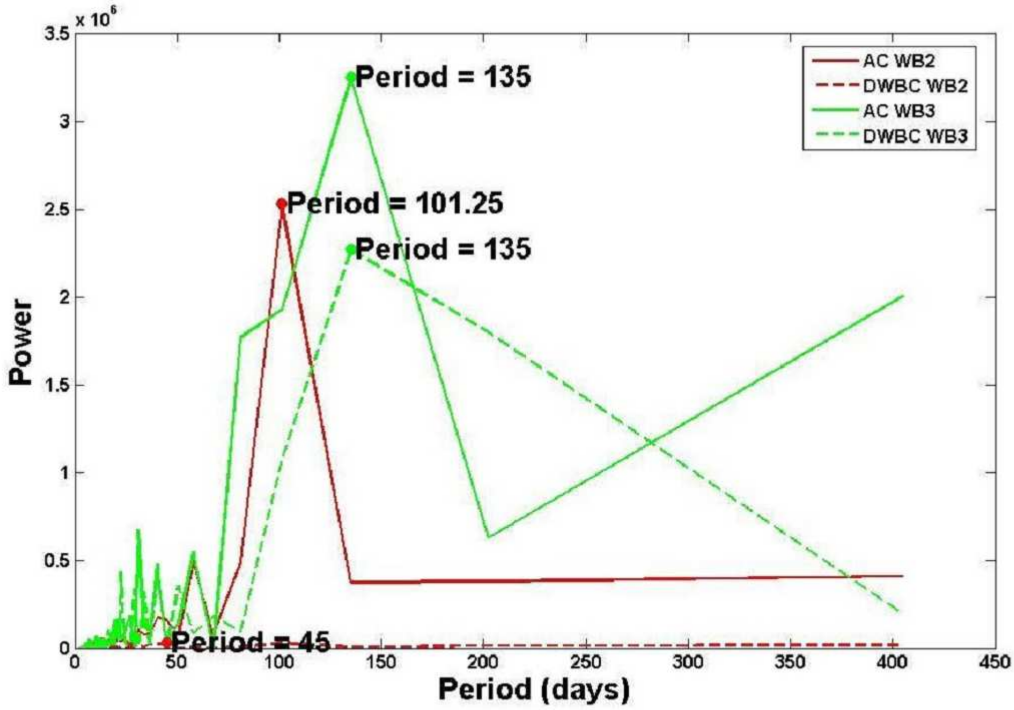

FIGURE 3.5: Periodogram of power spectrum density (frequency domain) derived from meridional velocity datasets between 2004 to 2005. WB3 (Green); WB2 (Red).

TABLE 3.2: Spectral results from meridional velocity and SSH.

Mooring	AC periods	DWBC periods	SSH periods
WB2	101 days	45 days	241 days
WB3	135 days	135 days	241 days
WB5	-	-	52 days

offshore at WB5 (at 52 days), compared to inshore (WB2 and WB3, at 241 days) leading to belief that eddies are affecting the WB5 mooring dataset and must be accounted for whilst filtering. Spectral analysis of the mooring datasets must be undertaken with care because of the relatively short time series. Analysis on the meridional velocity datasets resulted in the highest amplitudes of variability at periods near 135 days at WB3. WB2 on the other hand had highest amplitudes of variability at 101 days in the upper ocean regime, whilst the lower ocean regime had periodicity of 45 days which can be expected considering the effect the meandering of the DWBC. This might be explained by the recirculation encountered at the WB2 mooring site at depth, affecting the DWBC measurements and thus care needs to be taken in interpretation when this dataset is being used. However, we have yet to determine the effect of this result to the overall circulation and further analyses in the vertical structure would be beneficial.

3.4 Spatial-Temporal Evolution of Features in Altimeter Sea Surface Height (SSH) Datasets

We began this chapter by introducing the context of propagating features within the thesis. Fig.3.6 are longitude/time plots (also known as Hovmöller plots) from past and present SSH datasets. We can observe over a large horizontal scale, features of parallel bands from the bottom right to the top left in the figure. These are high and low SSH bands which are 'crests' or 'troughs' of westward propagating features. These can be explained as low frequency, large scale motions of slowly westward propagating features called Rossby or Planetary waves (RW). Observation of the 'tilt' in the horizontal (cross basin) and vertical structure would suggest that the feature may be losing energy to the mean flow as they are propagating westward. It may be the case (as in the atmosphere) that the feature transforms into a mixed RW-gravity (MRG) waves as they propagate westward due to changes in the background state.

Most of the present research revolve around coupled ocean modelling analysis in an attempt to understand such large scale propagation. As mentioned earlier, numerical work by Chelton and Schlax (1996); Dewar (1998); de Szoeke and Chelton (1999); Killworth et al. (1997); Killworth and Blundell (1999, 2001, 2003b,a); Killworth et al. (2004); Killworth and Blundell (2004, 2005), show that propagating features show large discrepancies between observed and predicted propagation. This is because the SSH dataset is limited only to the sea surface and does not take into account sub-surface structure at depths. The vertical structures of these RW are an important yet unresolved problem in oceanography. This makes the study of the variability within the vertical structure of the RAPID-MOC and MOCHA moorings beneficial to further understanding of westward propagation.

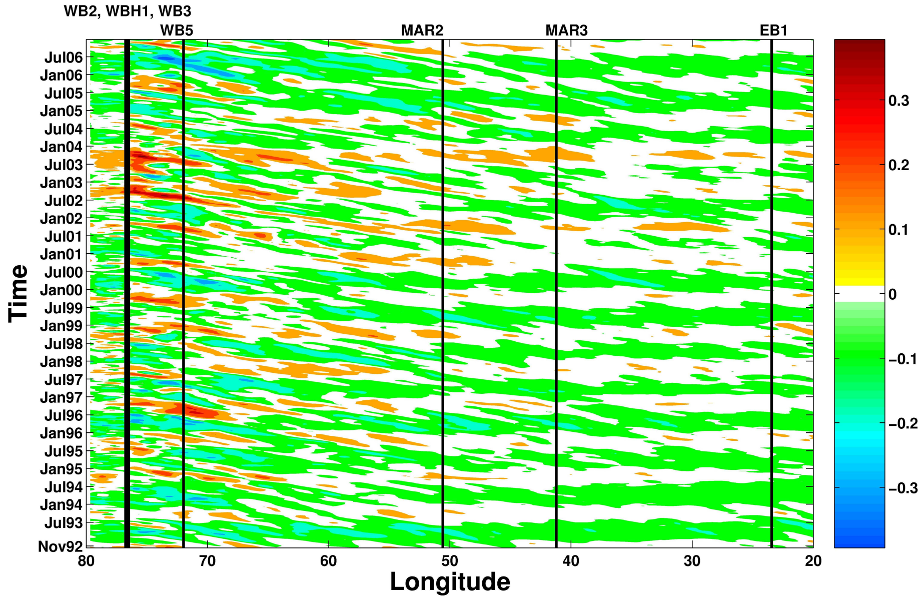

(a)

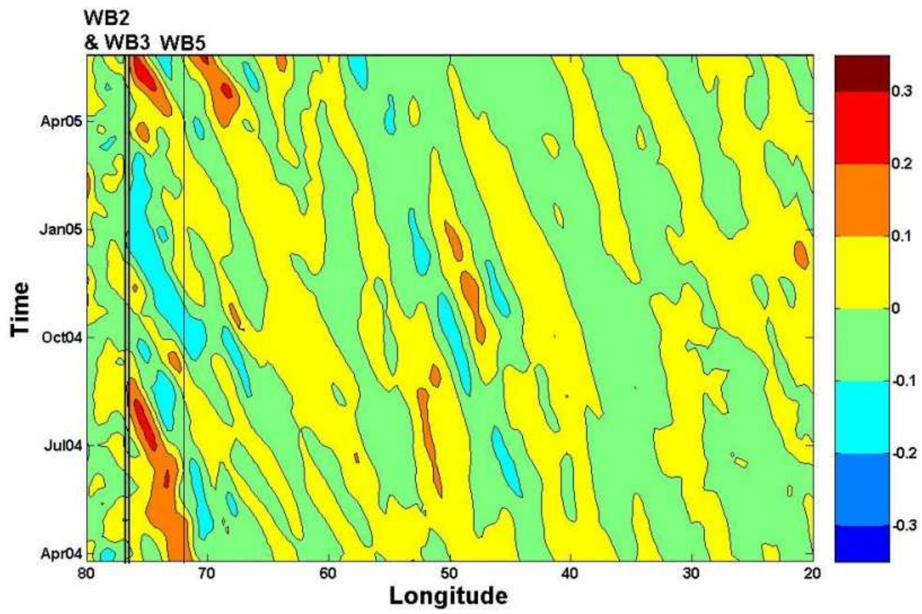

(b)

FIGURE 3.6: Hovmöller plot of SSHA at 26.5 °N, between longitudes 20 to 80 °W: (a) from 'historical' and 'present' DUACS datasets between 1992 to 2007; (b) Zoomed into 'present' DUACS datasets between 2004 to 2007.

We begin by exploring the SSHA dataset to detect events of westward propagation between western boundary moorings within historical datasets from 1992 to 2006. We plot of SSHA time series (Fig.3.7) which compares variability at the Rapid mooring locations WB2 (red), WB3 (green) and WB5 (blue). From visual inspection, the first results show distinct features of crest and troughs (highs and lows of SSHA) through the mooring positions at sub-annual timescales (seasonal cycle removed). Secondly, the patterns of high/ low SSHA between moorings (especially WB3 and WB2) are very similar. Thirdly, the highest or lowest SSHA are found at WB5, followed by WB3 and WB2. The SSHA closest to the mooring WB2, WB3 and WB5 positions were then chosen to enable the comparisons of SSHA between the moorings. Cross-correlation analysis of SSHA between positions: (i) WB2 vs. WB3; (ii) WB3 vs. WB5; were then done (Table 3.3) to determine the approximate time lag according to the highest correlations. This involves creating the normalized autocorrelation sequence. Lastly, the time lag is then considered when shifting the SSHA for visual a comparison of properties of a time-shifted SSHA. This result implies that the variability between WB3 and WB2 is with a maximum correlation coefficient of 0.91 at a one week time lag and between WB5 and WB3 is with a maximum correlation coefficient of 0.33 correlated at a 10 week time lag.

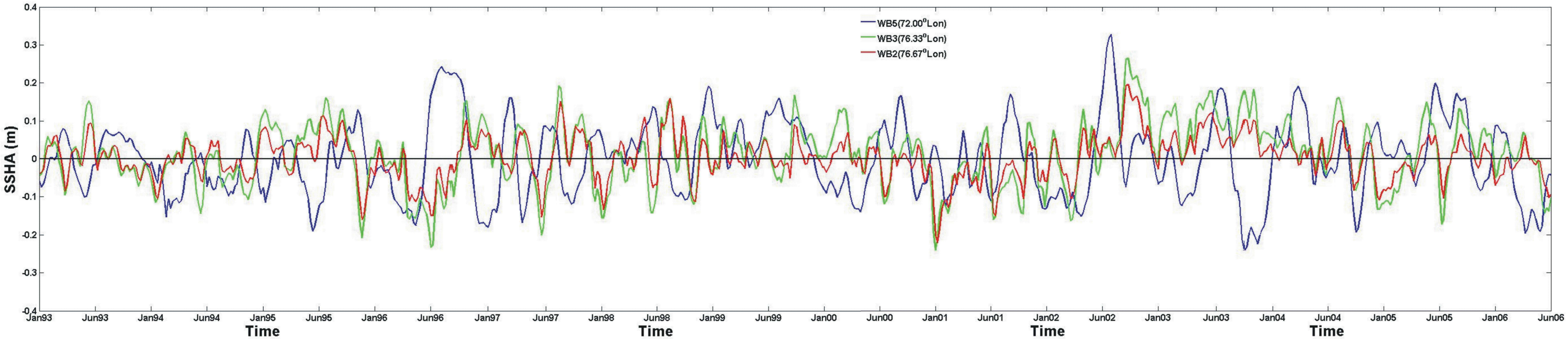

FIGURE 3.7: Historical SSHA time series of WB2 (red), WB3 (green) and WB5 (blue) from 1992 to 2006.

TABLE 3.3: Cross-correlation results of WB3 vs. WB2 as in Fig.3.8(a); and WB5 vs. WB3 SSHA as in Fig.3.8(b), from 1992 to 2006.

Comparison	Highest Correlation	Time Lag
WB3 vs. WB2 also see Fig.3.8(a)	0.9098	1 week
WB5 vs. WB3 also see Fig.3.8(b)	0.3298	10 weeks

We then go one step further by time-shifting SSHA between positions WB2, WB3 and WB5 by their time-lags to directly compare the patterns of high or low SSHA (Fig.3.9). We find features at WB5 (offshore) which do not appear in WB3 or WB2 (inshore). When tracking these propagating features from Hovmöller plots (Fig.3.6), several of these features have a short timescale, travel westward shortly before disappearing (or dissipating) between WB5 to WB3 or WB2 which leads to the conclusion that they are eddies.

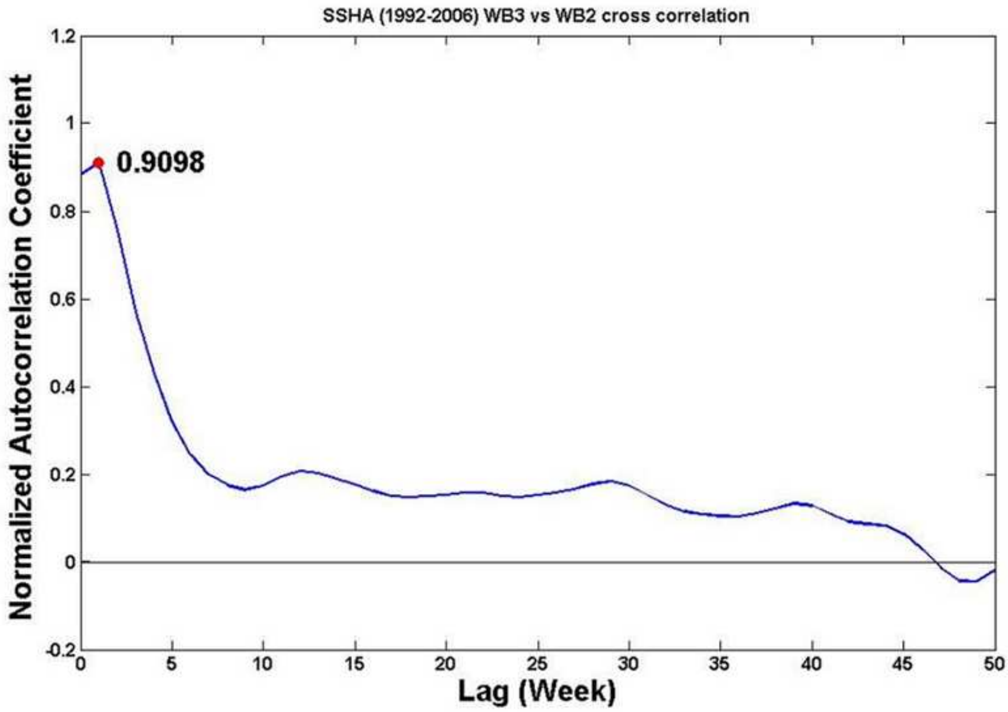

(a)

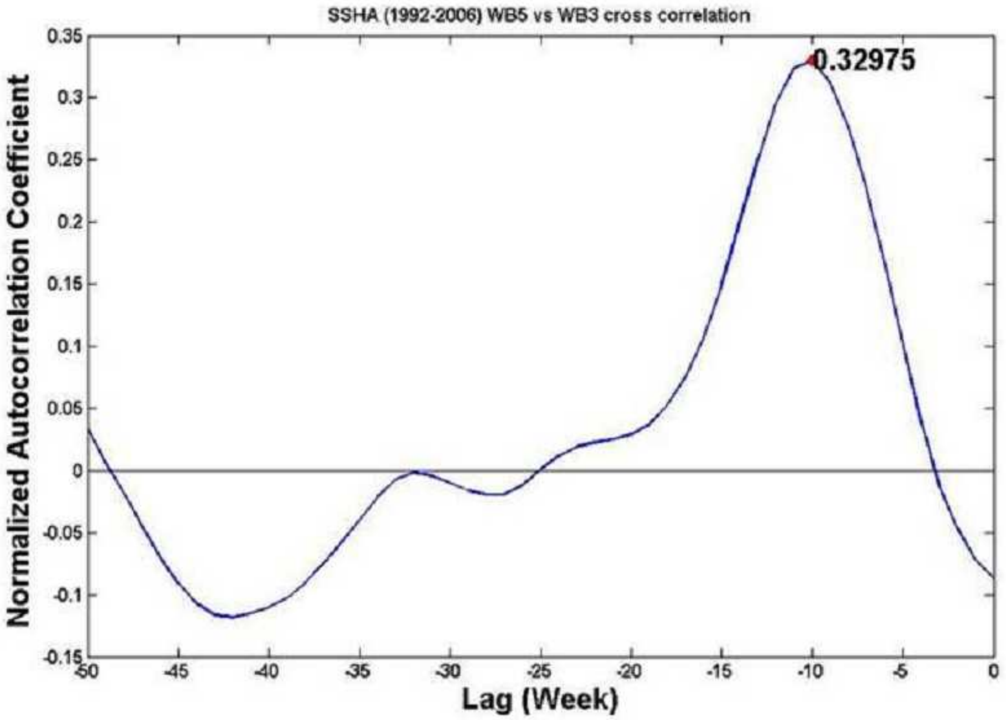

(b)

FIGURE 3.8: Time lag results from cross-correlation of SSHA from 1992 to 2006: (a) WB3 and WB2 with maximum correlation coefficient of 0.91 at a one week time lag; (b) WB5 and WB3 with maximum correlation coefficient of 0.33 correlated at a 10 week time lag.

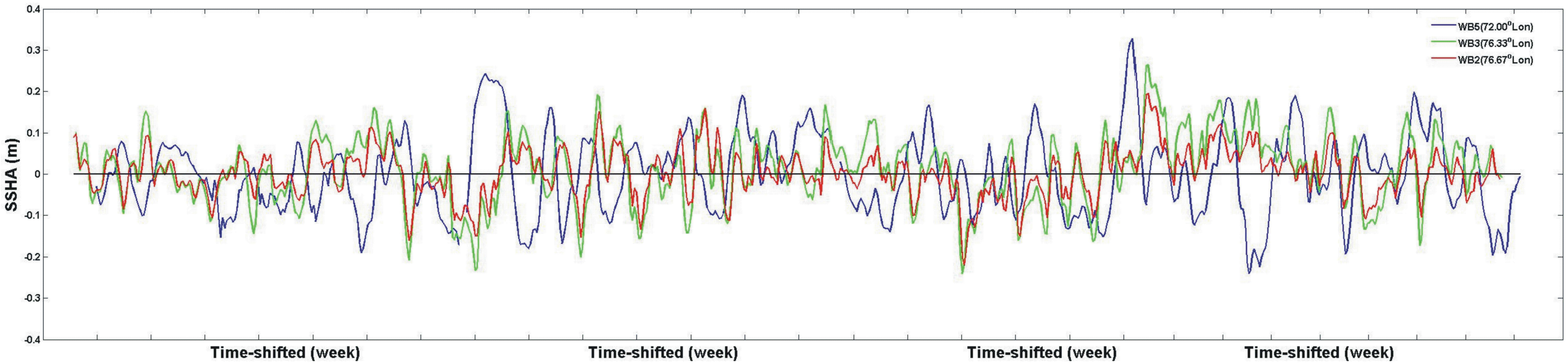

FIGURE 3.9: Time shifted SSHA time series of WB2 (red), WB3 (green) and WB5 (blue) from 1992 to 2006.

The sea surface height anomalies show westward propagation offshore to inshore between the mooring positions. It is reasonable to expect the high correlation between WB3 to WB2 SSHA, as they are in close proximity (just over 37 km apart). WB5 to WB3 on the other hand is over 482 km apart. A qualitative estimate of the mean propagating speed between moorings was done using distance and time-lag. The speed travelling inshore between WB5 to WB3 is average of 10 weeks (6.14 cms^{-1}), and increases speeds by nearly 20% to 7.98 cms^{-1} further inshore between WB3 to WB2. These features can explain a high percentage of the SSHA variability between the moorings e.g. variability between WB3 and WB2 is 91% correlated and between WB5 and WB3 is 33% correlated. This means more than 70% of the cause of variability to the offshore moorings are gone when reaching inshore WB3 only 500 km away. However, the coarse sampling resolution of satellite altimetry (7-day period) makes it hard to determine the significance of these calculations for time shifts of 7 days or less. The comparison of time-shifted patterns, indicates increasing propagation speeds whilst decreasing in SSHA amplitudes from offshore to inshore indicate that the propagating features change as they travel from offshore to inshore moorings. This could be due to many factors including interaction with the bathymetry, localized mean flow or western intensification as a general character of propagating features. However, there might be some other local interaction within the western boundary we need to study further. From earlier figures (2.11, 2.12 and 2.13) we know that the SSHA std is highest at the western boundary at latitudes of 35 °N. The variability is higher close to the western boundary but does not reach close to the coast. In fact, there is a decrease in standard deviation of SSHA close to the coast and as seen in Fig.3.10. This is not due to SSH sampling error which, although patchy, does decrease when close to the coast. The time series of SSHA close to the moorings at 26.5 °N are not significantly affected by the sampling error. Early discussions about the possibility of propagating features dissipating and their dynamics whilst approaching the boundary is further discussed in Kanzow et al. (2009). Studying the vertical structure of flow from mooring datasets can also provide insight to understanding how these features interact with flow in the western boundary and ultimately, their effect on the variability.

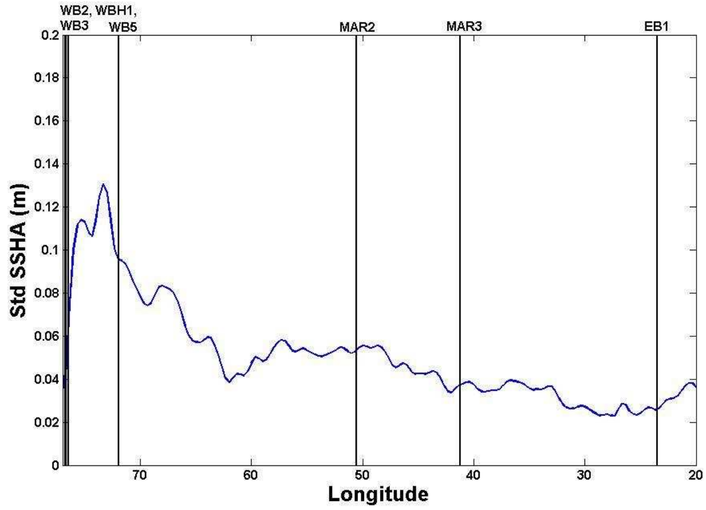

FIGURE 3.10: Standard deviation in SSHA variability at 26.5 °N which show a decrease close to the coast.

3.5 Spatial-Temporal Evolution of Features in Mooring Sub-surface Datasets

3.5.1 Currents and Temperatures

It is important to have long time series measurement in full depth of the various properties as satellites cannot explain everything. The composite of seven day passes does not capture the faster barotropic waves and are almost synoptic for RW over short separations such as between WB2 and WB3. We can supplement datasets using moorings to determine the causes of relatively 'short' events such as in November 2004. Besides that, we are able to ascertain the annual or sub-annual variability, at various temporal-spatial scales in higher resolution. Determining LNADW vs UNADW is also important to explain the overturning circulation patterns and their contribution to the THC as heat transport variability is dominated by velocity fluctuations (Jayne and Marotzke, 2001). The spatial-temporal variability can be studied using the vertical structure of the moorings plotted from the now filtered and gridded datasets from WB2, WB3 and WB5. As mentioned earlier, the vertical structure of the time series from the RAPID-MOC and MOCHA moorings was set-up to resolve the mean flow and capture the spatial-temporal variability to a higher resolution than previously possible. Johns et al. (2008) have compared the mean flow from the moorings with three shipboard-lowered ADCP sections taken coincidentally with the array. They concluded that the features in the Antilles Current (AC) and Deep Western Boundary Current (DWBC) from mooring datasets compared well with the ADCP datasets.

A comprehensive statistical dataset for moorings WB2, WB3 and WB5 was firstly compiled. This included filtered and corrected mean flow, range and standard deviation of zonal and meridional currents as well as temperatures where available. The basic results from figures of vertical structure for meridional velocity and temperature (Fig.3.11 to 3.12), Table 3.4) show highest variations between 50 to 800 m i.e. in the upper thermocline and surface mixed layer. This is expected as the most vigorous motion is driven primarily by wind in the upper 1000 m of the ocean and diminishes dramatically with depth. The main features in the complicated vertical structure are the following components: (i) the upper surface water ocean; and (ii) the lower or deeper water ocean.

TABLE 3.4: Range & mean of meridional velocity & temperatures of WB2, WB3 and WB5

Mooring	Range and Mean of meridional velocities	Range and Mean temperatures
WB2	AC = -20 to 60 cms^{-1}, 13 cms^{-1}, DWBC = 20 to -60 cms^{-1}, 0.6 cms^{-1}	AC = 9 to 27°C, DWBC = 3 to 8°C
WB3	AC = -20 to 60 cms^{-1}, 7 cms^{-1}, DWBC = 20 to -60 cms^{-1}, -17 cms^{-1}	AC = 9 to 26 °C, DWBC = 2 to 8 °C
WB5 a.k.a. BJE	N/A	AC = 9 to 25 °C, DWBC = 2 to 8 °C

The upper ocean near the Bahamas (Rapid mooring sites WB2 and WB3) has an intensified warm northward flow with its core located vertically near 400 m and a steep vertical change in temperature. It is commonly referred to as the Antilles Current (AC) and is a typical feature in the mean flow Lee et al. (1990, 1996); Bryden et al. (2005a). Previous literature by Lee et al. (1996) describes this AC feature as recirculation of

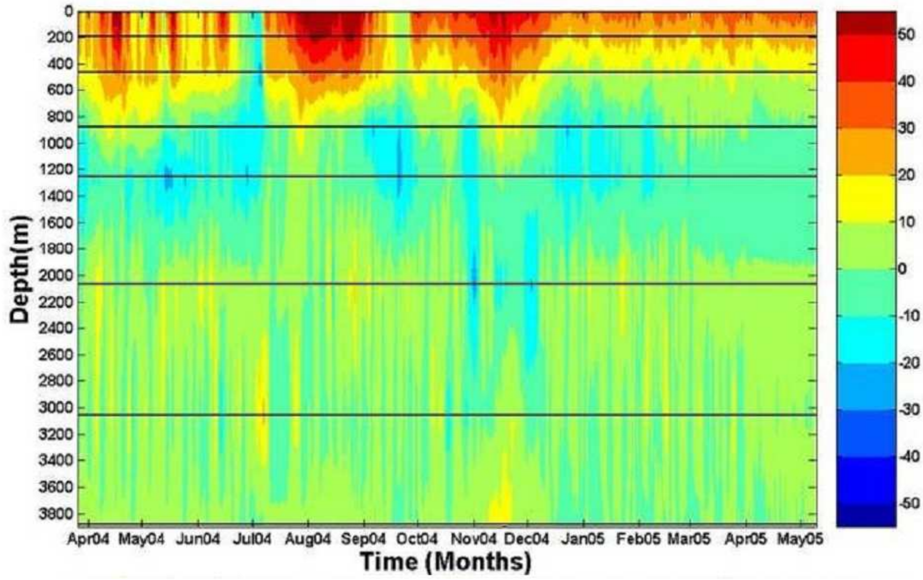

(a)

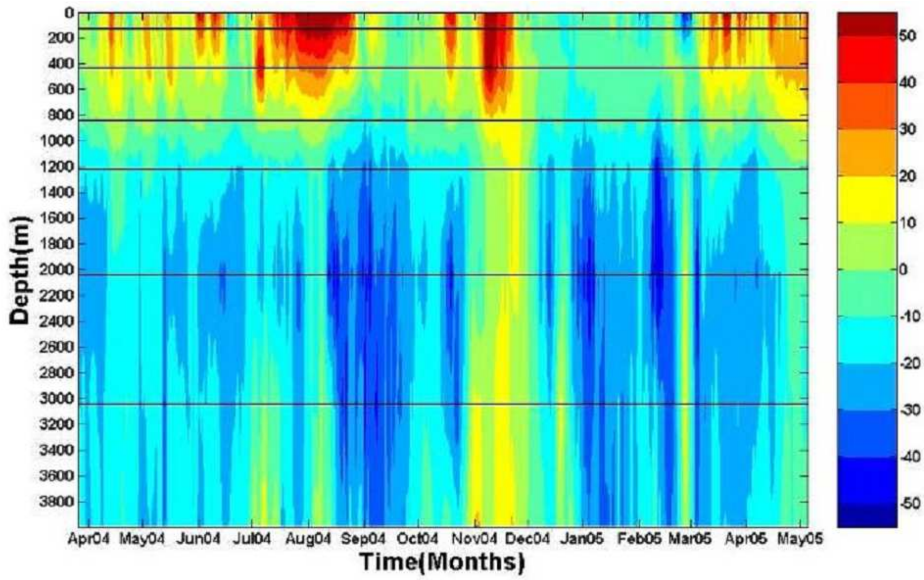

(b)

FIGURE 3.11: Vertical plot of meridional velocity time series from April 2004 to May 2005, (a) WB2; (b) WB3. These show highest variations between 50 to 800 m i.e. in the upper thermocline and surface mixed layer and the decoupled upper/ lower ocean waters.

water in the western part of the North Atlantic subtropical gyre and partly to a more localized gyre or eddy centred just northeast of Abaco. According to Johns et al. (2008), it is a sub-surface intensified current mainly involving subtropical mode water (18 ° water), rather than historical concepts of a semi-continuous surface current of the AC flowing from the tropics to the subtropics e.g. Wüst (1924). The core of northward

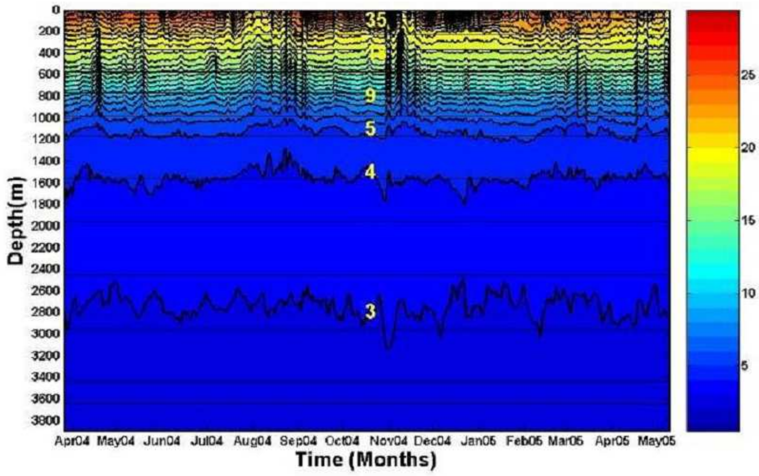

(a)

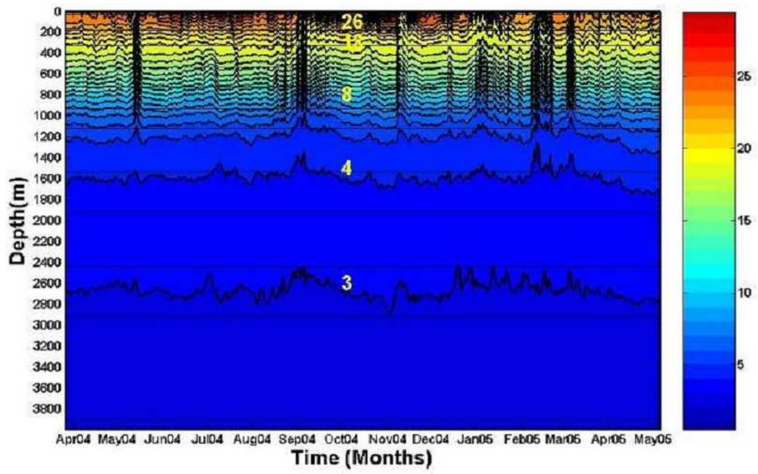

(b)

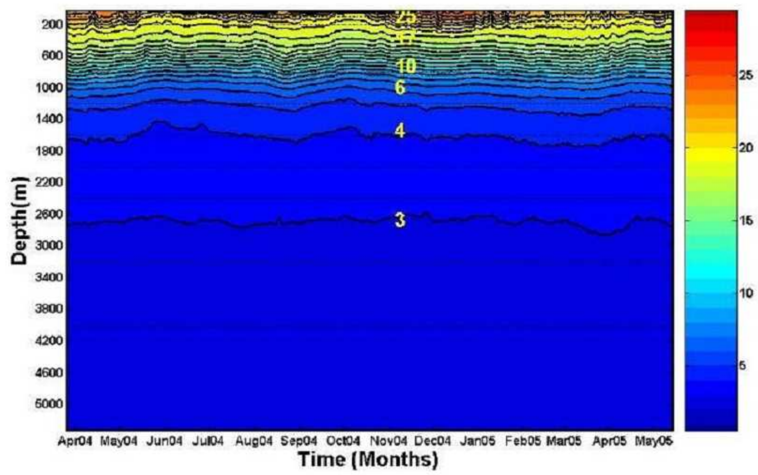

(c)

FIGURE 3.12: Vertical plot of temperature time series from April 2004 to May 2005: (a) WB2; (b) WB3; (c) WB5.

flow AC is more intense (almost double) at WB2 compared to at WB3.

In the lower ocean, below 1000 m, the regime abruptly changes from a warm northward flow to a cold southward flow associated with the Deep Western Boundary Current (DWBC), and with scarcely further change in the vertical structure of temperature. At the WB2 mooring closer to the western boundary (Fig.3.11(a)), the intense core of southward flow is found centered near 1200 m, just at the top of the escarpment and protruding ridge. This feature has been found during shipboard surveys by Hacker et al. (1996) and Johns et al. (1997) but historical mooring datasets e.g. Lee et al. (1990) had wider horizontal separations and so failed to find this feature. Below the intense southward flowing DWBC core, WB2 shows a region of weak and sometimes reversed northward flow which as mentioned earlier, indicates the 'shielding' by the escarpment (Fig.3.11(a) and 3.12(a)). The stronger flow probably represents the upper part of the DWBC which managed to escape the 'shielding'. At the WB3 mooring farther offshore (Fig.3.11(b)), the DWBC is not shielded and the core of the DWBC is deeper and centered around 2000 m. This is consistent with previous results which also show the WB3 mooring to lie close to the mean core of the DWBC (Johns et al., 2008). The meridional current flows southward at a mean of -17 cms^{-1}, except during a few events as explained further.

To reveal the variability clearly, the mean meridional velocity and temperature flow (Fig.3.13) are removed at each depth from the time series to create a time series of meridional velocity anomalies (Fig.3.14) and temperature anomalies (Fig.3.15). The meridional velocity anomalies in WB2 (Fig.3.14(a)) show significant events in the surface currents AC but none at the lower depths as the 'shielding' has significantly reduced any strong DWBC flows. However, in WB3 (Fig.3.14(b)) the DWBC shows a significant event of reversal (or possible 'stoppage') in November 2004, which has velocities of over 20 cms^{-1} to a maximum of over 40 cms^{-1} throughout the water column.

Using the vertical structure of WB2, WB3 and WB5 temperatures anomalies (Fig.3.15) we see the events of high or low anomalies on sub-annual timescales

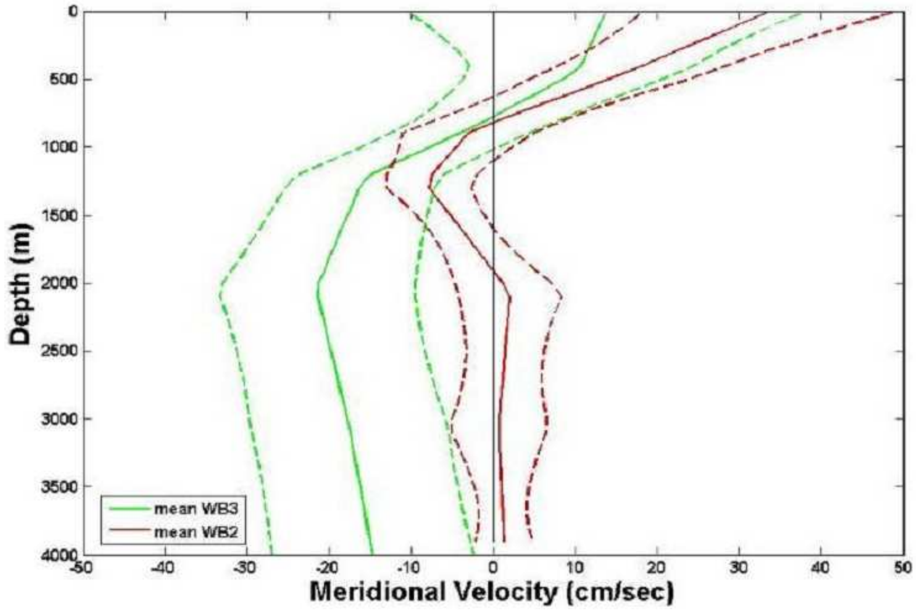

(a)

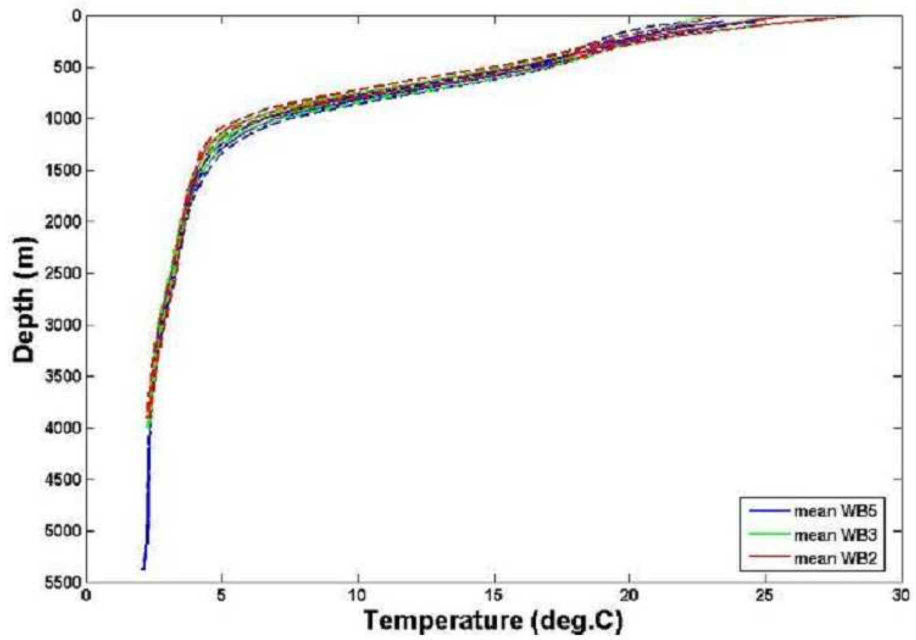

(b)

FIGURE 3.13: WB2 (red), WB3 (green) and WB5 (blue) of, (a) mean meridional flow, $V(z)$; (b) mean temperature flow, $T(z)$. Dotted lines depict standard deviation.

similar to the vertical structure of meridional velocity anomalies. The temperature anomalies do not seem to prevail throughout the water column during the November event (unlike WB3 meridional velocity anomalies). Contours of the temperatures on the other hand, depicted sharp 'dips' in the lower ocean isotherms (see 3 to 4 °C isotherms

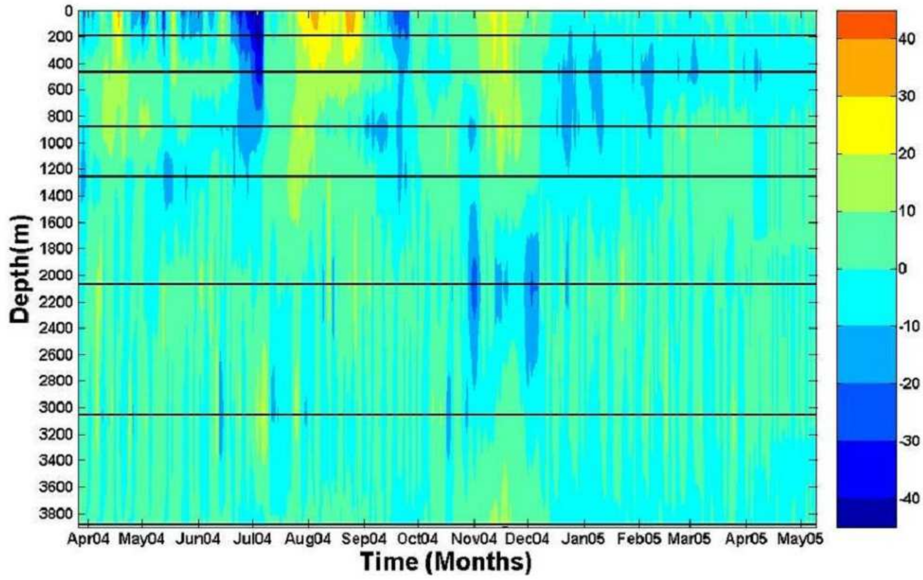

(a)

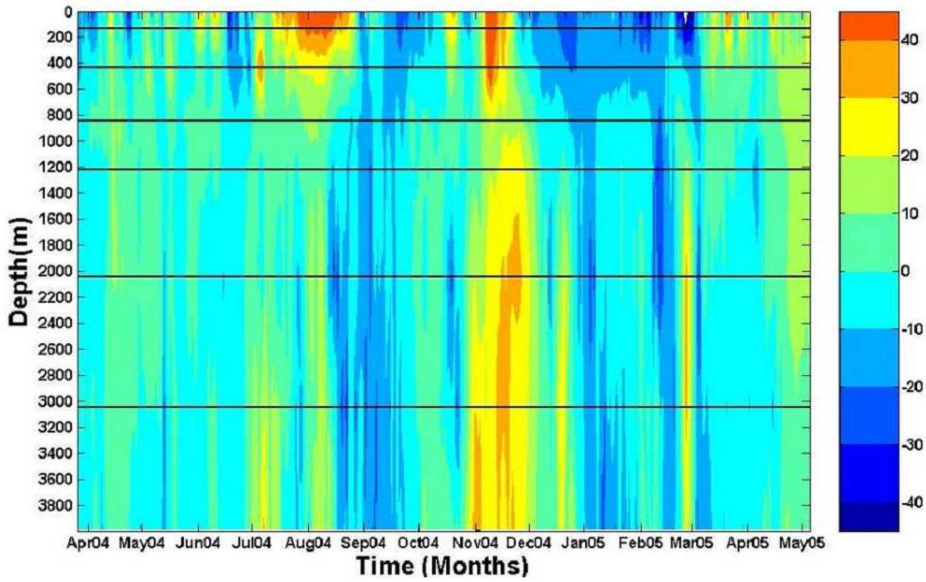

(b)

FIGURE 3.14: Vertical plot of meridional velocity anomalies from April 2004 to May 2005: (a) WB2; (b) WB3. Black lines show sampling depths of instruments available on respective moorings. In WB3, the large November event is clearly seen in the meridional velocity anomalies.

at WB2 and WB3 respectively) during the events. WB5 offshore (Fig.3.15(c)) does not show as much of the variability in the deep ocean temperature contours as seen inshore at WB3 (Fig.3.15(b)) or WB2 (Fig.3.15(a)).

We propose to continue to study the spatial-temporal variability of currents

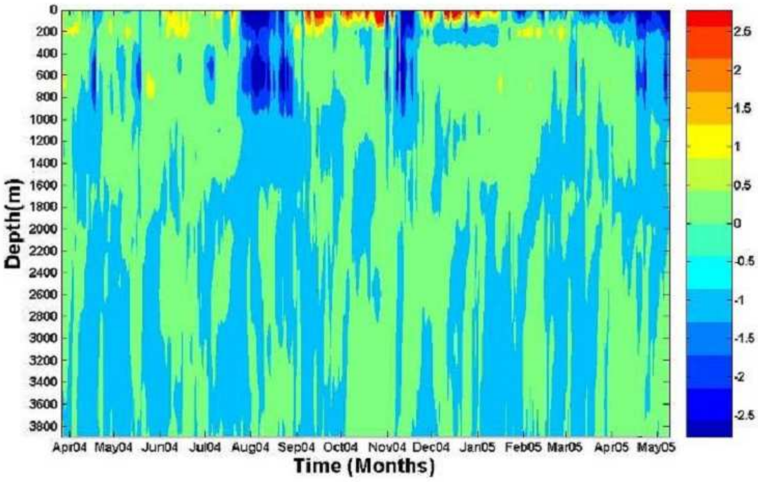

(a)

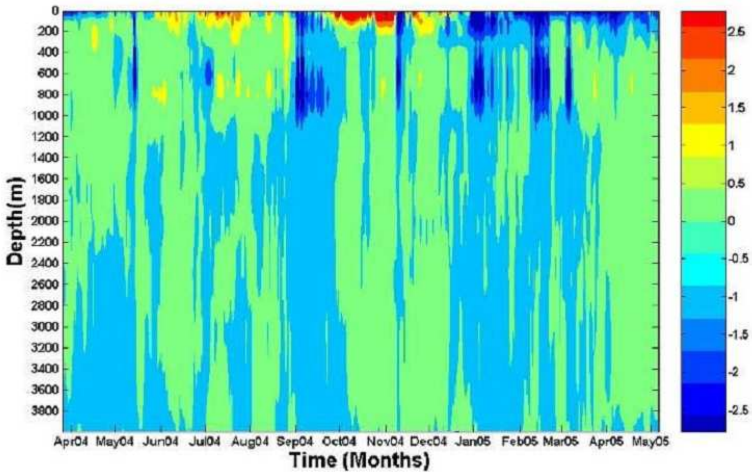

(b)

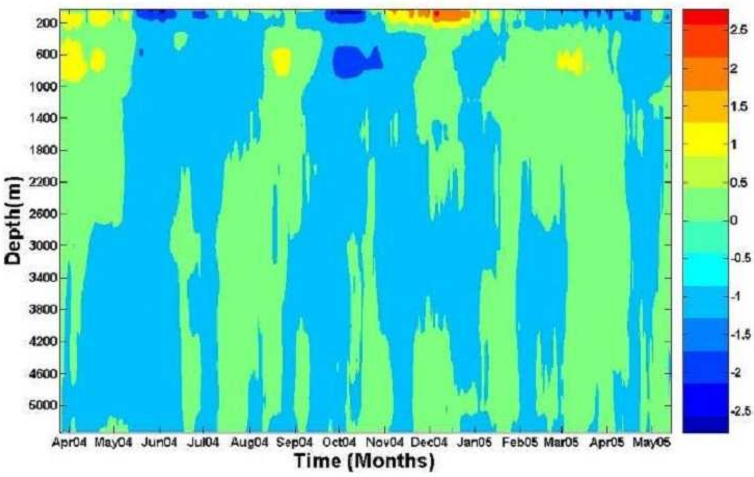

(c)

FIGURE 3.15: Vertical plot of temperature anomalies from April 2004 to May 2005: (a) WB2; (b) WB3; (c) WB5.

and temperature between moorings to include the historical datasets in the future. We determine if the historical datasets show variability in the vertical structure which can be useful for comparisons with SSHA. This would aid in knowing how representative the current datasets are. The results from historical ACCP-1B datasets (Fig.3.16), show sub-annual variability in the meridional velocity and temperature datasets (similar to present WB2 and WB3 results).

From the analyses of first year mooring deployment datasets from RAPID-MOC and MOCHA, we can study the temporal-spatial variability in the western boundary 26.5 °N. The vertical structure of meridional velocities and temperatures depict clearly a decoupled upper ocean Antilles Current (AC) and lower ocean Deep Western Boundary Current (DWBC) regime to a higher resolution than previously possible. From visualizations of the full water column, we can see the vertical structure of the sub-annual features that we see in satellite SSHA. In further chapters we will need to determine its relationship of the moorings observations to surface altimeter observations. However, to determine if the November 2004 event is a one-off event, further studies into historical datasets are important to determine its significance and how representative the mooring datasets are.

3.5.2 Bottom Pressures

In bottom pressure (BP) records of the collated 10 bottom pressure instruments Fig.3.17), we were surprised to see the rising and falling pattern of BP, unison in time within a 5 to 10 day period. The std of the 12-hourly zonal average pressure, for all the 10 BP records, is 0.015 dbar and std 0.0048 dbar. For this basin scale fluctuation in pressure across the Atlantic basin at 26.5 °N, we find that the rising and falling pattern of the BP is within a time period of about 5 to 10 day. It appears as if the entire Atlantic Ocean basin is 'filling' and 'draining' simultaneously cross basin and this can lead to a strong fluctuation signal in the zonally averaged BP record. Care needs to be taken so this signal is removed from the local bottom pressure fluctuations for future work examining compensation mechanisms in the Gulf Stream

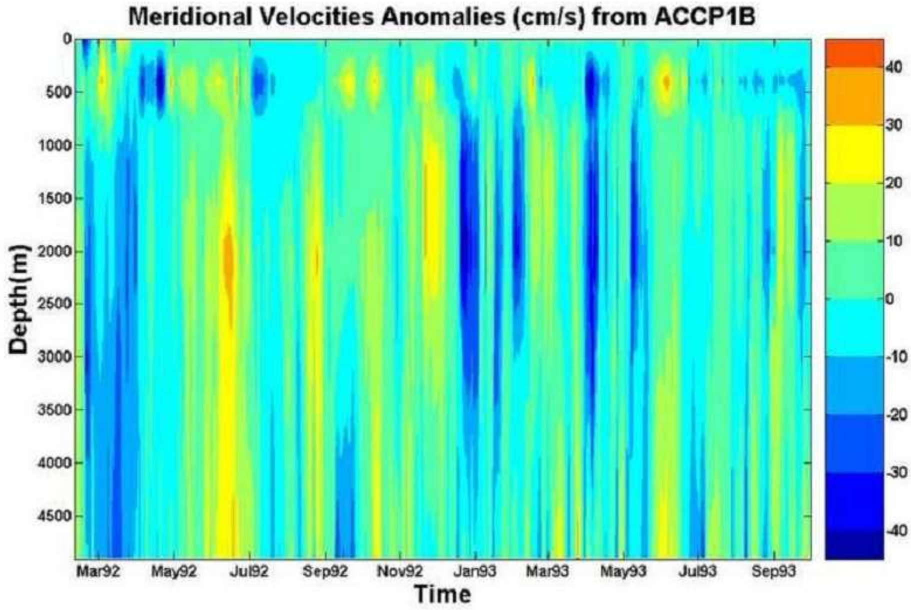

(a)

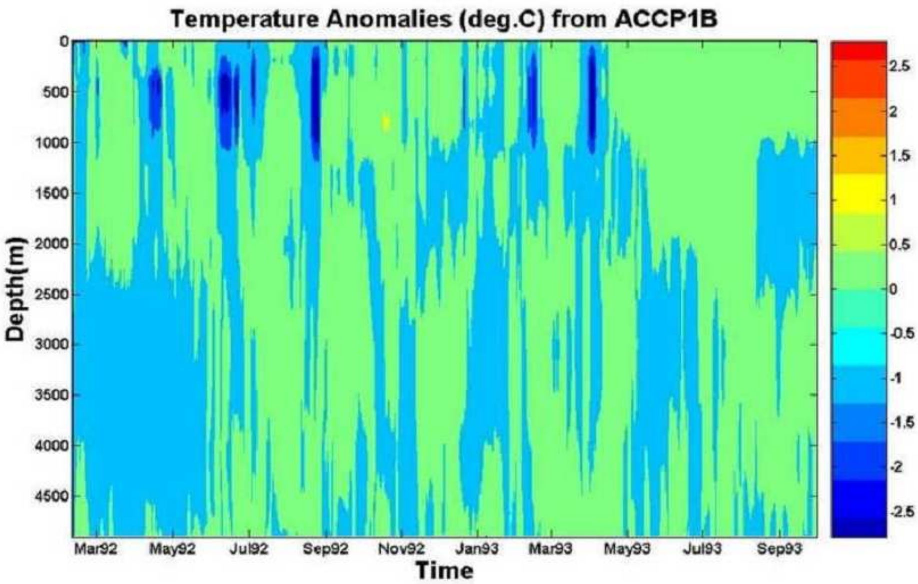

(b)

FIGURE 3.16: Vertical plot of historical ACCP1 anomalies from March 1992 to October 1993: (a) meridional velocity; (b) temperature.

and Ekman transport variability. We do this by removing the calculated zonal average BP (averaged of the 10 BP recorders) from individual records at each 12-hour time interval (see Table 3.5).

The cross basin zonal fluctuations should now be removed, and we find the resulting std BP signal to be 0.012 dbar down from 0.019 (a 60% reduction in variance). This

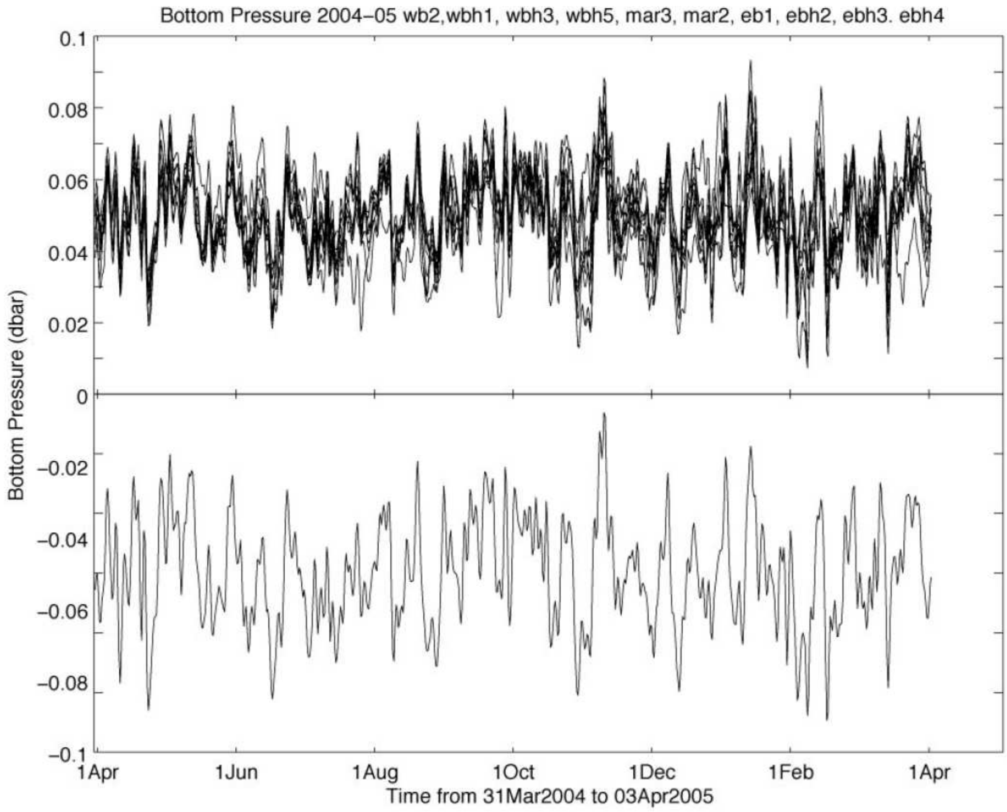

FIGURE 3.17: Bottom pressure time series at: (top) 10 sites across the Atlantic at 26.5 °N (with offset of 0.08dbar); (bottom) zonally averages BP daily (with offset -0.05 dbar).

TABLE 3.5: Variability in Bottom Pressure Datasets

Mooring	std dev (dbar)	Individual Zonal Average std dev (dbar)
wb2	0.0218	0.0118
wbh1	0.0226	0.0131
wb3	0.0210	0.0109
wb5	0.0261	0.0215
mar2	0.0173	0.0105
mar3	0.0168	0.0100
eb1	0.0189	0.0146
ebh2	0.0157	0.0094
ebh3	0.0165	0.0102
ebh4	0.0165	0.0095

step is important as a 0.02 dbar BP signal signifies a geostrophic transport signal of 15 Sv in a scenario of depth independent pressure fluctuations with over 5000 m depths, in geostrophic balance, and unmatched by the same BP signal on the opposite side of the basin. However, the high frequency BP fluctuations in the west and east basin are of similar amplitudes. Thus, the BP differences (proportional to the barotropic transport) are much smaller than their individual amplitudes. With this, the variance measured in the western BP is larger (but only slightly) than the eastern BP. It must be noted that future work especially dealing with analysis of local BP recorders, care must be taken in removing the spatially coherent variability in BP, in this case up to 60% of low frequency BP variability observed locally from individual BP records. When done for example in only the western boundary records, the spatially uniform variability could be larger than the dynamically important components (for example the baroclinic or Gulf Stream transport variability), and would be not related to local atmospheric pressure variability which has larger amplitudes and smaller spatial scales.

3.6 Summary

In this Chapter III we began with a review of low frequency variability especially Rossby Waves (RW), theory on its mechanisms, general methods in observations and its importance which serves as an outline of the assumptions and present research on propagating features. We then performed some preliminary spectral analysis on western boundary sea surface height altimeter dataset and moorings leading us to conclude that propagating features of high variability contribute significantly to temporal-spatial variability in the western boundary of the 26.5 °N section and propagating features including eddies must be accounted for. Besides that, it was curious that at the mooring furthest inshore at WB2 and WB3, the upper surface water and deeper water regime of the decoupled AC-DWBC show different periodicities from mooring dataset although the spectral analysis of sea surface heights were showing similar dominant periods. We continued by exploring the SSHA datasets and have found that many of the propagating features tracked from offshore and found the propagation speeds of about 6 cms^{-1} from WB5 to WB3 and close to 8 cms^{-1} from WB3 to WB2. This translates to an increase in travelling speeds by up to 22% over nearly 500 km. It is important to note that uncertainty in the speeds is due to uncertainty in the time lag for maximum correlation of $\pm$ 3.5 days. Also, at least 70% of the variability we see from offshore mooring positions have disappeared when approaching inshore. The max SSH std is found just offshore close to the western boundary but drops drastically westward inshore. It is not due to sampling errors and warrants further investigation in coming chapters. From the analyses of first year mooring deployment datasets from RAPID-MOC and MOCHA, we can study the temporal-spatial variability in the western boundary 26.5 °N. We see a decoupled AC-DWBC (upper ocean and deep ocean) regime in higher resolution than previously possible and we are able to pick out anomalies at various spatial-temporal scales. For the bottom pressure datasets, it was vital that analysis was done after appropriate filtering on a basin scale approach and so care must be taken so as not to remove the possible dynamically important components to the variability. The western boundary is a complicated region and one-off shipboard measurements need to take into account the presence of eddies besides Rossby wave propagation. Large events such as the possibly one-off November 2004 event, are important to determine the interaction of the circulation at the western boundary, the impact to the dynamics at the western boundary and ultimately the effect to its variability. Further study into historical datasets are important to determine how representative the Rapid mooring datasets are. Studying the vertical structure of flow from mooring datasets can also provide insight to understanding how these features interact at the complicated western boundary region.

Chapter 4

The Use of Vertical Projection of Data and Statistical Modes in Improving Assessments of Variability

4.1 4.1 Chapter Overview

The chapter begins with an introduction to vertical projection of data including theoretical and statistical modes, their derivations, assumptions and present theoretical papers. We then describe the vertical modal structure derived from the observations and the boundary conditions imposed. From these, we will be able to determine the extent of which statistical vertical modes compare to theoretical vertical modes of variability. This will lead to novel results alluding to the prospect of studying the vertical structure using statistical modes. We can also then determine the quantitative proportion of which propagating features contribute to the observed variability within the vertical structure.

The aims of the chapter are highlighted to simplify the research:

1. To determine if the vertical mode structure derived using theoretical and statistical methods are the same.

2. To determine if the relative contributions of higher modes (Mode 1 to Mode 3) to the variability at western boundary 26.5 °N are high.

4.2 4.2 Introduction

In describing and visualizing variability using large oceanographic datasets, various methods can be employed to reduce large time series into compressed smaller number of independent pieces of information on the variability. Emery and Thompson (1997) explains in much detail the widely used methods in which to analyse and present spatially distributed oceanic data to a level easily visualized. Here we briefly explore two common methods in wave analysis: (i) the theoretical normal modes, including the theory and derivations behind vertical normal modes (henceforth VNM); and (ii) the statistical empirical orthogonal functions (EOFs). Explanation and prediction of flow from principles of fluid dynamics are along patterns of motion, and so the associated necessary components (fields) such as pressure, temperature, salinity and density are dynamically linked to motion in the ocean. Thus the method explored here can be employed to all associated components as well.

4.3 4.3 Vertical Normal Mode (VNM)

Vertical normal modes are a subset of normal modes so firstly, we will understand the greater picture of normal modes. In general terms, normal modes are oscillations in which the fluid motion is in the same frequency and phase and so every change in a system is a superposition of normal modes. Bearing this in mind in the oceanographic context, we can separate variances in data into an ordered set of spatial and temporal statistical modes.

Using the normal modes involves the procedure of finding decomposition of solutions (e.g. separated vertical and horizontal components of fluid motion) based on the eigenvectors of a set of linearized dynamical equations as well as to determine the different responses (forced or freely propagating). This method is commonly used for large-scale motions, which yields the solution to be expressed as a sum of normal mode solutions for which each has a fixed vertical structure and behaves in time and in horizontal dimension similarly to homogenous fluids with a free surface (Gill, 1982).

Assumptions in the underlying physics and boundary conditions of the oceanic system are made to solve the eigenvalue problem and approximate the complete solution to the original differential equations. Currently, this technique is applied in ocean models, either continuous or discretely stratified. Results from the former are an infinite set of normal modes and the latter a finite number of modes.

A brief introduction to vertical normal mode (VNM) theory and its derivations can be found in the following parts of this chapter. Basically, working with the mean density profiles, we have obtained the corresponding Brunt-Vaisala frequency. This is then applied to Sturm-Liouville equation to calculate the eigenvalues (which describe the dynamical properties of the system) and the eigenvectors (define the vector coordinates) for the derived the theoretical modes. This is subject to the end-point boundary conditions of the seafloor and the upper free surface. The normal modes are then normalized and fitted to the data in a least squares sense. The maximum possible number of baroclinic modes is the number of depths minus one. In this case we have binned the dataset at discrete 100 m intervals before analysis and could have as many as 45 vertical modes. However, our interests are on the first few leading modes.

4.3.1 4.3.1 Theory and Derivations

The theory of vertical normal modes (VNM) separates out the vertical structure from the horizontal structure within the equations of motion. In the context of analysis and the visualization of the spatial distribution of variables, this enables the vertical structure of different variables in the ocean to be decomposed. The VNM theory can be found in many textbooks such as Kundu (1990); Gill (1982); LeBlond and Mysak (1979). In this review, we will only outline the main derivations and results of the VNM under assumptions outlined, i.e. main calculation of VNM eigenfunctions (arbitrary constants) for a stratified hydrostatic fluid with specified top and bottom boundary conditions. Then, we compare these derived VNM with corresponding RW derivations. In this review, we are assuming the linear flat bottom VNM theory (continuous case). This will not include the possible impact of the topography to local dispersion relation or wave propagation (or change to predicted local velocities), and so any change in vertical normal mode be contributed to modification of background potential vorticity by mean flow.

Assumptions:-

1. Continuous stratification in an incompressible (inviscid) fluid in hydrostatic balance
2. Linear flat bottom case (specified top and bottom boundary conditions)
3. Assumptions of linearity i.e. the 3 velocity components (horizontal u and v, and vertical w) are assumed to have small Rossby number, $\frac{V}{fL} << 1$
4. Both pressure and density are considered as uniform background fields, with small perturbations

$$p{=}p_0(z) + p'(x,\ y,\ z,\ t)$$
$$\rho{=}\rho_0(z) + \rho'(x,\ y,\ z,\ t)$$

5. Variables of pressure, density and the components of velocity can be separated into vertical and horizontal components.

$$e.g. \quad V(x,\ y,\ z,\ t) = V(z)\ v(x,\ y,\ t)$$

As in LeBlond and Mysak (1979), we start with describing small amplitude motions about the hydrostatic equilibrium state $p_0(z)$, $\rho_0(z)$, centered in mid-latitude ocean basins (neglecting the term $\widetilde{f}w$ in the momentum equations for u and assuming that the horizontal length scale L is large compared to depth H). Assuming the hydrostatic approximations yield the linearized hydrostatic β-plane equations governing the dynamics, linear for horizontal motion (long waves), and including rotation (f). We use $f = f_0 + \beta y$, and have p' and ρ' denoting the perturbation pressure and density fields.

Dynamics (Primitive)

$$u_t - fv = -\frac{1}{\rho_0}p'_x \tag{4.1}$$

$$v_t + fu = -\frac{1}{\rho_0}p'_y \tag{4.2}$$

Assuming $\frac{D}{Dt}W$ is small and $\omega^2 << N^2$, where ω is the frequency thus making the hydrostatic approximations valid, we have also neglected, in the linear approximation the vertical acceleration terms $\rho_0 w_t$ and $\rho_0 \widetilde{f} u$, and so the hydrostatic relation is the vertical primitive equation, both for the background and perturbation fields separately.

Hydrostatic Balance

$$\frac{\partial p_0}{\partial z} = -g\rho_0$$

$$p'_z = -g\rho' \tag{4.3}$$

Continuity is assumed (in incompressible fluid)

$$u_x + v_y + w_z = 0 \tag{4.4}$$

Also, the density conservation equations is linearised about the background vertical density gradient (when written using the form of equation 4.1) are as written below.

Density Conservation

$$\frac{D\rho}{Dt} = \frac{\partial \rho'}{\partial t} + w\frac{\partial \rho_0}{\partial z} = 0 \tag{4.5}$$

Assuming quasi - geostrophy with $\omega << f$, gives 4.6 and 4.7, where the velocity is proportional to the horizontal pressure gradient, the primitive equations are still linear for horizontal motion. And from 4.3 and 4.5 we get 4.8, where $\overline{\rho}_0$ is a reference density using the Boussinesq approximation so that ρ_0(z) is replaced by a constant density except in the buoyancy term:

$$u = -\frac{1}{\overline{\rho}_0 f}\frac{\partial p'}{\partial y} \tag{4.6}$$

$$v = \frac{1}{\overline{\rho}_0 f}\frac{\partial p'}{\partial x} \tag{4.7}$$

$$-w = \frac{\partial \rho'}{\partial t} / \frac{\partial \rho_0}{\partial z} \quad orw = p'_{zt}/g\frac{\partial \rho_0}{\partial z} \tag{4.8}$$

Considering vorticity in a rotating frame, we can form the vorticity gradient equation 4.9 below by taking $\partial/\partial x$ of 4.2 and $\partial/\partial y$ of 4.1

Vorticity

$$\frac{\partial}{\partial t}(v_x - u_y) + f(u_x + v_y) + \beta v = 0 \tag{4.9}$$

From the continuity equation 4.4 into the vorticity 4.9 we get the following:

$$-w_z = u_x + v_y$$

$$\frac{\partial}{\partial t}(v_x - u_y) - f(w_z) + \beta v = 0 \tag{4.10}$$

Combining the primitive equations (4.6, 4.7) and 4.8 into the new vorticity equations (4.10) gives the new form of the quasi-geostrophic equation.

$$\tfrac{1}{\bar{\rho}_0 f}(p'_{xx} + p'_{yy})_t - f\tfrac{\partial}{\partial z}\tfrac{p'_{zt}}{g\frac{\partial \rho_0}{\partial z}} + \beta\tfrac{1}{\bar{\rho}_0 f}(p'_x) = 0$$

$$(p'_{xx} + p'_{yy})_t + f^2\frac{\partial}{\partial z}\frac{p'_{zt}}{N^2} + \beta(p'_x) = 0 \tag{4.11}$$

where N is the Brunt Vaisala frequency (which is a measure of the stratification of the fluid) and is given by $N^2 = -\frac{g}{\bar{\rho}_0}\frac{\partial \rho_0}{\partial z}$.

Some authors work with a streamfunction ψ, which is proportional to the pressure anomaly, hence the horizontal velocity components, the density anomaly and the vertical velocity component can be expressed in the terms of ψ. E.g. $\psi_x = v$ and $\psi_y = -u$, where $\psi = p'/\bar{\rho}_0 f$ in our formulation. We now express each dependent variable in 4.11 in the terms of the ψ. Now, the full linearized governing equation of motions demonstrating the vorticity dynamics of a stratified fluid on the β-plane is:

$$\frac{\partial}{\partial t}(\frac{\partial^2\psi}{\partial x^2} + \frac{\partial^2\psi}{\partial y^2} + \frac{\partial}{\partial z}(\frac{\partial\psi}{S\partial z})) + \beta\frac{\partial\psi}{\partial x} = 0, \text{ with } S = \frac{f^2}{N^2} \tag{4.12}$$

At this point u, v, w and ρ' have been eliminated, but they can be found in the terms of P

$$u = -\frac{p'_y}{f\bar{\rho}_0},\ v = \frac{p'_x}{f\bar{\rho}_0},\ \rho' = -\frac{p'_z}{g} \text{ and } w = -\frac{p'_{zt}}{\bar{\rho}_0 N^2}$$

Now, assuming the waves are within a uniformly stratified incompressible rotating fluid (with uniform buoyancy frequency, i.e. N^2 = constant), and the motions are of small amplitude, with low frequencies, we can consider that the waves take the form

$$\psi_0 \ \ exp(ikx + ily + imz - i\omega t)$$

without loss of generality to derive the dispersion relation connecting the frequency, ω with the horizontal wavenumber, k and l, and the vertical wavenumber, m. Substituting into this form 4.12 we get 4.13, the dispersion equation which show that all planetary waves have westward phase velocity (negative ω implies westward propagation).

$$\omega(k^2 + l^2 + Sm^2) + \beta k = 0 \ \text{ or } \ \ \omega = -\frac{\beta k}{k^2 + l^2 + Sm^2} \tag{4.13}$$

From long waves $k^2 + l^2 << Sm^2$ so the long wave dispersion relation is

$$\frac{\omega}{k} = -\frac{\beta}{Sm^2}$$

The group velocity components in the horizontal x-, and y- directions and the vertical z- direction is obtained by differentiating equation 4.13 for long waves, where $k^2+l^2 <<$ Sm^2

$$c_{gx} \equiv \frac{\partial\omega}{\partial k} = -\frac{\beta}{Sm^2} \tag{4.14}$$

$$c_{gy} \equiv \frac{\partial \omega}{\partial l} = \frac{2\beta kl}{(Sm^2)^2} \tag{4.15}$$

$$c_{gz} \equiv \frac{\partial \omega}{\partial m} = \frac{2f^2\beta km}{N^2(m^4)} \tag{4.16}$$

4.3.2 4.3.2 VNM and Rossby Waves (RWs)

As we know, the purpose of vertical normal mode analysis is to separate out the vertical structure from the horizontal structure of the solution. Thus a solution is sought of the form:

$$\psi = Re \quad e^{i(kx+ly-\omega t)}\psi_n(z)$$

where $\psi_n(z)$ is the vertical structure function to be found, the subscript n anticipating the vertical mode numbers, or

$$p'(x, y, z, t) = P(z)p(x, y, t)$$

and $p(x, y, t)$ is the horizontal structure assumed to be wavelike $e^{i(kx+ly-\omega t)}$.

We now consider the separated boundary conditions as for Rossby waves in an oceanic case. For the complete eigenvalue problem, that is unbounded laterally but limited in its vertical scale i.e. vanishing vertical component of velocity at the upper free surface z=0 (the rigid lid condition), and at the flat bottom ocean z= 1 (no boundary fluxes driving the modes). The boundary conditions are

$$\frac{\partial^2 \psi}{\partial t \partial z} = 0 \quad \text{at} \quad z = 0, 1 \tag{4.17}$$

The vertical structure function, $\psi_n(z)$ must satisfy the following Sturm - Liouville equation:

$$\frac{1}{\rho_0}\frac{\partial}{\partial z S}\frac{\partial \psi_n}{\partial z} = -\lambda\psi_n \tag{4.18a}$$

As before $S = \frac{f^2}{N^2}$, and $N^2 = -\frac{g}{\rho_0}\frac{\partial \rho_0}{\partial z}$ is the Brunt-Vaisala frequency. The eigenvalue λ_n of the modes, is obtained from the separation constant c_n^2, i.e. $\lambda_n = \frac{1}{c_n^2}$, and from 4.13 is given by:

$$\lambda_n = Sm^2 = -(\tfrac{\beta k}{\omega} + k^2 + l^2)$$

$$m^2 = -(\frac{\beta k}{\omega} + k^2 + l^2)/S \tag{4.18b}$$

To check the vertical velocity, the boundary conditions in 4.19a and 4.19b for ψ_n (top and bottom of the ocean) are determined from 4.17.

$$\frac{\partial \psi_n}{\partial z} = 0, \text{at} \quad z = 0 \tag{4.19a}$$

$$\frac{\partial \psi_n}{\partial z} = 0, \text{at} \quad z = 1 \tag{4.19b}$$

As mentioned before, the separation constant c_n^2 reflects the phase speeds and is associated with the eigenvalue λ_n of the modes, i.e. $\lambda_n = \frac{1}{c_n^2}$. Determined from the boundary conditions, they are summarized by 4.20a and 4.20b (Gill, 1982).

$$\text{Barotropic mode, } n = 0, \quad c_0 = \sqrt{gH} \tag{4.20a}$$

$$\text{Baroclinic mode, } n = 1, 2, 3 ... \quad c_n \approx \frac{NH}{n\pi} \qquad \text{for constant N} \tag{4.20b}$$

With different suitable boundary equations in this oceanic case, 4.18a or 4.18b, and 4.19a or 4.19b are now eigenvalue problems for the eigenvalue λ_n which when solved, will give rise to the infinite number of vertical normal mode solutions since N^2 and S are always positive in the interval (0, 1).

The following shows how we can solve the eigenvalue problem (Pedlosky, 1987). The solutions of the different vertical mode wave speeds $\psi_n, n = 1, 2, 3$ correspond to the eigenvalue problem with different real, discrete eigenvalue of $\lambda_n, n = 1, 2, 3$. After integration by parts 4.21, it is also seen that all the non-zero λ_n are positive.

$$\lambda_n = \frac{\int_0^1 \frac{\rho_0}{S} \left| \frac{\partial \psi_n}{\partial z} \right|^2 dz}{\int_0^1 \rho_0 |\psi_n|^2 dz} \tag{4.21}$$

And $\lambda = 0$ is an eigenvalue for arbitrary $\rho_0(z)$ and $S(z)$ since 4.18a or 4.18b, and 4.19a or 4.19b are satisfied by:

$$\lambda = 0, \quad \psi_n(z) = 1 \tag{4.22}$$

By convention, the first is called the barotropic mode, and the subsequent are the baroclinic modes. The barotropic ψ field is independent of depth and its horizontal velocities are also depth independent. Its vertical velocity and density perturbations are identically zero. For this $\lambda = 0$ mode, 4.22 applies and it is identical to the Rossby wave frequency of a homogeneous fluid. This barotropic mode in a stratified fluid and has the dispersion relation below, is possible regardless of the detailed structure of $\rho_0(z)$ and $S(z)$.

$$\omega = \omega_0 = -\frac{\beta k}{k^2 + l^2} \tag{4.23}$$

When $\lambda \neq 0$, the integral of 4.18a from $z = 0$ to $z = 1$, bearing in mind the boundary conditions at the end points 4.17, the vertically integrated density perturbation is 0 :

$$\int_0^1 \rho'(z) dz = 0, \quad \lambda \neq 0 \tag{4.24}$$

and all solutions with $\lambda_n \neq 0$, have zero vertically integrated horizontal mass flux

$$\int_0^1 \rho_0 u dz = \int_0^1 \rho_0 v dz = 0, \quad for \quad \lambda_n \neq 0 \tag{4.25}$$

These modes are the baroclinic modes, and deform the density surfaces, have non-zero vertical velocity and their presence depends on the basic stratification. For example, with constant $\rho_0 = 1$ and S, we get 4.26

$\frac{1}{S}\frac{\partial^2 \psi_n}{\partial z^2} = -\lambda_n \psi_n$ or

$$\frac{\partial^2 \psi_n}{\partial z^2} = -\lambda_n S \psi_n \tag{4.26}$$

with the solution satisfying the boundary conditions 4.19a being

$$\psi_n = \cos(\lambda_n S)^{1/2} z \tag{4.27}$$

and the eigenvalue relation 4.27 from the boundary conditions 4.19b

$$\sin(\lambda_n S)^{1/2} = 0 \tag{4.28a}$$

or

$$\lambda = \lambda_n = \frac{n^2 \pi^2}{S}, \quad n = 1, 2, 3... \tag{4.28b}$$

The $n = 0$ mode is the barotropic mode as discussed before. For the $n > 0$ the solutions are the set

$$\psi_n(z) = \cos n\pi z, \quad n = 1, 2, 3... \tag{4.29}$$

Each corresponding to the eigenvalue λ_n as given in 4.28b. This demonstrates the following general feature of the eigenvalue problem:

if the λ_n are arranged to form an increasing sequence

$$\lambda_0 = 0 < \lambda_1 < \lambda_2 < \lambda_3 < ... < \lambda_{n-1} < \lambda_n < \lambda_{n+1} \tag{4.30}$$

then for any $n > 0$, ψ_n has one more zero in the interval (0, 1) than ψ_{n-1}. The higher modes are more 'wiggly' in the depth. If $S(z)$ is a more complicated function of z, the numerical values of λ_n will be altered as well as the structure of the baroclinic modes ψ_n but their general character will remain unaltered.

For each λ_n calculated, there exists a corresponding Rossby-wave frequency

$$\omega_n = -\frac{\beta k}{k^2 + l^2 + \lambda_n}, \quad n = 0, 1, 2, ... \tag{4.31}$$

When comparing the dispersion relationship for a uniformly stratified fluid, with the dispersion relation of the Rossby wave modes (whether barotropic or baroclinic), they are found to be identical with:

$$\lambda_n = Sm^2 \tag{4.32}$$

In particular, all the properties of horizontal energy propagation, reflection and dispersion derived for the homogenous model can be directly carried over to the properties of each mode in the stratified fluid with the identification of Sm^2 with λ_n.

For example, the group velocity in the x-direction for the n-th mode is simply 4.14 with the factor Sm^2 derived to be equivalent to λ_n (Pedlosky, 1987).

$$c_{gx} = \frac{\beta(k^2 - (l^2 + \lambda_n))}{(k^2 + l^2 + \lambda_n)^2} \tag{4.33}$$

Since the λ_n form an increasing sequence, the higher baroclinic modes will tend to favor energy propagation to the west. On the other hand, the group velocity is a decreasing function of λ_n, so that the higher baroclinic modes will propagate their energy more slowly than the barotropic mode or the lower baroclinic modes. Sometimes the eigenvalue λ_n is written in terms of the quantity h_n, called the equivalent depth. It is similarly defined by an eigenvalue problem and is not merely given by the physical vertical scales, as by the relationship 4.34 below

$$\lambda_n = \frac{f^2}{gh_n} \tag{4.34}$$

And so, the propagation characteristics of the n-th Rossby wave mode in a stratified fluid are given entirely by the characteristics of the Rossby wave in a homogeneous layer whose depth is the equivalent depth h_n. For a barotropic mode the equivalent depth is infinite and for the water column of constant N,

$$h_n^2 = \frac{N^2 D^2}{gn^2\pi^2} \tag{4.35}$$

where D is the depth of water.

Figure 4.1 shows the structure of these modes in the case of a constant ocean depth, where the baroclinic modes are sinusoids. Note that the barotropic pressure mode is almost depth independent, hence the definitions used previously, (i.e. barotropic 'depth-independent' or baroclinic 'depth-varying'). If the rigid lid boundary condition is used, the barotropic mode would be completely depth independent. The small depth variation comes when a free surface boundary condition is used.

All variables can be decomposed into these modes, viz

$$\begin{aligned}
p'(x,y,z,t) &= \textstyle\sum_n P_n(z)p_n(x,y,t) \\
w(x,y,z,t) &= \textstyle\sum_n W_n(z)w_n(x,y,t) \\
u(x,y,z,t) &= \textstyle\sum_n -\frac{il}{\bar{\rho}_0 f}P_n(z)u_n(x,y,t) \\
v(x,y,z,t) &= \textstyle\sum_n \frac{ik}{\bar{\rho}_0 f}P_n(z)v_n(x,y,t)
\end{aligned}$$

where $W_n(z) = \frac{i\omega}{\bar{\rho}_0 N^2}\frac{\partial P_n(z)}{\partial z}$

4.4 4.4 Empirical Orthogonal Functions (EOF) Modes

The EOF method involves Principal Component Analysis (PCA) to summarise the variability (reduction of data) by finding patterns in the data that explain the maximum variance. The linear combination of the spatial orthogonal 'modes', or predictors in time function, essentially accounts for the combined variance in all observations in the time series grid (horizontal and depth cross sections). Caution has to be mentioned in the use of EOF modes as it is a statistical tool, by which the datasets are compressed through partitioning of variance. And so, the patterns may be linked to physical dynamics or physical modes (e.g. Quasi-geostrophic modes) but they do not necessarily have a direct physical or mathematical relationship.

4.4.1 4.4.1 Theory and Derivations

Here Empirical Orthogonal Functions (EOFs) also known as Principal Component Analysis (PCA) are used to describe the spatial temporal variability of data in terms of orthogonal functions or statistical modes of variability (Horel, 1984). EOFs represent a statistical method of analysis to enable the transformation of the dataset (done by performing an eigenvalue analysis of the covariance matrix of the dataset e.g. Variance-covariance matrix to determine maximum variance by linear combinations) to yield eigenvectors which are the 'spatial patterns', or principal component loading patterns, which can then be mapped to easily view spatial patterns (eigenvectors) of variability. The first EOF explains the most variance in the dataset. The expansion coefficient (ECs) on the other hand, are the component time series for each principal components (also commonly known as Principal Components, PCs) which represents the 'temporal patterns' describing how the spatial structure evolves in time.

To prepare the dataset before analysis (as seen in Fig.4.2), the original data matrix (X) of $M * N$ matrix that is space*time (collection of row time column space vectors)

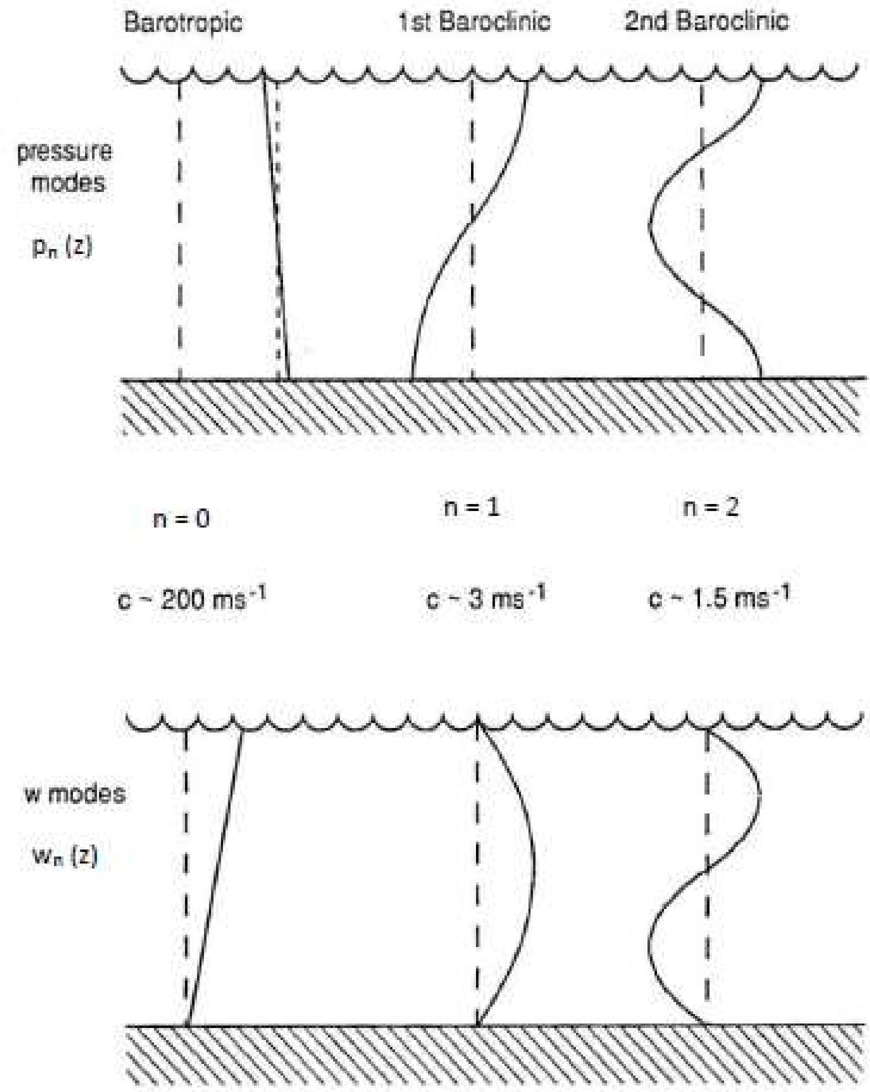

FIGURE 4.1: Vertical normal modes for pressure,$p_n(z)$, and vertical velocity, $w_n(z)$, in a constant N^2 ocean with free surface boundary conditions. Adapted from Woodgate (1994).

is ensured to have: (1) same start/end time with equal lengths (N); (2) de-mean and de-trended; (3) each now normalized by its std

The next step involves the projection of the dataset onto a set of orthogonal functions and to replace the original dataset with a set of projection coefficients of the basis vector. Here we have chosen the computationally efficient Singular Value Decomposition (SVD) method which derives all the components of EOF analysis (eigenvectors, eigenvalues and time-varying amplitudes) without the computation of the covariance matrix. The data matrix, X, is 'broken' into 3 matrices, i.e.

$$
X = \begin{array}{c|ccccc|}
 & t1 & t2 & t3 & t4 \ldots\ldots & tN \\
s1 & x\,11 & x\,21 & x\,31 & x\,41 \ldots\ldots & x\,N1 \\
s2 & x\,12 & x\,22 & x\,32 & x\,42 \ldots\ldots & x\,N2 \\
s3 & x\,13 & x\,23 & x\,33 & x\,43 \ldots\ldots & x\,N3 \\
 & . & . & . & . & . \\
 & . & . & . & . & . \\
 & . & . & . & . & . \\
sM & x\,1M & x\,2M & x\,3M & x\,4M \ldots\ldots & x\,NM
\end{array}
$$

FIGURE 4.2: Example of the original data matrix format (X) of $M * N$ matrix that is space*time (collection of row time/ column space vectors).

$$X = U * D * V$$

where U and V are orthonormal and D is diagonal. The EOFs, V, are the eigenvectors of the covariance matrix (the columns of the EOFs matrix), while U, is the time variability in each eigenvector of the covariance matrix, and D represents the variance explained by each EOF. The ECs are $U * D$. The EOFs and ECs visualized are reduced only to those explaining a significant percentage of the overall variance.

4.5 4.5 Results and Discussion

4.5.1 4.5.1 Meridional Velocity Modes

Early work compared these meridional velocity modes from normal mode analysis, seen in Figure 4.3(a), to EOF vertical modal structure are as seen in Figure 4.3(b), in this example at WB2 mooring site. This can provide a comparison on the two different descriptions of the vertical distribution of the time variable flow. Results (when normalized) indicate similar pattern of vertical modal structure for the 1st baroclinic mode $n = 1$ (Green) with the first EOF mode, by 0.9791. The correlation worsens with depth i.e. for the 2nd baroclinic mode $n = 2$ is 0.5381 (Red).

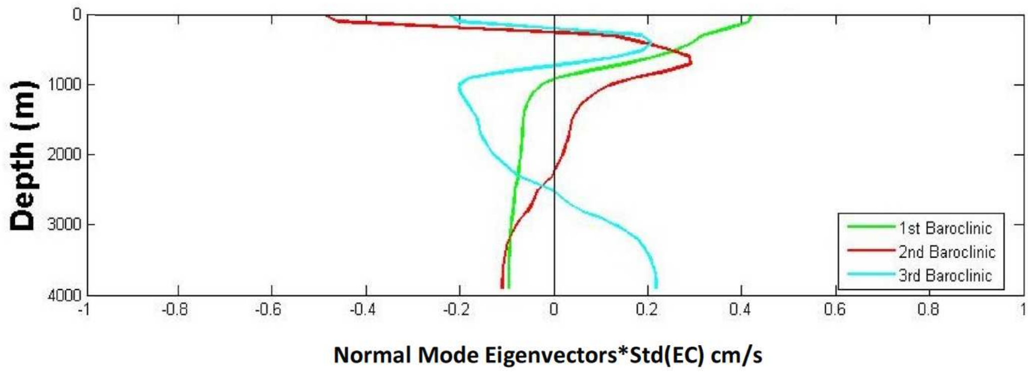

(a)

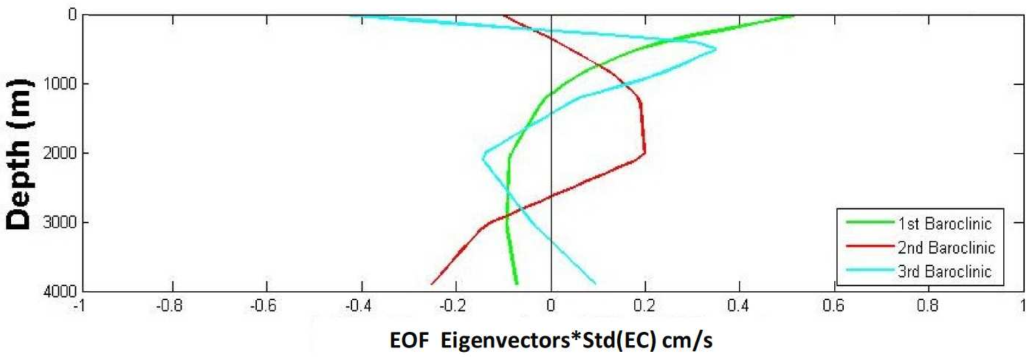

(b)

FIGURE 4.3: Comparison of vertical structure of modes from: (a) normal mode analysis (normalized); (b) EOFs (normalized). The barotropic mode has a magnitude of unity at all depths which are not plotted here in either figure. 1st baroclinic mode (Green); 2nd baroclinic mode (Red); 3rd baroclinic mode (cyan).

Using the vertical structures, we have visually captured the variability of the western boundary moorings. We now move to see if we can statistically characterize the events seen. Using the EOFs, we can determine what are the dominant statistical modes of variability at WB2 (Fig.4.4(a)) and WB3 (Fig.4.4(b)). For the purpose of this report, we concentrate on WB2 and WB3 meridional velocity datasets.

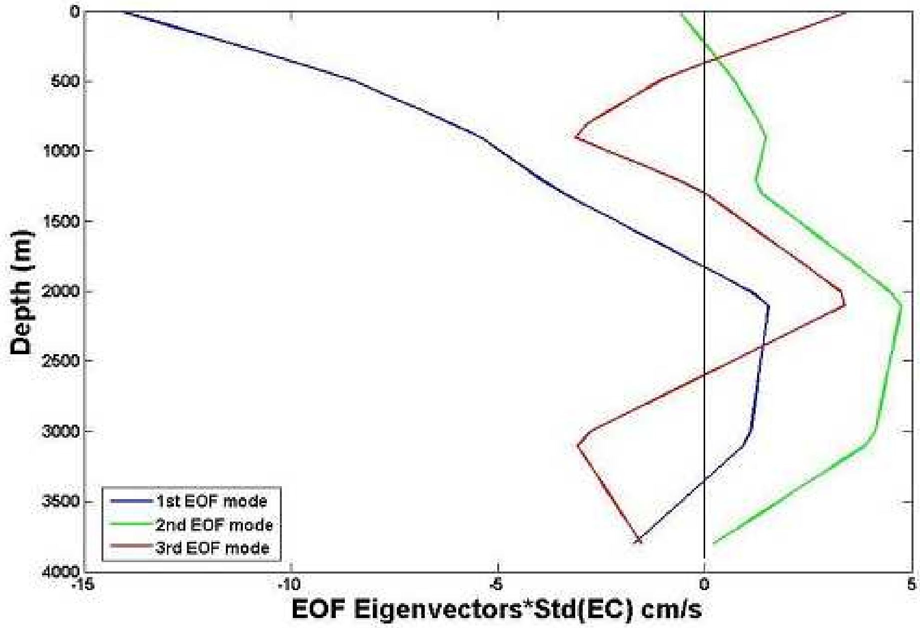

(a)

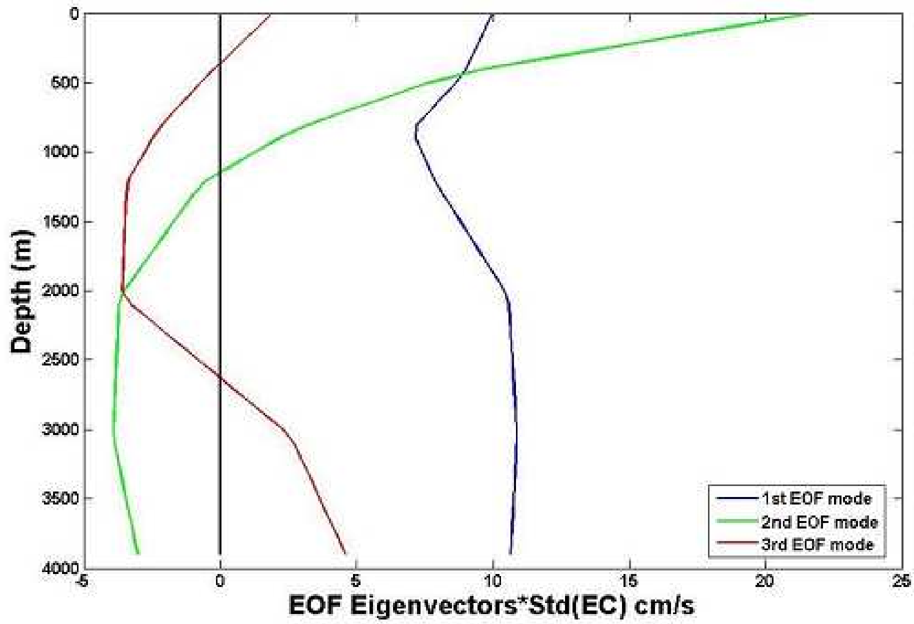

(b)

FIGURE 4.4: Meridional velocities EOF modal structure from April 2004 - May 2005: (a) WB2; (b) WB3. 1st EOF mode (Dark Blue) representing the barotropic mode which has a magnitude of unity at all depths; 2nd EOF mode (Green) representing the 1st baroclinic mode; 3rd EOF mode (Red) representing the 2nd baroclinic mode.

Firstly, results show the WB2 and WB3 EOF meridional velocity modal structure throughout the water columns. The EOF eigenvectors have been multiplied by the standard deviation of the ECs to give the structure a physical value in cms^{-1}. In general, the structure in WB2 is more complicated (does not map according to the structure expected from normal mode analysis) than WB3, probably due to the shielding and recirculation in the deep water below 1500m depths. The modal structure in WB3 is similar to the expected structure (e.g. first to following modes with zero to two zero crossings). However, much caution has to be placed in the effort to understand the EOF modal structure results. EOFs work as an efficient statistical tool whereby datasets are compressed through partitioning of variance which results in the EOFs modes not necessarily corresponding to true dynamical modes of physical behaviour. The discrepancy seen between the statistical EOF modes and the theoretical modes is because a single process can be spread over more than one EOF mode and likewise, more than one physical process can be contributing to the variance contained in a one single EOF mode.

Table 4.1 summarizes the contributions on the first three (3) EOF modes to the variances of individual moorings. For WB2, Fig.4.4(a), the first mode accounts for 51% of the variance in the dataset, with especially strong influence at the upper ocean, close to 15 cms^{-1} (positive or negative signs are arbitrary). The second mode on the other hand accounts for much of the variance in the lower ocean, close to 5 cms^{-1}. For WB3 4.4(b), the modes show a very different structure through depths. The first mode accounts for higher variance in the dataset (70%) compared to WB2, with almost equal magnitude at all depths (around 10 cms^{-1}) which is expected as it corresponds to the depth independent barotropic mode. However, unlike in WB2, much of the variance in the lower ocean is dominated by the first mode, whilst the upper ocean is dominated by the second mode (over 20 cms^{-1}).

Table 4.1: First three EOF modes and the % variances explained at individual moorings WB2 and WB3.

Mooring	1st EOF Mode	2nd EOF Mode	3rd EOF Mode	Total
WB2	51%	23%	12%	86%
WB3 (BJB)	70%	21%	6%	97%

Fig.4.5 shows the corresponding ECs time series (below) for the meridional velocity anomalies vertical profile time series (top) at (a) WB2 and (b)WB3 respectively. We can use the relative amplitudes of the ECs (EOF principal components) to reflect the dominant modes for any given event in time. From visual inspection, the high relative amplitudes of the ECs clearly coincide with the major sub-annual events. When studying the statistics of the events individually (e.g. decomposition of only the black boxed November event), the event has a very dominant second mode as the

leading mode of variability (61%), followed by the 1st mode (21%) and the third mode (15%).

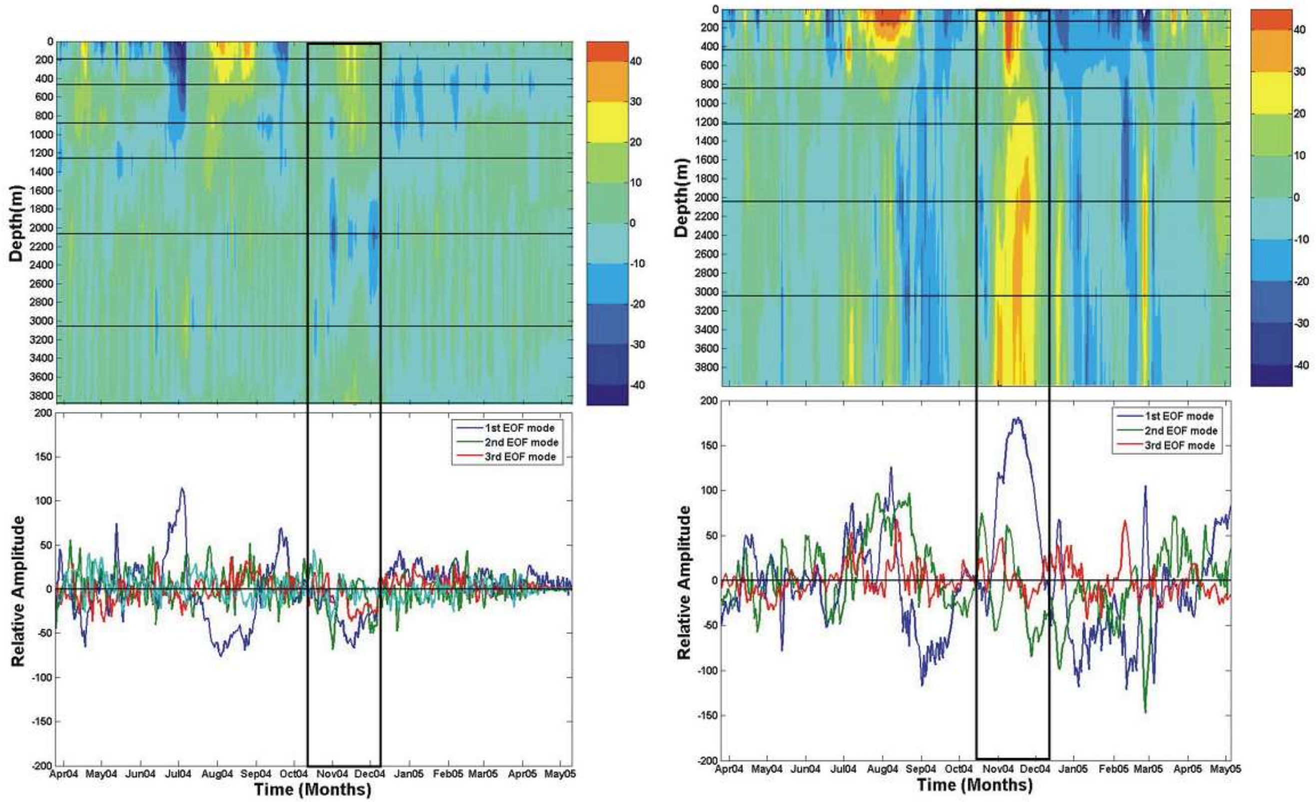

(a) (b)

FIGURE 4.5: Meridional velocities anomalies (Top) & relative amplitudes of the ECs (Bottom) from April 2004 to May 2005: (a) WB2; (b) WB3. 1st EOF mode (Dark Blue) representing the barotropic mode; 2nd EOF mode (Green) representing the 1st baroclinic mode; 3rd EOF mode (Red) representing the 2nd baroclinic mode. Black box highlights the November 2004 event.

4.5.2 4.5.2 Temperature Modes

Fig.4.6 are examples of the EOF temperature modal structure throughout the water column from WB2, WB3 and WB5 respectively. The temperature dataset has not been normalised. This can be done by using either: (i) the Brunt-Vaisala frequency profile; or (ii) standard deviation of the temperature at each depth sampled. Fig.4.7 shows the corresponding ECs time series (below) for the temperature anomalies time series (top) at WB2, WB3 and WB5 respectively. However, even with normalization of the temperature, interpretation of the temperature modal results was complicated and advised (P. Killworth, *Personal Communication*) to be left out in pursue of other dataset analyses.

4.5.3 4.5.3 Dynamic Height Modes with Bottom Pressure

We continue by creating a dataset of local daily bottom pressure anomalies (BPA) added to the dynamic height anomalies (DHA) at each of the moorings sites. The datasets are effectively time series of geostrophic pressure profiles. The estimated EOFs for the vertical structure can be applied as before, to obtain the vertical structure of the geostrophic pressure (equivalent to a profile of northward transport per unit depth, obtained by dividing the Coriolis parameter, f from geostrophic pressure. Fig.4.8, 4.9 and 4.10 are examples of the EOF modal structure throughout the water column from WB2, WB3 and WB5 respectively.

At WB2, Figure 4.8, the first 3 modes account for 92.7% of the variances. The first mode accounts for 56.0% of the variance in the dataset, displaying especially strong influence at the surface (surface intensified), exhibiting the same sign from surface to bottom modulating from 1000 - 4000 dbar possibly reflecting the 2-lobed structure of the DWBC. The second mode accounts for 22.5% of the variance, looks similar to the classical first baroclinic mode and its surface pressure will have opposite signs to the bottom pressure. The third mode then looks like the classical second baroclinic mode and accounts for 14.2% of the variance.

For WB3 (Fig.4.9), the modes show a very different structure through depths although the first 3 modes account for much more of the variances (95.9%). The first mode accounts for higher variance in the dataset (71.1%) compared to WB2, However, unlike in WB2, it has the same sign from surface to bottom and exhibits a surface intensified structure in the shallow flows above 1000 dbar. At depths below 1000 dbar, the structure is also relatively depth independent and might be termed the coupled barotropic-baroclinic mode. The second mode accounts for 17.9% of the variance, with features similar to the classic first baroclinic mode and the surface pressure will have opposite signs to the bottom pressure. The third mode again looks like the classical second baroclinic mode and accounts for 6.9% of the variance.

Looking at WB5 (Fig.4.10), the vertical modal structure is similar to WB2 and WB3 except the first 3 modes account for 99.0% of the variances. The first mode accounts for higher variance in the dataset (60.7%) compared to WB2. However, unlike in WB2, but much more like WB3 and the othe moorings offshore as well as at the Eastern Boundary EB1, it has the same sign from surface to bottom and exhibits a surface intensified structure in the shallow flows above 1000 dbar. The second mode accounts for 31.0% of the variance, with features similar to the classic first baroclinic mode displayed by WB3 and EB1. The third mode again looks like the classical second baroclinic mode displayed by WB3 and EB1 and accounts for 7.3% of the variance.

We consider the same analysis also at Eastern Boundary mooring EB1 (Fig.4.11), where we find the the vertical modal structure is similar to WB3 and WB5 except the first 3 modes account for 99.4% of the variances. The first mode accounts for highest variance in the dataset (60.6%) as expected however, it is similar to WB3 and WB5 further offshore at the Western Boundary. It has the same sign from surface to bottom and exhibits a surface intensified structure in the shallow flows above 1000 dbar. The second mode accounts for 37.0% of the variance, with features similar to the classic first baroclinic mode displayed by WB3 and WB5. The third mode again looks like the classical second baroclinic mode displayed by WB3 and WB5 and accounts for only 1.8% of the variance. These results are collated in Table 4.2 to explain the first three EOF modes and the % variances explained at individual moorings WB2, WB3, WB5 and EB1.

Table 4.2: First three EOF modes and the % variances explained at individual moorings WB2, WB3, WB5 and EB1.

Mooring	1st EOF Mode	2nd EOF Mode	3rd EOF Mode	Total
WB2	56%	22.5%	14.2%	92.7%
WB3	71.1%	17.9%	6.9%	95.9%
WB5	60.7%	31.0%	7.3%	99.0%
EB1	60.6%	37.0%	1.8%	99.4%

Correlations between surface dynamic height (DH) and bottom pressure (BP) observations are relatively small as seen in Table 4.3. The case of the vertical modes can help explain these low correlations: in the first mode, with about 60% of the variance has a positive correlation to surface dynamic height and pressure but the second mode contributes a negative correlation but with only 25% of variances. Overall, this partially diminishes the first mode correlations. In addition from looking at the individual time series, the fluctuations depicted by the bottom pressure fluctuations are smaller than the dynamic height fluctuations. The coupled barotropic - baroclinic mode WB3, WB5 and EB1 showing depth independent structure below 1000 dbar and instensified surface structure is what some e.g. Chelton et al. (2007) would call an eddy-like structure and the first baroclinic mode would be referred to as a baroclinic Rossby Wave. The coupled barotropic - baroclinic mode dominates roughly 2 to 1 but not enough that there is a consistent correlation between DH and BP. There is also no reason to suspect there would be a correlation between DH and BP as the DH calculations for the RAPID array (as outlined in Sub-section 2.5.3) are the geostrophic pressure profiles integrated from a pre-determined reference level to the surface.

TABLE 4.3: Correlation between surface dynamic height (DH) and bottom pressure (BP) observations at Western boundary mooring sites.

Mooring	Correlations
WB2	0.36
WB3	0.09
WB5	-0.13
EB1	-0.38

4.6 4.6 Summary

In summary, the purpose of this chapter was to introduce vertical projection of data including theoretical and statistical modes, their derivations, assumptions and present theoretical papers. We then explore the vertical modal structure derived from the observations and the boundary conditions imposed. We found the extent of which statistical vertical modes compare to theoretical vertical modes of variability to be high especially for velocity and dynamic height modes further offshore. By decomposing the dataset taking into account the associated physics and boundary conditions, there is great prospect of using statistical vertical normal mode analysis of *in-situ* mooring datasets to predict the vertical structure. The relative contributions of higher modes (mode 1 to mode 3) to the variability at western boundary 26.5 °N are high. For example in statistical modes created by combination of the local daily bottom pressure anomalies (BPA) to the dynamic height anomalies (DHA) at each of the moorings sites (effectively time series of geostrophic pressure profiles) we find that between 92 and 99 % of variance can be explained within the first three modes. The same goes for the statistical modes from meridional velocities which explain between 82 and 97 % of the variance. In the case of the the meridional velocity modes, the EOFs can be given a physical value in cm/s and directly correspond the anomalies in the time series to the relative amplitudes of the ECs (EOF principal components) to reflect the dominant modes and their physical contribution at any one time. By isolating the details we find different barotropic and baroclinic modes or even the coupled barotropic-baroclinic mode as seen in WB3, WB5 and EB1. We show that surface dynamic height and bottom pressure datasets are not correlated. In further chapters, we attempt to compare the similarities of *in-situ* data (such as from dynamic height) to be compared with sea surface height anomalies (SSHA) as to determine the possibility of future modal comparisons between the surface and sub-surface datasets.

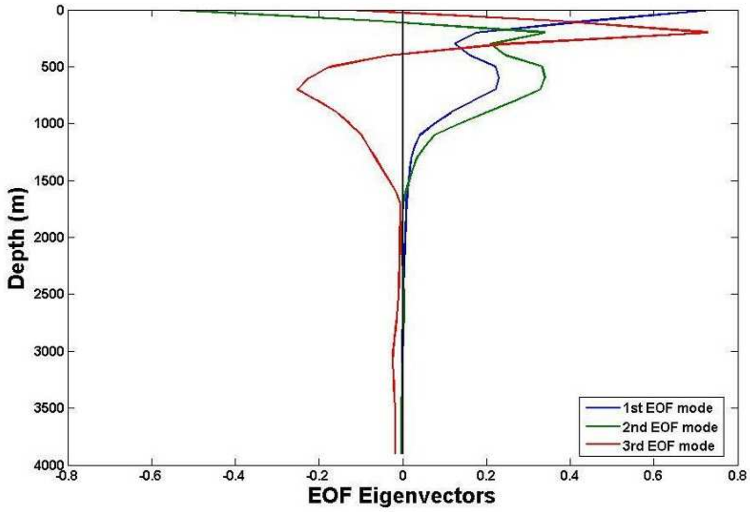

(a)

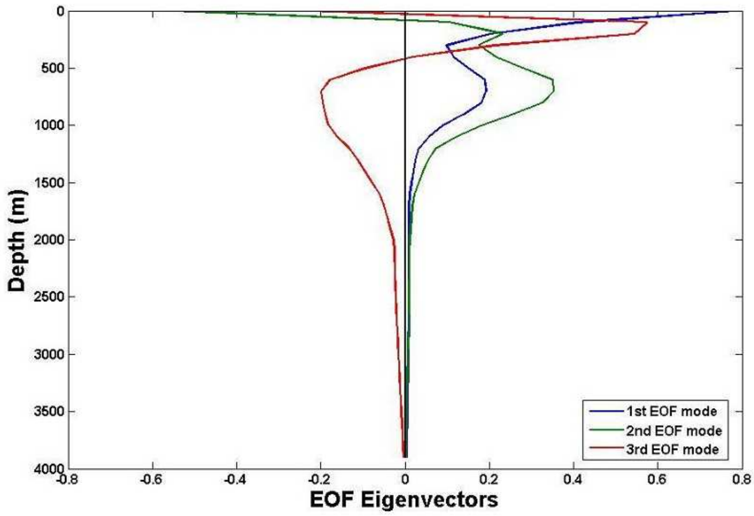

(b)

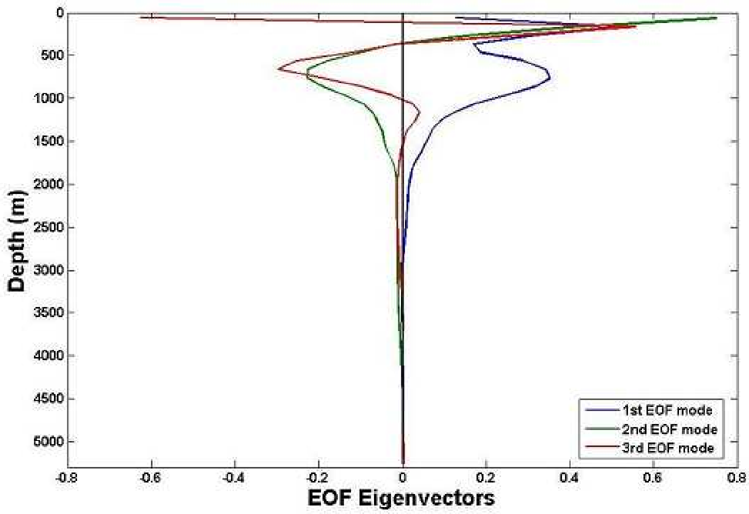

(c)

FIGURE 4.6: Temperature EOF modal structure: (a) WB2; (b) WB3; (c) WB5. 1st EOF mode (Dark Blue) representing the barotropic mode; 2nd EOF mode (Green) representing the 1st baroclinic mode; 3rd EOF mode (Red) representing the 2nd baroclinic mode.

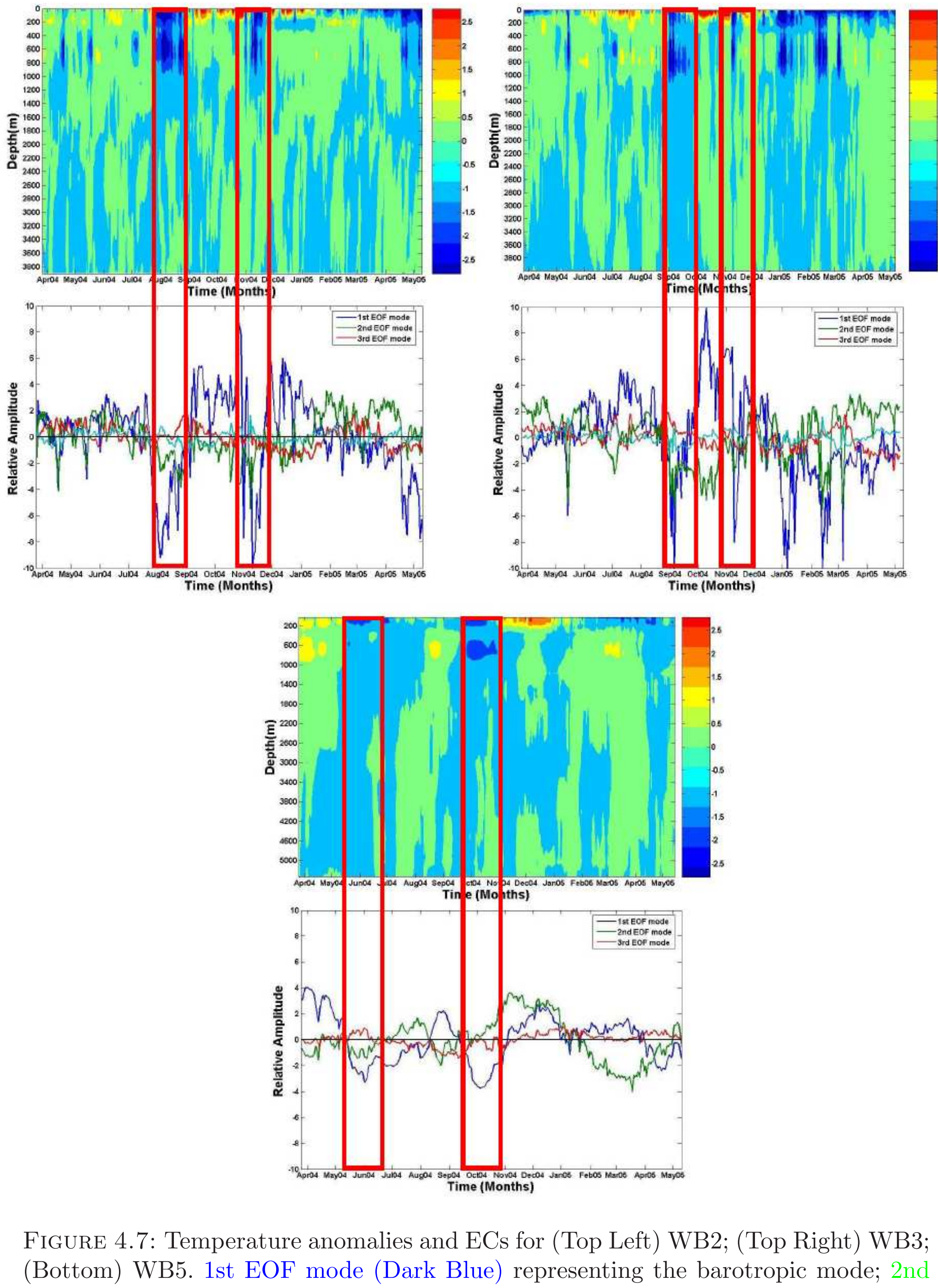

Figure 4.7: Temperature anomalies and ECs for (Top Left) WB2; (Top Right) WB3; (Bottom) WB5. 1st EOF mode (Dark Blue) representing the barotropic mode; 2nd EOF mode (Green) representing the 1st baroclinic mode; 3rd EOF mode (Red) representing the 2nd baroclinic mode.

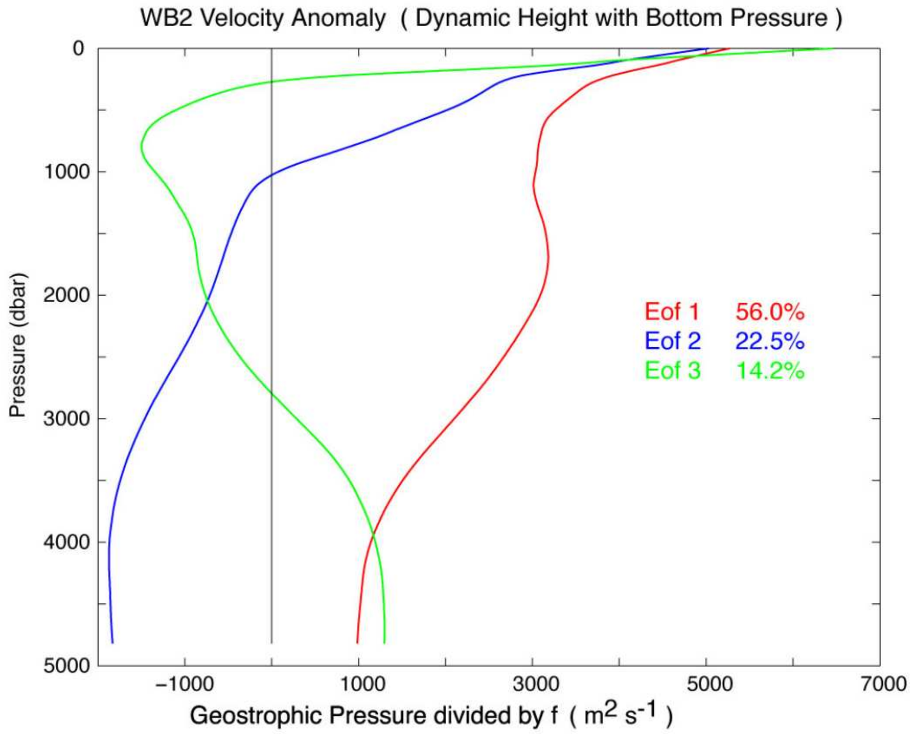

FIGURE 4.8: Dynamic height with bottom pressure EOF modal structure from April 2004 to May 2005 for WB2. 1st EOF mode (Red) representing the barotropic mode; 2nd EOF mode (Blue) representing the 1st baroclinic mode; 3rd EOF mode (Green) representing the 2nd baroclinic mode.

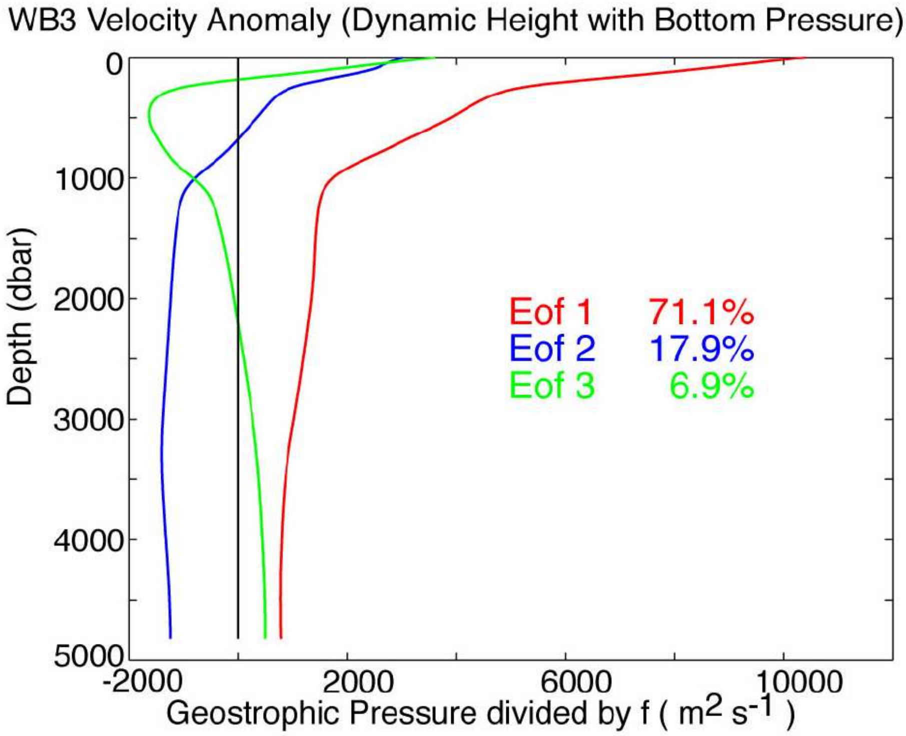

FIGURE 4.9: Dynamic height with bottom pressure EOF modal structure from April 2004 to May 2005 for WB3. 1st EOF mode (Red) representing the barotropic mode; 2nd EOF mode (Blue)representing the 1st baroclinic mode; 3rd EOF mode (Green) representing the 2nd baroclinic mode.

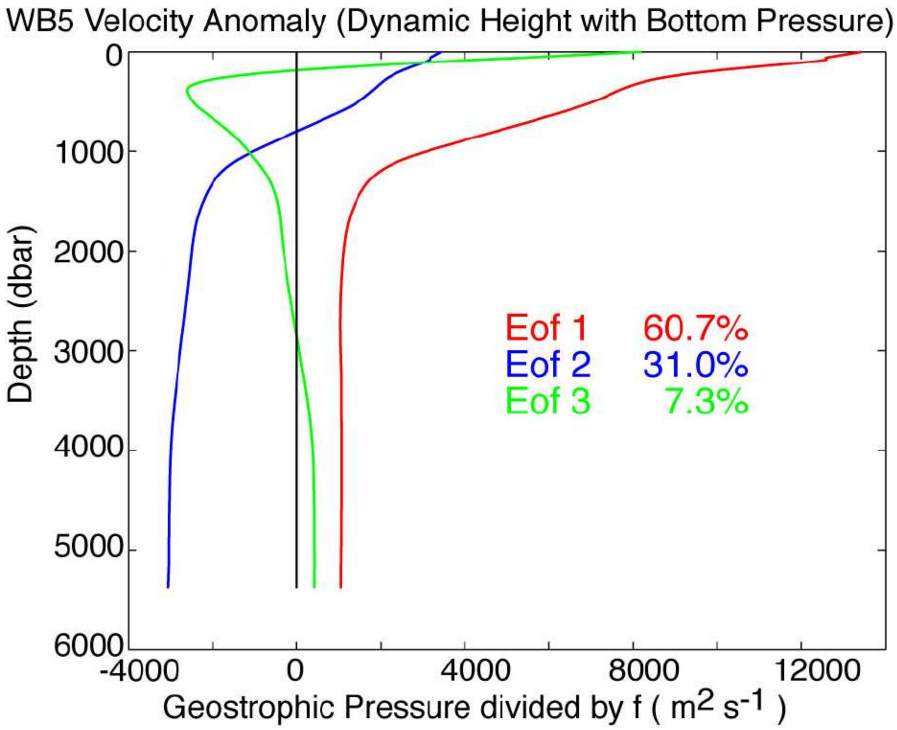

FIGURE 4.10: Dynamic height with bottom pressure EOF modal structure from April 2004 - May 2005 for WB5. 1st EOF mode (Red) representing the barotropic mode; 2nd EOF mode (Blue) representing the 1st baroclinic mode; 3rd EOF mode (Green) representing the 2nd baroclinic mode.

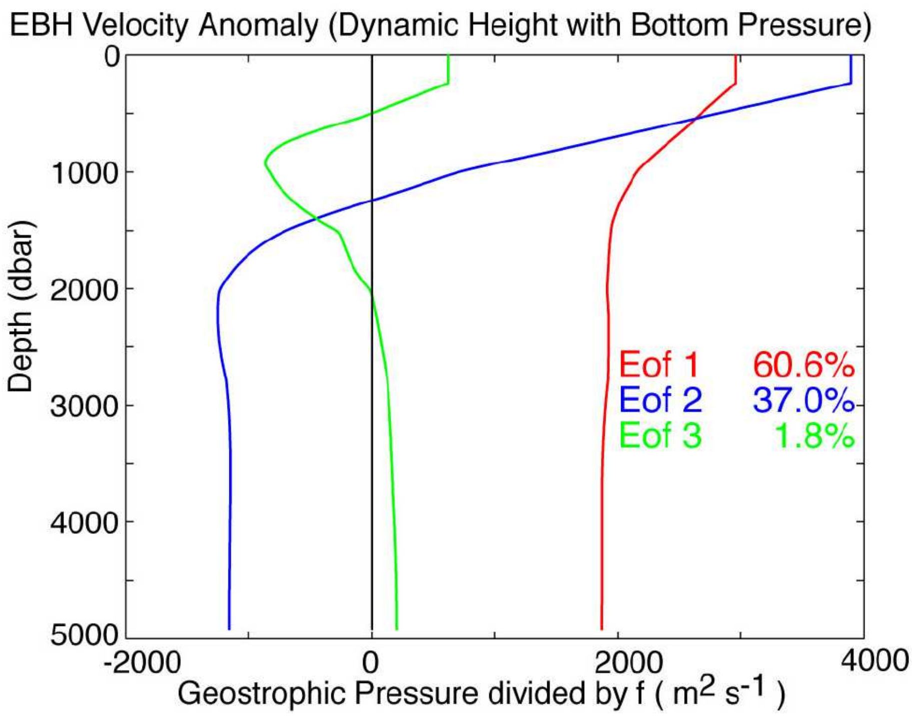

FIGURE 4.11: Dynamic height with bottom pressure EOF modal structure from April 2004 - May 2005 for EB1. 1st EOF mode (Red) representing the barotropic mode; 2nd EOF mode (Blue) representing the 1st baroclinic mode; 3rd EOF mode (Green) representing the 2nd baroclinic mode.

Chapter 5

Assimilating Altimetric and Mooring Data

5.1 Chapter Overview

Chapter 5 contains investigations into a novel technique toward studying the temporal-spatial variability of sub-surface mooring signals versus the surface altimeter signals in the western boundary 26.5 °N. We can evaluate the inter-relationship between the surface and sub-surface signals, and results here can determine the prospect of using limited surface datasets to reflect and infer the sub-surface signals. Ultimately, we would provide a relationship scheme for use in further comparison schemes in variability studies. From these assimilation efforts, we can better observe and understand the mechanisms in adjustments to various forcings within basin wide circulation.

The aims of the chapter are highlighted to simplify the research:

1. To determine if the surface and sub-surface properties are related on all timescales
2. To determine the ability of RAPID-MOC and MOCHA set-up to detect basin scale adjustments to forcings

5.2 Introduction

The associated components such as pressure, temperature, salinity, density are dynamically linked to patterns of motion in oceans. However, there has been a lack of studies determining the relationship between the surface and sub-surface properties on either short, seasonal or long timescales. Here we have the opportunity to use DUACS gridded Sea Surface Height (SSH) products, interpolated onto RAPID mooring locations along 26.5 °N to produce SSH time series at mooring sites. We will be comparing SSH with Dynamic Height (DH) time series.

5.3 Results and Discussion

5.3.1 Comparing SSHA and DHA Observations

To test if changes in the Dynamic Height Anomaly (DHA) datasets are reflected in the Sea Surface Height Anomaly (SSHA) datasets, the cross-correlation of the SSHA versus DHA is done to see the degree of similarity and time-lag. The DH dataset were scaled by *10 (taking into account the factor of gravity which is included in standard calculations of DH). At first we inspect to find that the DHA sampled daily to produce the time series which shows higher frequency variability than the SSHA dataset which have time series resolution of 7-day sampling intervals, with similar pattern but appearing damped of SSHA time series. Visual correlation is very strong, with the variability in same amplitudes and even stronger visual correlation in WB3 than WB2. Further calculation shows that the similarities (correlation expressed as percentage) between the DHA and SSHA at mooring positions from inshore WB2 (Fig.5.1), to further offshore WB3 (Fig.5.2) and WB5 (Fig.5.3) can be calculated to be 54.4%, 79.7% and 83.5% respectively. This steady increase in similarity is probably due to the difficulties of mooring sampling inshore (boundary and topographic effects) and 'cleaner' unaffected mooring sampling offshore. This shows that the changes in DHA are reflected to a high degree in the changes seen in SSHA.

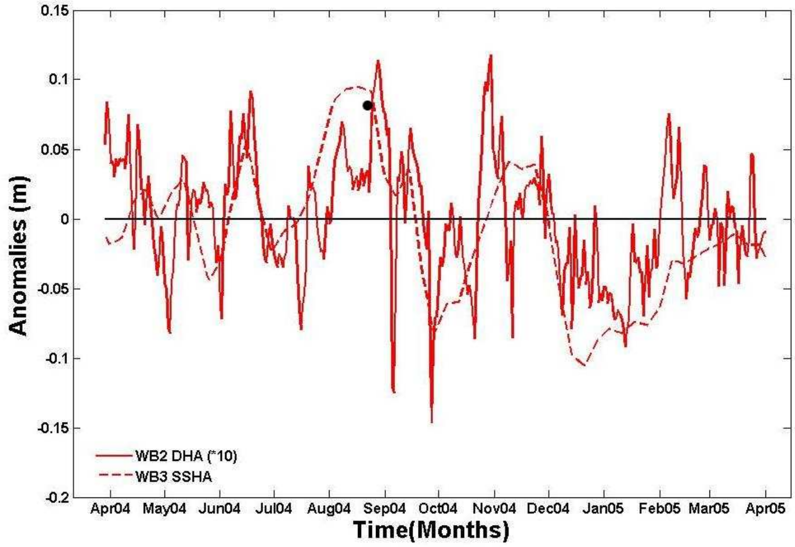

FIGURE 5.1: Temporal variability of SSH versus DHA at WB2, with 54.4% similarities.

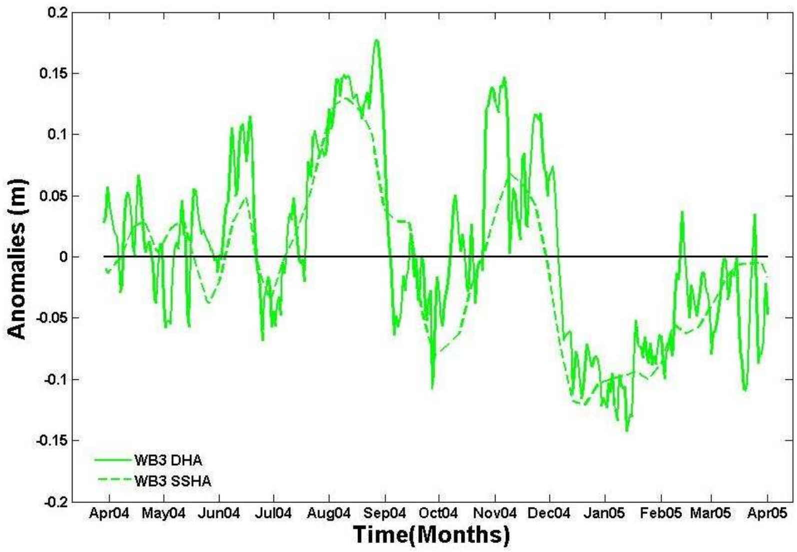

FIGURE 5.2: Temporal variability of SSH versus DHA at WB3, with 79.7% similarities.

5.3.2 Decreasing variability at the western boundary

Satellite SSH was found to be correlated to DH as measured on moorings WB2, WB3 and WB5 - with similar amplitude and time evolution (Table 5.1 and Fig.5.1, 5.2 and 5.3). Variability in SSH and DH unexpectedly decrease as the western boundary is approached. The primary Rapid measurements have a good zonal resolution near the western boundary 26.5 °N.

Further results of the satellite SSH in the western boundary (Fig.5.4, 5.5

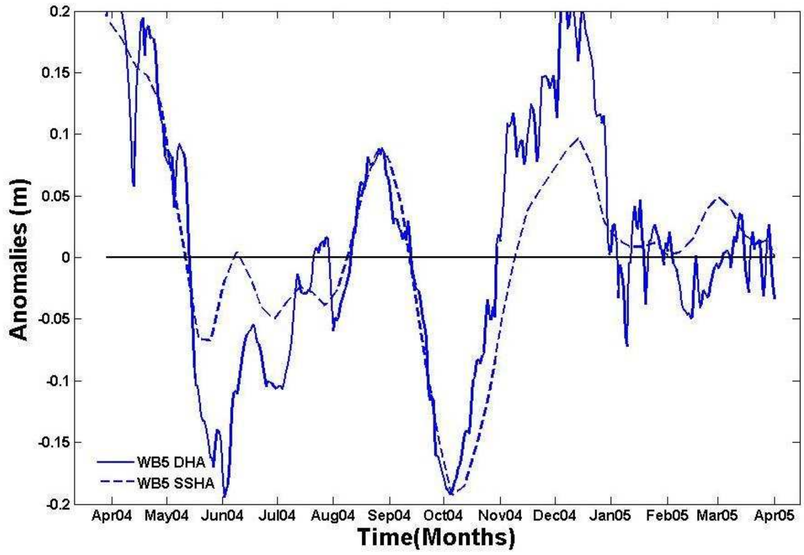

Figure 5.3: Temporal variability of SSH versus DHA at WB5, with 83.5% similarities.

Table 5.1: Comparison of Sea Surface Height (SSH) and Dynamic Height (DH) standard deviation shows marked decrease in variability toward the western boundary. In parentheses is the std in SSH for the period 1992 to 2005.

Site	SSH (cm)	DH 100 dbar (dynamic cm)	DH 0 dbar (dynamic cm)
wb2	4.83 (5.50)	3.46	4.66
wb3	6.22 (6.78)	5.40	7.24
wb5	7.66 (9.66)	8.64	10.57

and Table 5.1) also show a band of decreasing variability approaching the western boundary coastline. In figures the standard deviation (std) in DH at moorings WB2, WB3, WB5 and EBH are indicated by crosses at the appropriate longitudes, and the std in SSHA are indicated by the lines. The bold lines are SSHA from 1992 to 2008 and where applicable, dotted lines are from individual periods of interest. The horizontal scale is expanded in the west to show the sharp drop in SSH and DH variability as the western boundary is approached. This is a major surprise as seen previously in SSH standard deviations and SSH error estimations in Chapter 2 and 3. On its own, the striking decrease at the boundary might have been considered a result of the boundary effects of satellite altimetry aliasing in course of avoiding land effects in satellite measurements. However since both the DH and SSH time series display such a decrease in variance with similar timescales and periods, combined with knowledge from the error maps of SSH in Chapter 2, we determine that in the observations are 'real'. The observations of the 100 dbar DH, there is the decrease is from 8.6 dynamic centimetres at WB5, 500 km from the boundary, to 5.4 at WB3 50 km from the shore, to 3.5 at WB2 23 km from Abaco. Besides, as the variability reduces as we go inshore, it is important to note the importance to measure as close to the western boundary as possible to obtain the best results of baroclinic transport variations. The western boundary dynamics seem to exert a constraint on the size of variability relative from offshore to inshore. Work presented here about the decrease in SSH and DH brought about much interested and attention, and further work was then done (Kanzow et al., 2009) to describe the interaction of propagating features in the western boundary including the factors bringing about this observation of a sharp decrease in amplitudes at the coasts.

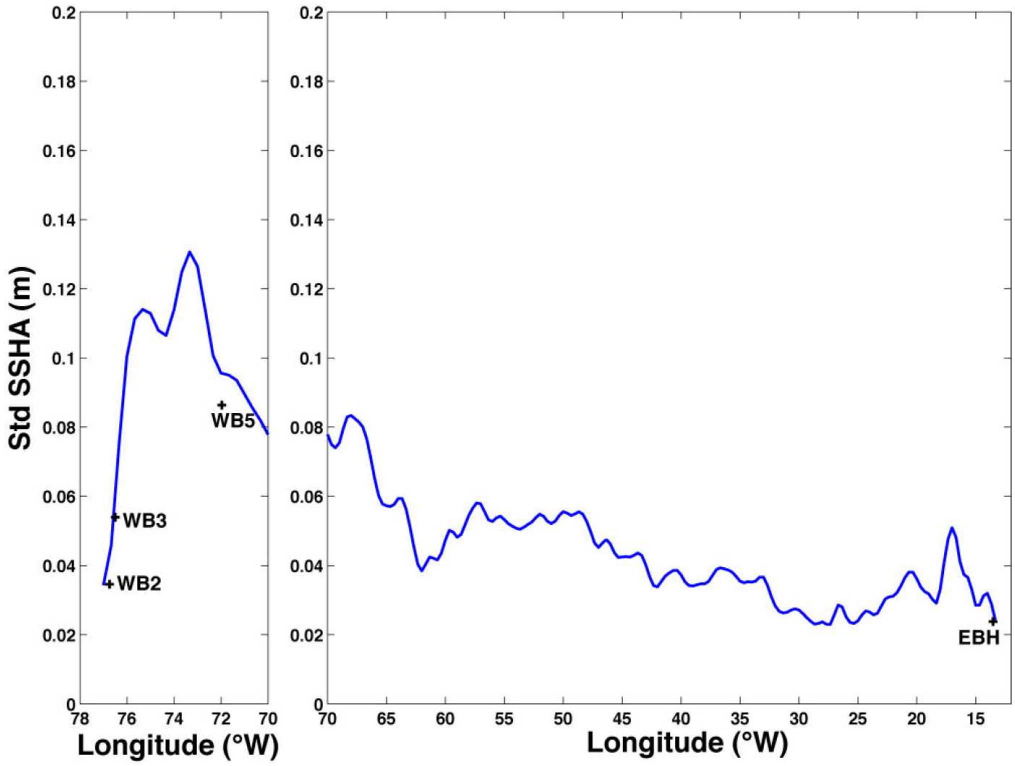

FIGURE 5.4: Standard deviation in SSHA variability at 26.5 °N showing a band of decreasing variability approaching the western boundary coastline.

Feasibility studies (Cromwell et al., 2007; Häkkinen, 2001) have shown that it may

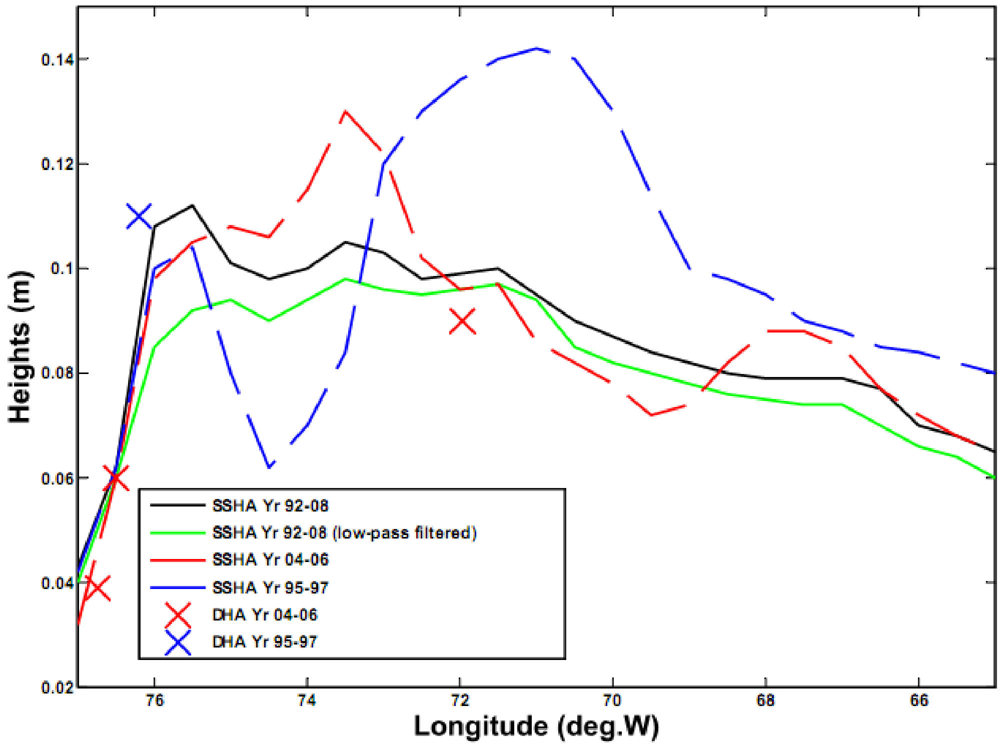

FIGURE 5.5: Standard deviation in SSHA and DHA variability at 26.5 °N from 1992 to 2008 showing a band of decreasing variability approaching the western boundary coastline.

be posibble to monitor the AMOC from satellite observations. Prediction tests show that it is best to have sufficiently long time series (∼10 years) but initially, we are confident that the altimetry can already provide complementary surface datasets and hold a key to extending the monitoring array's capabilities. Here the fact that both the moorings and the satellite observations are depicting the same picture brought much light to the increasing possibility and ability of satellites to capture the variability.

5.3.3 Crossbasin local baroclinic variability

We can observe the variance in the western boundary baroclinic transport variability (Sv) (Figure 5.6 as calculated from DHA profiles vertically integrated daily and divided by the Coriolis parameter). Variance in the western boundary counterpart moorings are 5 times larger than in the eastern boundary with std of 7.9 Sv and 3.3 Sv respectively. Using the same depth intervals as Cunningham et al. (2007), we vertically integrate over the layers to estimate the transport variability in the individual layers (Table 5.2). From Figure 5.6 and Table 5.2 we can note that the local baroclinic transport variability in the surface thermocline recirculation layer is only slightly larger in the west compared to the east. However, the baroclinic transport variability in the deep water transports are much greater in the west versus the east. This result was expected as there is little deep transport variability in the eastern boundaries, as also found in Longworth (2007) from analysis of historical hydrographic stations.

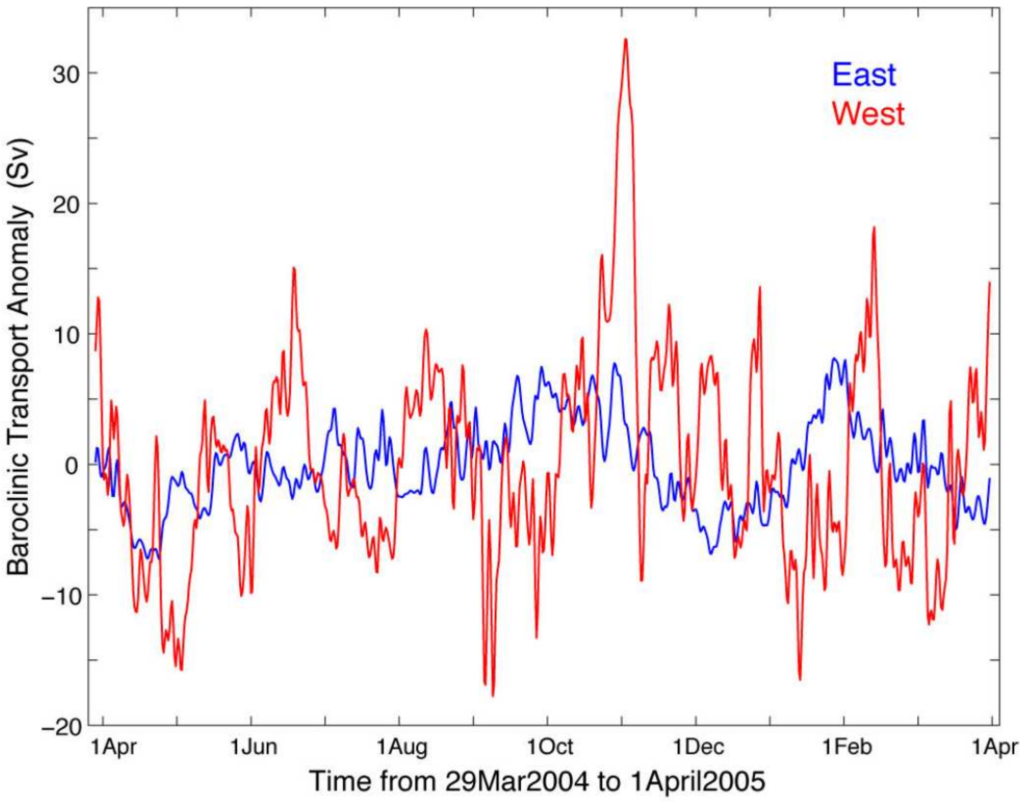

FIGURE 5.6: Baroclinic transport variability near the western and eastern boundaries

Firstly, we recall back at section 3.5.2 where the BP in the western Atlantic basin at 26.5 °N has slightly higher variances than the BP in the eastern basin. However, any change in temperature or salinity can cause fluctuation in measurements of local baroclinic transport (baroclinic transport anomalies). At the energetic western boundary, we expect they can be from any forcing such as from westward propagating Rossby waves or eddies hitting the western boundary, or even southward propagating Kelvin waves trapped travelling along the continental slope. In the Eastern boundary,

Table 5.2: Std of Baroclinic Transport (Sv)

Depths (m)	East	West
Overall	3.32	7.89
Thermocline Recirculation (0 - 800)	2.43	2.97
Intermediate Waters (800 - 1100)	0.49	0.87
Upper North Atlantic Deep Water, UNADW (1100 - 3000)	0.70	4.22
Lower North Atlantic Deep Water, LNADW (Below 3000)	0.08	0.77

forcings can include upwelling mechanisms or northward propagating Kelvin waves trapped travelling along the continental slope. With reference to Cunningham et al. (2007), in their calculations of mass compensation in a basin scale flow, it is assumed that the baroclinic transport anomaly is compensated by the barotropic variability (depth independent barotropic adjustment). In a localised point (e.g. where moorings are), the barotropic adjustments is reflected by a change in the BP. Effectively, this is measured from the vertical integration of the BPA (by method of BPA $*$ 4800 m depth layers) which cancels out the baroclinic transport anomalies. Using this we can determine the overall compensating BPA at any mooring, by which the total variability (overall transport anomaly of barotropic transport plus baroclinic transport) equals zero.

From observations, we note the predicted BPA correlated to the observed BPA. The strongest correlation (0.62) is found at WB2 (the western most boundary mooring) as seen in Fig.5.7. The observed BPA and predicted BPA at WB2 have similar amplitudes and no phase shift. The BP (blue) at the western boundary seems to be responding to local changes in temperature and salinity variability by compensating for variations in baroclinic transport fluctuations (red). The black line shows the difference between the BPA and predicted BP. Both the blue and red lines are offset by +0.06 dbar.

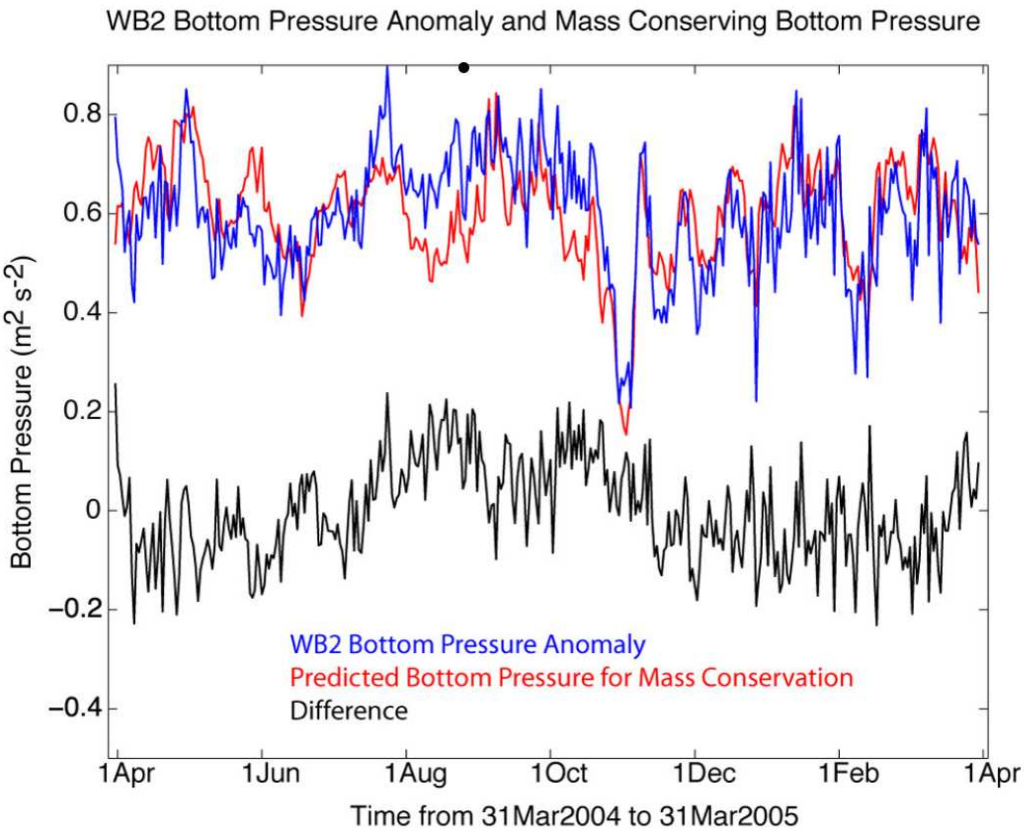

FIGURE 5.7: Baroclinic variations at the western boundary are locally compensated by bottom pressure, both offset by +0.06 dbar.

This is seen clearly in an example of the November 2004 event mentioned previously in section 3.5 and subsection 4.5.1. The November 2004 event (reproduced here again in temperature datasets Fig.5.8) displays large fluctuation in baroclinic transport and bottom pressure time series (Fig.5.6 and 5.7). As mentioned before, the temperature vertical structures show warming, and the deepening of isotherms by up to 700 m especially in the deeper waters. The change in temperature affects the DHA, and reflects as a positive fluctuation in the DHA as shown in Fig.5.9. If the eastern boundary DHA remains unchanged, then a positive DHA means a southward mid-ocean transport anomaly. In this case, the baroclinic transport anomaly at WB2 is more than 30 Sv (as seen in Fig.5.6), and we can predict the BPA to compensate the transport anomaly by calculating the negative offset of the vertical integration of DH at the mooring site. We find that the predicted BPA values are almost equal to the observed BPA at WB2. We then take a next step by trying to produce a vertical structure of the mid-ocean transport per unit depth profile Fig.5.9. We do this by combining the dynamic height profile values (blue line) with the predicted BPA to create a profile of predicted BPA plus the DHA (green line). Then this is subtracted from the observed mean transport per unit depth profile values (black line). This produces the intended mid-ocean transport per unit depth profile (red line) which depicts the stoppage to southward flowing LNADW at depths below 3000 m, and the reversal of the northward flow below 3500 m as described by Johns et al. (2008) who observed similar events using direct measurements obtained from the project as well.

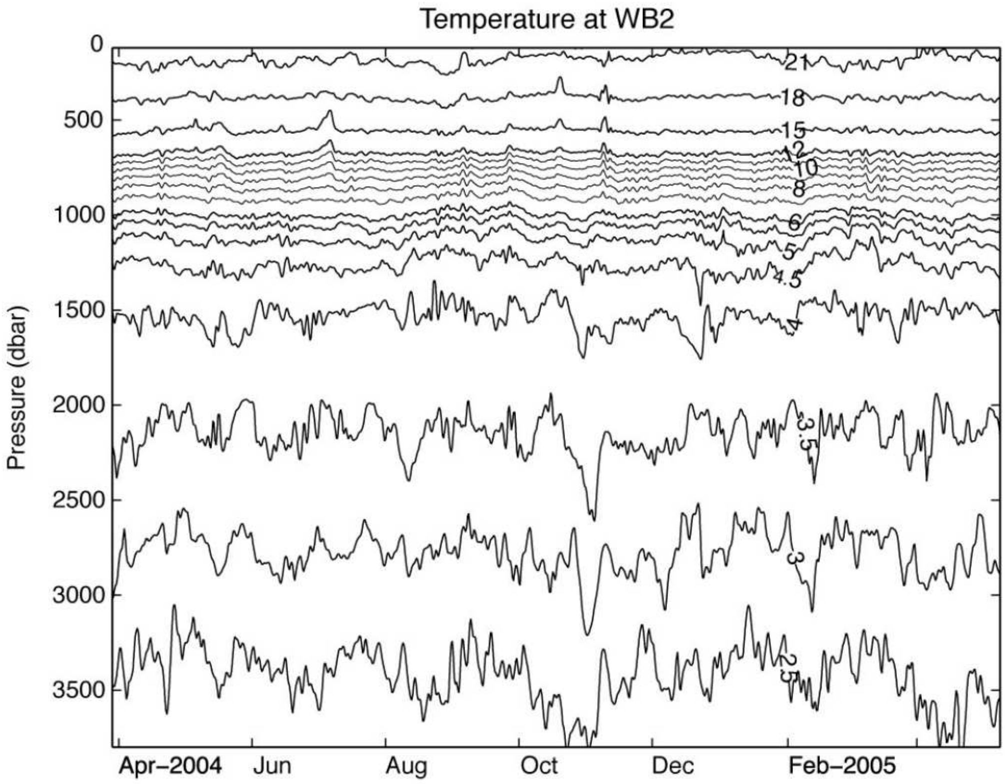

FIGURE 5.8: November 2004 Event in Temperature Datasets at Mooring Site WB2

5.3.4 Variations with Transport Fluctuations.

We then move further to determine the mechanism by which the bottom pressure fluctuations compensate with some of the components of the AMOC (Gulf Stream, Ekman and mid-ocean transport). We test this at mooring WB2, by trying to obtain the residual geostrophic transport (barotropic transport) in order to compare how the reduced BPA relate to the Gulf Stream transports. Firstly, we remove the predicted BP required to compensate the local baroclinic transport from the observed BPA at WB2

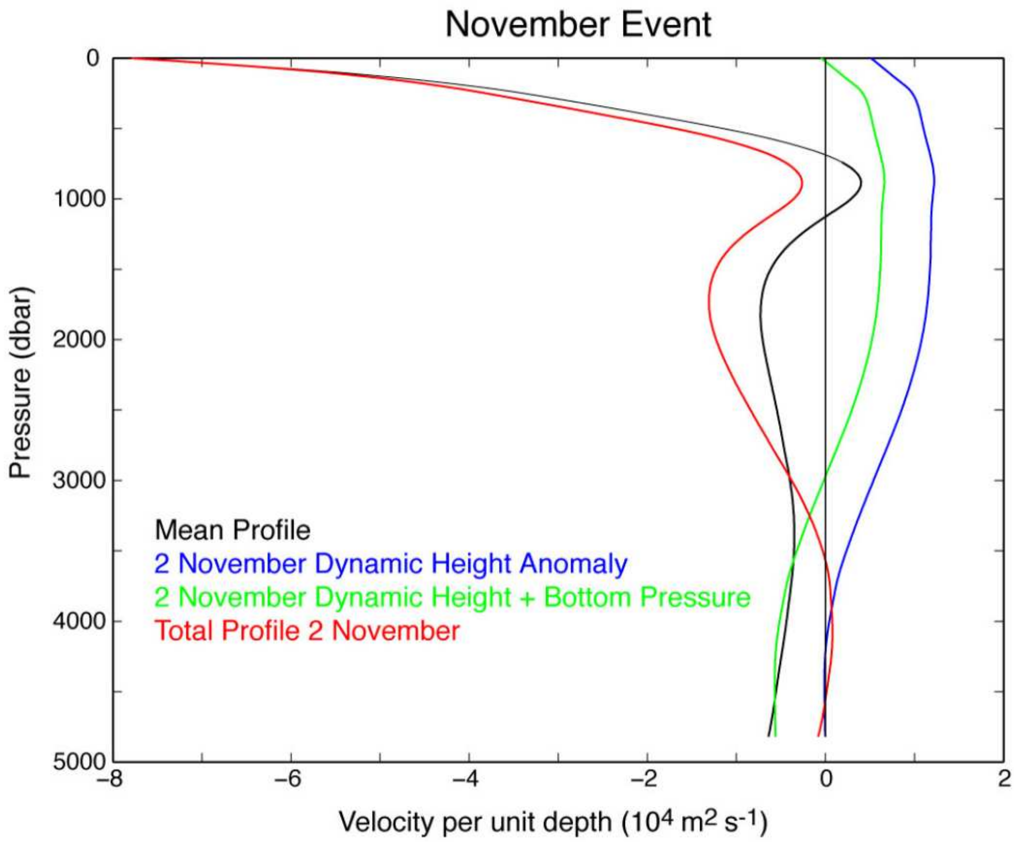

Figure 5.9: Vertical structure of the mid-ocean transport per unit depth profile during the November 2004 event at WB2 mooring site.

to obtain residual BP time series (black line in Fig.5.7. We then derive a time series of geostrophic mid-ocean transport due to fluctuation at WB2 by multiplying the reduced BP by the depth (4000 m) and further divide by the Coriolis parameter. So essentially, we have removed the baroclinic transport anomaly compensating the predicted BP and are now left with the residual geostrophic transport which is in essence barotropic. We then do comparisons with Gulf Stream transports which resulted in daily correlation of 0.51 and 0.62 for 10-day low pass filtered values. There was significant correlation as previous work by Cunningham et al. (2007) have estimated the integral time scales for temporal variability in the time series used here to be 24 days. In this dataset, the correlation between the residual geostrophic transport and the Gulf Stream transport have 13 degrees of freedom, from which we determine that correlations greater than 0.514 are significantly different at a 95% confidence level.

From the following figure showing the residual bottom pressure variations after subtracting the variations due to baroclinic transport variability are correlated (0.62) to Gulf Stream Transport (Fig.5.10) with similar amplitudes. This would imply that higher Gulf Stream tranport is correlated to higher bottom pressure (southward barotropic geostrophic flow) at the western boundary 26.5 °N (at mooring site WB2). The correlation relationship worsens further offshore at mooring site WB3 (0.34) and vanishes at mooring site WB5. Thus, the Gulf Stream transport fluctuations appear to be compensated by local transport fluctuations just east of the Bahamas.

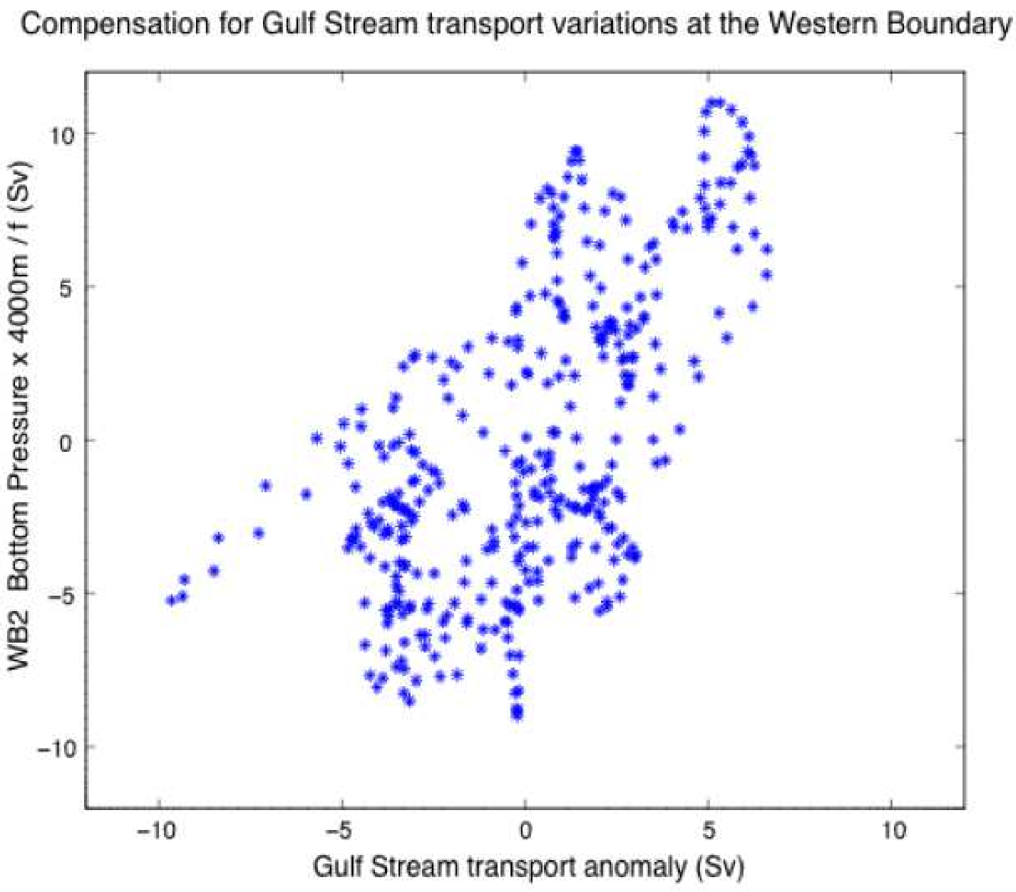

FIGURE 5.10: Scatterplot of residual bottom pressure variations after subtracting the variations due to baroclinic transport variability are correlated (0.61) to the Gulf Stream Transport

Previous simulated observations estimate variability of 6 Sv from r.m.s. variability from models of hydrographic sections (Ganachaud, 2003) and projected r.m.s. variability from datasets of satellite altimetry estimating SSH variability associated with eddies concluded it should be as high as 16 Sv (Wunsch, 2008). This is significantly different from estimates by Cunningham et al. (2007) who estimated the standard deviation of the upper mid-ocean transport to be 3.32 Sv. Here, our results from mooring observation show that the variability in upper (0 - 800 m) mid-ocean transport to be 2.97 Sv, a factor 2 to 5 times smaller than previous modelled observations. We propose (Kanzow et al., 2009) that the smaller variability at the western boundary could be due to: (i) eddy variability, reducing drastically while approaching the western boundary; (2) strong constraints at the western boundary by means of compensation between components of the overturning so the overall variability is smaller in comparison to the components.

In light of results from Kanzow et al. (2007) who found compensation between 'internal' components and 'external' components of variability modes, the results here show the overall standard deviation of baroclinic transport, essentially the 'internal mode' (i.e. std 7.89 Sv) is largely compensated by the BP, essentially the 'external mode'. In the case of the November 2004 event for example, the baroclinic transport anomaly of more than 30 Sv which is mostly concentrated in the deep water of the western boundary current is locally compensated by the observed BP variability (which is depth independent). This results in what we see in the vertical structure of the 'stoppage' in the deep tranport anomaly and leaving only the small anomaly of 2.97 Sv in the overturning. However BP compensation is not as effective for the shallow Gulf Stream transport. As this northward flow increases, the BPA would increase to compensate leading to a stronger southward transport. But as the compensation is barotropic, only around 20% of the compensation will occur to compensate the shallow Gulf Stream flows (in the upper 800 m) whereas the rest will be observed as variations in the overturning.

5.4 Summary

We began this chapter to determine if we could use a novel technique toward studying the temporal-spatial variability of sub-surface mooring signals in this case the dynamic height (DH), and bottom pressure (BP), versus the sea surface height (SSH) altimeter signals, in the western boundary 26.5 °N. In this case, upper ocean (surface to 100 m depths) DH time series are found to be highly correlated to SSH time series especially near to the coast in the western boundary. These results determine that there is good prospect of using limited surface datasets to reflect and infer some sub-surface signals but care must be taken as the relationship deteriorates away from the western boundary continental slope. Also, it is hard to use SSH to infer detailed vertical structure because the SSH is not correlated to the BP and sub-surface events in the time series, such as the November 2004 event have no strong SSH signal. Another surprise is that the variability in the western boundary is observed to be much smaller than previously modelled based on datasets from hydrographic section or SSH. The mooring observation shows the upper mid-ocean transport (0 to 800 m) variability to be about 3 Sv. From these assimilation efforts, we can better observe and understand the mechanisms in adjustments in strength and structure to various forcings within basin wide circulation. It was found that the variations in components of overturning such as the Gulf Stream or deep water boundary current transports are compensated in a barotropic manner by bottom pressure fluctuations.

Chapter 6

Conclusions and Future Work

6.1 Overall Summary and Conclusions

In the beginning, we started with an idea to study the low frequency variability especially near the western boundary by giving a review on its features. Early work involved suitable preparations including the appropriate filtering, interpolations and gridding before spectral analysis of the sea surface height (SSH) dataset since 1992 up to 2006 (combination of TOPEX/ Poseidon, T/P and Developing Use of Altimetry for Climate Studies, DUACS) was performed. We find that the western boundary at 26.5 °N is a complicated region, with the RAPID-MOC and MOCHA array moorings in positions which will capture significant temporal-spatial variability from propagating as indicated in the spectral analysis. These features tracked from offshore decreased speed by 22%) and losing about 70% of their features variability from the offshore western boundary mooring of WB5 (500 km from Abaco) to the inshore mooring nearest to the western boundary at WB2 (23 km away from Abaco). At WB2, upper waters representing the Antilles Current (AC) and deeper waters representing the Deep Western Boundary Currents (DWBC) showed different dominant periodicities although this was not reflected in the spectral analysis at WB3. Also, the variability at the western boundary was found to be maximum at WB5 (from SSH standard deviation, std) but the variability drops drastically inshore. This is significant and not due to sampling errors. Further analysis of the vertical structure of the water column at individual moorings in the western boundary is done to characterise the temporal-spatial variability from the first year mooring deployment datasets from the RAPID-MOC and MOCHA array moorings at 26.5 °N.

Firstly, the mooring datasets were pre- and post- calibrated to meet British Oceanographic Data Centre (BODC) quality standards, appropriately filtered, interpolated and gridded before further analyses including creation of anomaly datasets. From the vertical structure, we see the decoupled AC-DWBC upper and deeper ocean regime in all the western boundary moorings datasets in either meridional velocities and temperatures. The DWBC is significantly weaker at WB2 compared to WB3 however a significant event in November 2004 is clearly depicted as a 'stoppage' of the DWBC reflected in its meridional velocities and temperature anomalies. This was considered to be a possible on-off event; however more in-depth study of the 11 year historical dataset in the area needs to be made. Bottom pressure (BP) datasets were also vital however much care needed to be taken in its filtering so as not to remove the dynamically important components of local variability. In all, these are important results showcasing the advantage of high resolution temporal-spatial scale of the trans-Atlantic moorings in comparison to shipboard sampling strategies.

It is important to pursue the course of determining the changes within the vertical structure by decomposing and projecting the dataset into statistical modes to determine modes of variability. At the western boundary 26.5 °N, the higher modes (mode 1 to mode 3) which represent the barotropic, first baroclinic to second baroclinic modes, contribute significantly to variability. Between 92 to 99% of variance can be explained by the first three geostrophic pressure profile modes and between 82 to 97 % of variance can be explained in the meridional velocity modes. In addition, the statistical modes (for example, meridional velocity vertical modes) can reflect the dominant modes and the physical contribution at any time within the time series. We find different barotropic, baroclinic and even coupled barotropic-baroclinic modes within the datasets. This gives greater confidence in using statistical modes to predict vertical structure and quantify the proportion of variability.

Finally, we approach the possibility of studying the temporal-spatial variability of the mooring datasets using satellite datasets. It was found that the surface dynamic height (DH) and sea surface height (SSH) datasets are highly correlated close to the western boundary but the correlation deteriorates further offshore. Both the surface DH and SSH depict the decreasing variability in the western boundary and this leads to the substantial finding that the variability approaching the western boundary is much smaller than previously modelled based on datasets from hydrographic section or sea surface height (SSH). The mooring observations show that the upper mid-ocean transport (0 to 800 m) to be about 3 Sv. The bottom pressure (BP) dataset showed the North Atlantic basin 'filling' and 'draining' instantaneously but also as expected - uncorrelated to sea surface height (SSH) and surface dynamic height (DH). In this case, upper ocean (surface to 100 m depths) DH time series are found to be highly correlated to SSH time series especially near to the coast in the western boundary. There is therefore good prospect in the future of using limited surface datasets to reflect or infer sub-surface signals but care must be taken as the relationship deteriorates away from the western boundary continental slope. Also, it is hard to use SSH to infer detailed vertical structure because the SSH is not correlated to the BP and sub-surface events in the time series, such as the November 2004 event,which have no strong SSH signal. However from these assimilation efforts, we have been able to better observe and understand the mechanisms involved in the compensation of the various forcings at the western boundary 26.5 °N and the basin wide circulation especially from the DH and BP records. The events such as the November 2004 event clearly show the manner in which the forcings such as the Gulf Stream and deep water boundary currents in the western boundary are compensated in a barotropic manner by the bottom pressure fluctuations. As the interior component of the MOC relies on the end-point data of DH and BP, understanding compensation mechanisms at the boundaries is crucial in measuring the general MOC.

In answering the aims of the thesis, we utilized measurements from a unique combination of sub-surface and surface properties to provide new insights into effects of propagating features to the dynamics and variability at the western boundary 26.5 °N.

The key statements from overall discussions of the chapters are:

1. it is possible to characterise the temporal-spatial variability of propagating features using observations from altimetry and moorings especially in the western boundary Atlantic at 26.5 °N. The propagating features with short periods and high frequency in the western boundary show that eddies affect the mooring datasets and must be accounted for. The propagating features can be tracked and are found to have the same characteristics in datasets of western boundary 26.5 °N derived from mooring datasets of sub-surface properties and from satellite altimetry. We can determine that propagating features contribute significantly to various scales of temporal-spatial variability in the western boundary 26.5 °N.

2. by using vertical modal structure derived from the observations and the boundary conditions imposed, we identified the relative contributions of higher modes (mode 1 to mode 3) to the variability at western boundary 26.5 °N are high. We found the extent to which statistical vertical modes and theoretical vertical modes explain the variability especially for velocity and dynamic height modes further offshore. There is great prospect of using statistical modes to predict the vertical structure. We also found that propagating features can be observed within the vertical structure and their variability can be quantified in proportion to the observed temporal-spatial variability.

3. by using a novel technique we study the temporal-spatial variability of sub-surface mooring signals versus the surface altimeter signals in the western boundary 26.5 °N. There is good prospect of using limited surface datasets to reflect and infer the sub-surface signals especially nearer to the western boundary at WB2. The relationship at the mooring sites can be used in further comparison schemes in variability studies of the region. We can observe and understand the mechanisms involved in the compensation of the various forcings at the western boundary 26.5 °N and the basin wide circulation.

6.2 Limitations and Future Work

Overall during the course of the project, many challenges have been faced by the author, lacking both programming knowledge and background in observational work being the main difficulties. However, the programs created during the course of the Ph.D., from writing the simple and humble routines of time conversions, to analysing the large amount of various datasets, which can now be easily applied to future mooring observation analysis. There are certain limitations and further work within the datasets and methods used in the present work which could be improved in future work and which could enhance various points discussed. Firstly, the moorings located at 26.5 °N were chosen for numerous reasons, among them the fact that historical datasets were available. In future work, all the available datasets from RAPID-MOC and MOCHA mooring array should be used. This would give a longer time series, and in addition to include the time series that would be obtained from RAPID-Watch ending in 2014 to have decadal time series. Secondly, it would be beneficial to expand all the analysis involved in comparing the simultaneous combination of the spatial-temporal observations of various sub-surface and surface properties. It would also be beneficial to have more in-depth study of the propagating features within the numerical modelling domain with comparisons of present 'real' *in-situ* observations as from Kanzow et al. (2009) included in this thesis. In calculations of the geostrophic pressure profiles (and geostrophic transport), the end stations used were in fact merged profiles of numerous stations 'climbing' the Western and Eastern boundaries. This was done to maximise the depth over which the AMOC was calculated. The moorings were stationed at different points along the zonal section and aliasing may affect the accuracy of results, although work by Hirschi et al. (2003) indicated that the stations are able to resolve the AMOC well enough. This project has yielded much information not previously known about the western boundary and therefore future work on gaining such long term high resolution datasets should be continued. Further research into the investigations of propagating features using different techniques including 3-D Radon Transform might be beneficial to understanding the interaction at the boundaries. Also the use of other statistical methods such as wavelet transform to characterise the variability of the future longer time series from mooring datasets with comparisons to other satellite datasets could prove to be illuminating.

References

Baehr, J., Hirschi, J., Beismann, J. O., Marotzke, J., 2004. Monitoring the meridional overturning circulation in the North Atlantic: A model-based array design study. Journal of Marine Research 62, 283–312.

Baringer, M. O., Larsen, J. C., 2001. Sixteen years of floridacurrent transport at 27°N. Geophysical Research Letters 28, 3179–3182.

Bentson, M., Drange, H., Furevik, T., Zhou, T., 2004. Simulated variability of the meridional overturning circulation. Climate Dynamics 22, 701–720.

Broecker, W. S., 1991. The great conveyor belt. Oceanography 4, 79–89.

Bryden, H., Mujahid, A., Cunningham, S., Kanzow, T., 2009. Adjustment of the basin-scale circulation at 26 °N to variations in gulf stream, deep western boundary current and ekman transports as observed by the rapid array. Ocean Science 6, 871 − 908.

Bryden, H. L., 1993. Ocean heat transport across 24°N latitude. In: McBean, G., Hantel, M. (Eds.), Interactions Between Global Climate Subsystems: The Legacy of Hann. American Geophysical Union, pp. 65–75.

Bryden, H. L., Imawaki, S., 2001. Ocean circulation and climate (Siedler, G., Church, J. & Gould, J., Eds.). Academic Press, Ch. Ocean heat transport, pp. 455–474.

Bryden, H. L., Johns, W. E., Saunders, P. M., 2005a. Deep western boundary current east of Abaco: Mean structure and transport. Journal of Marine Research 63, 35–57.

Bryden, H. L., Longworth, H. R., Cunningham, S. A., 2005b. Slowing of the Atlantic meridional overturning circulation at 25°N. Nature 438, 655–657.

Challenor, P. G., P. Cipollini, P., Cromwell, D., 2001. Use of the 3-d radon transform to examine the properties of oceanic rossby waves. Journal of Atmospheric and Oceanic Technology 18(9), 1558–1566.

Chang, P., Yamagata, T., Schopf, P., Behera, S. K., Carton, J., Kessler, W. S., Meyers, G., Qu, T., Schott, F., Shetye, S., Xie, S. P., 2006. Climate fluctuations of tropical coupled systemsthe role of ocean dynamics. Journal of Climate 19, 5122–5174.
URL `http://hdl.handle.net/2264/596`

Charria, G., Dadou, I., Cipollini, P., Drévillon, M., de Mey, P., Garçon, V., 2006. Understanding the influence of Rossby waves on surface chlorophyll concentrations in the North Atlantic Ocean. Journal of Marine Research 64, 4371.

Chelton, D. B., Schlax, M. G., 1996. Global observations of oceanic Rossby waves. Science 31, 234–238.

Chelton, D. B., Schlax, M. G., 2003. The accuracies of smoothed sea surface height fields constructed from tandem satellite altimeter datasets. Journal of Atmospheric & Oceanic Technology 20, 1276–1302.

Chelton, D. B., Schlax, M. G., Samelson, R. M., de Szoeke, R. A., 2007. Global observations of westward energy propagation in the ocean: Rossby waves or nonlinear eddies? Geophysical Research Letters 34, L15606, doi:10.1029/2007GL030812.

Cipollini, P., 2003. Multiple Satellite Observations of Oceanic Planetary Waves: Techniques and Findings. In: Dalle Mese, E. (Ed.), Proceedings of the 2003 Tyrrhenian International Workshop on Remote Sensing. pp. 134–143.

Cipollini, P., Cromwell, D., Challenor, P. G., Raffaglio, S., 2001. Rossby waves detected in global ocean colour data. Geophysical Research Letters 28, 323–326.

Cipollini, P., Cromwell, D., Jones, M. S., Quartly, G. D., Challenor, P. G., 1997. Concurrent altimeter and intrared observations of Rossby wave propagation near 36°N in the Northeast Atlantic. Geophysical Research Letters 24, 889–892.

Cipollini, P., Quartly, G. D., Challenor, P. G., Cromwell, D., Robinson, I. S., 2004. Manual of Remote Sensing (3rd Edition, A Series, Volume 6): Remote sensing of the marine environment (Ed. Gower J.F.R.). Tech. rep., Southampton Oceanography Centre, U.K.

Cipollini, P.and Challenor, P., Cromwell, D., Hill, K., Quartly, G., Robinson, I., 2000a. Remote Sensing of Oceanic Rossby Waves: New Techniques and Results. In: Proceedings of International Geoscience and Remote Sensing Symposium. IGARSS. Vol. 5. pp. 1824–1826.

Cipollini, P.and Challenor, P. G., Cromwell, D., Hill, K. L., Quartly, G. D., Robinson, I. S., 2000b. Recent advances in remote sensing of extra-tropical Rossby waves. In: Proceedings of Pacific Ocean Remote Sensing Conference, PORSEC. Vol. 1. pp. 271–275.

Colling, A., 2002. Ocean CIrculation 2nd Edition. Butterworth-Heinemann, Oxford.

Cromwell, ., Shaw, A. G. P., Challenor, P., Houseago-Stokes, R. E., Tokmakian, R., 2007. Towards measuring the meridional overturning circulation from space. Ocean Science 3, 223–228.

Cromwell, D., 2006. Temporal and spatial characteristics of sea surface height variability in the North Atlantic ocean. Ocean Science 2, 147–159.

Cunningham, S., 2005a. RRS Discovery Cruise 279 (4 April - 10 May 2004): A transatlantic hydrographic section at 24.5°N Cruise Report 54. Tech. rep., Southampton Oceanography Centre.

Cunningham, S. A., 2005b. RRS Discovery Cruise 277 (26 March - 16 April 2004) and RRS Discovery Cruise 278 (19 March - 30 March 2004): Monitoring the Atlantic Meridional Overturning Circulation at 26.5°N Cruise Report 53. Tech. rep., National Oceanography Centre Southampton.

Cunningham, S. A., Kanzow, T. O., Rayner, D., Barringer, M. O., Johns, W. E., Marotzke, J., Longworth, H. R., Grant, E. M., Hirschi, J. J.-M., Beal, L. M., Meinen, C. S., Bryden, H. L., 2007. Temporal variability if the Atlantic Meridional Overturning Circulation at 26.5°n. Science 317, 935–938.

Czaja, A., Marshall, J., 2005. The partitioning of poleward heat transport between the atmosphere and ocean. Journal of Atmospheric Sciences 63, 1498 – 1511.

de Szoeke, R. A., Chelton, D. B., 1999. The modification of long planetary waves by homogenous potential vorticity layers. Journal of Physical Oceanography 29, 500–511.

Deutsch, C., Hall, M. G., Bradford, D. F., Keller, K., 2002. Detecting a potential collapse of the North Atlantic thermohaline circulation before a point of no return: Implications for the design of an ocean observation system. In: EMF Summer Workshop "Climate Change Impacts and Integrated Assessment VIII", Snowmass, Colorado, July 27 August 7, 2002. URL `http://www.geosc.psu.edu/~kkeller`

Dewar, W. K., 1998. On 'too fast' baroclinic planetary waves in the general circulation. Physical Oceanography 28, 1739–1758.

Dickinson, R. E., 1978. Rossby waves - long-period oscillations of oceans and atmospheres. Annual Review of Fluid Mechanic 10, –195.

Dong, B. W., Sutton, R. T., 2001. The dominant mechanisms of variability in the Atlantic Ocean heat transport in a coupled ocean-atmosphere GCM. Geophysical Research Letters 28, 2445–2448.

Emery, W., Maagard, L., 1976. Baroclinic Rossby waves as inferred from temperature fluctuation in the eastern Pacific. Journal of Marine Research 34, 365–385.

Emery, W. J., Thompson, R. E., 1997. Data analysis methods in physical oceanography. Pergamon Press, Oxford.

Fillenbaum, E. R., Lee, T. N., Johns, W. E., Zantopp, R. J., 1997. Meridional heat transport variability at 26.5°N in the North Atlantic. Journal of Physical Oceanography 27, 153–174.

Fu, L. L., 2004. Latitudinal and frequency characteristics of the westward propagation of large-scale oceanic variability. Journal of Physical Oceanography 34, 1907–1921.

Fu, L. L., Chelton, D. B., 2001. Large Scale Ocean circulation. In: Fu, L., Cazenave, A. (Eds.), Satellite Altimetry and Earth sciences. Academic Press: San Diego, pp. 133–169.

Ganachaud, A., 2003. Error budgetof inverse box models: The North Atlantic. Journal of Atmospheric & Oceanic Technology 20, 1641–1655.

Ganachaud, A., Wunsch, C., 2000. Improved estimates of global ocean circulation, heat transport and mixing from hydrographic data. Nature 408, 453457.

Gill, A. E., 1982. Atmosphere-ocean dynamics. Academic Press, San Diego.

Gregory, J. M., Dixon, K. W., Stouffer, R. J., Weaver, A. J., Driesschaert, E., Eby, M., Fischefet, T., Hasumi, H., Hu, A., Jungclais, J. H., Kamenkovich, I. V., Levermann, A., Montoya, M., Murakami, S., Nawrath, S., Oka, A., Sokolov, A. P., Thorpe, R. B., 2005. A model intercomparison of changes in the atlantic thermohaline circulation response to increasing atmospheric co_2 concentrations. Geophysical Research Letters 32.

Hacker, P., Firing, E., Wilson, W. D., Molinari, R. L., 1996. Direct observations of the current structure east of the Bahamas. Geophysical Research Letters 23, 1127–1130.

Häkkinen, S., 2001. Variability in sea surface height: A qualitative measure for the meridional overturning in the North Atlantic. Journal of Geophysical Research 106, 13 837–13 848.

Hall, M. M., Bryden, H. L., 1982. Direct estimates and mechanisms of ocean heat transport. Deep-Sea Research 29, 339–359.

Halliwell, G., Cornillon, P., Byrne, D. A., 1991. Westward-propagating SST anomaly features in the Sargasso Sea. Journal of Physical Oceanography 21, 635–649.

Hill, K. L., Robinson, I. S., Cipollini, P., 2000. Propagation characteristics of extratropical planetary waves observed in the ATSR global sea surface temperature record. Journal of Geophysical Research 105, 927–945.

Hirschi, J., Killworth, P. D., Blundell, J. R., 2006. Subannual, seasonal and interannual variability of the north Atlantic meridional overturning circulation. Journal of Physical Oceanography 37, 1246–1265.

Hirschi, J. J.-M., Killworth, P. D., Blundell, J. R., Cromwell, D., 2009. Sea surface height signals as indicators for oceanic meridional mass transports. Journal Of Physical Oceanography 39 (3), 581–601.

Hirschi, J. M., Baehr, J., Marotzke, J., Stark, J., Cunningham, S. A., Beismann, J. O., 2003. A monitoring design for the Atlantic meridional overturning circulation. Geophysical Research Letters 30(7:1413), doi:10.1029/2002GL016776.

Horel, J. D., 1984. Complex Principal Component Analysis: Theory and Examples. Journal of Climate and Applied Meteorology 23, 1660–1673.

IPCC, 2001. Climate Change 2001: The scientific basis. Cambridge University Press: Cambridge, UK.

IPCC, 2007. Climate Change 2007: The Physical Science Basis. Contribution of Working Group I to the Fourth Assessment Report of the Intergovernmental Panel on Climate Change. Cambridge University Press: Cambridge, UK.

Jacobs, G. A., Hurlburt, H. E., Kindle, J. C., Metzger, E. J., Mitchell, J. L., Teague, W. J., Wallcraft, A. J., 1994. Decade-scale trans-Pacific propagation and warming effects of an El Niño anomaly. Nature 370, 360–363.

Jacobson, A. R., Spielberger, J. L., 1998. Observations of El Niño-Southern Oscillation induced Rossby waves in the northeast Pacific using in situ data. Journal of Geophysical Research 103, 24585–24596.

Jayne, S. R., Marotzke, J., 2001. The dynamics of ocean heat transport variability. Reviews of Geophysics 39, 385–411.

Johns, E., Fine, R. A., Molinari, R. L., 1997. Deep flow along the western boundary south of the Blake Bahama Outer Ridge. Journal of Physical Oceanography 27, 2187–2208.

Johns, W. E., Beal, L. M., Baringer, M. O., Molina, J., Cunningham, S. A., Kanzow, T., Rayner, D., 2008. Variability of shallow & deep watern boundary currents off the Bahamas during 2004-2005: First results from the 26°N RAPID-MOC array. Journal of Physical Oceanography 38, 605–623.

Johnson, H. L., Marshall, D. P., 2004. Global Teleconnections of Meridional Overturning Circulation Anomalies. Journal of Physical Oceanography 34, 1702–1722.

Kantha, L. H., Clayson, C. A., 2000. Numerical models of oceans and oceanic processes. Vol. 66 of International Geophysics Series. Academic Press: London.

Kanzow, T., Cunningham, S. A., Rayner, D., Hirschi, J. J.-M., Johns, W. E., Baringer, M. O., Bryden, H. L., Beal, L. M., Meinen, C. S., Marotzke, J., 2007. Observed Flow Compensation Associated with the MOC at 26.5 °N in the Atlantic. Science 317, 938–941.

Kanzow, T., Johnson, H., Marshall, D., Cunningham, S. A., Hirshi, J. J.-M., Mujahid, A., Bryden, H. L., 2009. Basin wide integrated volume transports in an eddy-filled ocean. Journal of Physical Oceanography Vol. 39 (12), 3091 3110.

Kanzow, T., Send, U., Zenk, W., Chave, A., Rhein, M., 2006. Monitoring the deep integrated meridional flow in the tropical North Atlantic: Long-term performance of a geostrophic array. Deep-Sea Research I 53, 528–546.

Killworth, P. D., Blundell, J. R., 1999. The effect of bottom topography on the speed and long extratropical planetary waves. Journal of Physical Oceanography 29, 2689–2710.

Killworth, P. D., Blundell, J. R., 2001. Large scale propagating disturbances: approximation by vertical normal modes. Journal of Physical Oceanography 31, 2852–2870.

Killworth, P. D., Blundell, J. R., 2003a. Long extra-tropical planetary wave propagation in the presence of slowly varying mean flow and bottom topography. Part i: The local problem. Journal of Physical Oceanography 33, 784–801.

Killworth, P. D., Blundell, J. R., 2003b. Long extra-tropical planetary wave propagation in the presence of slowly varying mean flow and bottom topography. Part ii: Ray propagation and comparison with observations. Journal of Physical Oceanography 33, 802–821.

Killworth, P. D., Blundell, J. R., 2004. The dispersion relation for Planetary waves in the presence of mean flow and topography. Part i: Ray analytical theory and one-dimensional examples. Journal of Physical Oceanography 34, 2692–2711.

Killworth, P. D., Blundell, J. R., 2005. The dispersion relation of planetary waves in the presence of mean flow and topography. part ii: Two-dimensional examples and global results. Journal of Physical Oceanography 35, 2110 2133.

Killworth, P. D., Chelton, D. B., de Szoeke, R., 1997. The speed of observed and theoretical long extra-tropical planetary waves. Journal of Physical Oceanography 27, 1946–1966.

Killworth, P. D., Cipollini, P., Uz, B. M., Blundell, J., 2004. Physical and biological mechanisms for planetary waves observed in sea-surface chlorophyll. Journal of Geophysical Research 109 (C07002), doi:10.1029/2003JC001768.

Kundu, P. K., 1990. Fluid mechanics. Academic Press, San Diego.

Kuo, H. L., 1973. Dynamics of quasigeostrophic flows and instability theory. Advances in Applied Mechanics 13, 330.

Lavin, A., Bryden, H. L., Parrilla, G., 1998. Meridional transport and heat flux variations in the subtropical North Atlantic. The Global Atmosphere and Ocean System 6, 269–293.

Lavin, A., Bryden, H. L., Parrilla, G., 2003. Mechanisms of heat, freshwater, oxygen and nutrient transports and budgets at 24.5°N in the subtropical North Atlantic. Deep-Sea Research I 50, 1099–1128.

Le Traon, P. Y., Nadal, F., Ducet, N., 1998. An improved mapping method of multisatellite altimeter data. Journal of Atmospheric and Oceanic Technologies 15, 522–533.

Le Traon, P. Y., Ogor, F., 1998. ERS-1/2 orbit improvement using T/P: The 2 cm challenge. Journal of Geophysical Research 103, 8045–8057.

LeBlond, P. H., Mysak, L. A., 1979. Waves in the ocean. Elsevier, Amsterdam.

Lee, T. N., Johns, W. E., Schott, F., Zantopp, R., 1990. Western boundary current structure and variability east of Abaco, Bahamas at 26.5°N. Journal of Physical Oceanography 20, 446466.

Lee, T. N., Johns, W. E., Zantopp, R. J., Fillenbaum, E. R., 1996. Moored observations of western boundary current variability and thermohaline circulation at 26.5°N in the subtropical North Atlantic. Journal of Physical Oceanography 26, 962983.

Liu, Z., 1999. Forced planetary wave response in a thermocline gyre. Oceanography 29, 1036–1055.

Longworth, H. R., 2007. Constraining variability of the Atlantic meridional overturning circulation at 26.5°N from historical observations. Ph.D. thesis, School of Ocean & Earth Science, University of Southampton, Southampton, U.K.

Manabe, S., Stouffer, R. J., 1988. Two stable equilibria of a coupled ocean-atmosphere model. Journal of Climate 1, 841–866.

Marotzke, J., 2000. Abrupt climate change and themohaline circulation: mechanism and predictability. Proceedings of the National Academy of Sciences 97(4), 1347–1350.

McPhaden, M. J., 1994. The eleven-year El-Nino? Nature 370, 326.

Mooers, C., Fiechter, J., 2005. Numerical simulations of mesoscale variability in the straits of florida. Ocean Dynamics 55, 309 – 325.

Mujahid, A., 2007. Vertical structure of propagating features. In: POETS Seminar Series. National Oceanography Centre, Southampton, U.K.

Mujahid, A., D., R., Bryden, H., 2008. Observational challenges in monitoring the atlantic meridional overturning circulation at 26.5 °N. In: Ocean Sensor, Warnemnde, Germany, 31st March 4th April 2008.

Nerem, R. S., Schrama, E. J., Koblinsky, C. J., Beckley, B. D., 1994. A preliminary evaluation of ocean topography from the TOPEX/POSEIDON mission. Journal of Geophysical Research 99, 565–583.

Pedlosky, J., 1987. Geophysical Fluid Dynamics., 2nd Edition. Springer-Verlag.

Platzman, G. W., 1968. The Rossby Wave. Quarterly Journal of the Royal Meteorological Society 94, 225–246.

Polito, P. S., Cornillon, P., 1997. Long baroclinic Rossby waves detected by TOPEX/POSEIDON. Journal of Geophysical Research 102, 3215–3235.

Polito, P. S., Liu, W. T., 2003. Global characterization of Rossby waves at several spectral bands. Journal of Geophysical Research 108, 3018.

Qiu, B., Miao, W., Muller, P., 1997. Propagation and decay of forced and free baroclinic Rossby waves in off-equatorial oceans. Journal of Physical Oceanography 27, 24052417.

Quartly, G. D., Cipollini, P., Cromwell, D., Challenor, P. G., 2003. Rossby waves: Synergy in action. Philosophical Transfers of the Royal Society London A 361, 57–63.

Rahmstorf, S., 2003. The current climate. Nature 421, 699.

Rahmstorf, S., 2006. Encyclopedia of Quarternary Sciences (Elias, S. A., Ed.). Elsevier, Amsterdam, Ch. Thermohaline Ocean Circulation, pp. 739–750.

Rahmstorf, S., Ganopolski, A., 1999. Long-term global warming scenarios computed with an efficient coupled climate model. Climate Change 43, 353–367.

Roemmich, D. H., Wunsch, C., 1985. Two transatlantic sections: Meridional circulation and heat flux in the subtropical North Atlantic Ocean. Deep-Sea Research 32, 619–664.

Rossby, C. G., 1939. Relation between variations in the intensity of the zonal circulation the atmosphere and the displacements of the semi-permanent centers of action. Journal of Marine Research 2, 38–55.

Schiermeier, Q., 30 November 2005 2005. Atlantic currents show signs of weakening: Research cruise reveals evidence of half-century of wane. Nature.

Schiermeier, Q., 2006. Climate change: A sea change. Nature 439, 256–260.

Stocker, T. F., 2000. Past and future reorganization in the climate system. Quarterly Science Reviews 19, 301–319.

Talley, L. D., 2003. Shallow, intermediate, and deep overturning components of the global heat budget. Journal of Physical Oceanography 33, 530–560.

Trenberth, K., Solomon, A., 1994. The global heat balance: heat transports in the atmosphere and ocean. Climate Dynamics 10, 107134.

Trenberth, K. E., Caron, J. M., 2001. Estimates of meridional atmosphere and ocean heat transports. Journal of Climate 14, 3433 – 3443.

UNESCO, 1983. Algorithms for computation of fundamental properties of seawater. United Nations Educational Scientific and Cultural Organization Technical Papers in Marine Science 44, 53.

Vellinga, M., Wood, R. A., 2002. Global climatic impacts of a collapse of the Atlantic thermohaline circulation. Climatic Change 54, 251267.

Wang, L., Koblinsky, C. J., 1995. Low-frequency variability in regions of the Kuroshio Extension and the Gulf Stream. Journal of Geophysical Research 100, 18313 18331.

Wang, L., Koblinsky, C. J., 1996. Annual variability of the subtropical recirculations in the North Atlantic and the North Pacific: A TOPEX/POSEIDON study. Journal of Physical Oceanography 26, 2462 2479.

Watts, D. R., Kontoyiannis, H., 1990. Deep-odean bottom pressure measurements: Drift removal and performance. Journal of Atmospheric & Oceanic Technology 7, 296–306.

White, W. B., 1977. Annual forcing of baroclinic long waves in the tropical North Pacific Ocean. Journal of Physical Oceanography 7, 50–61.

White, W. B., Chao, Y., Tai, C. K., 1998. Coupling of biennial oceanic Rossby waves with the overlying atmosphere in the Pacific basin. Journal of Physical Oceanography 28, 1236–1251.

Wood, R. A., Keen, A. B., Mitchell, J. F. B., Gregory, J. M., 1999. Changing Spatial Structure of the Thermohaline Circulation in Response to Atmospheric CO_2 Forcing in a Climate Model. Nature 399, 572 – 575.

Woodgate, R. A., 1994. Data Assimilation in Ocean Models. Ph.D. thesis, University of Oxford.

Wunsch, C., 2008. Mass and volume transport in an eddy-filled ocean. Nature Geoscience 1, 165–168.

Wüst, G., 1924. Florida- und Antillenstrom. Geographisch-naturwissenschaftliche Reihe 12, 48.

Zang, X. Y., Wunsch, C., 1999. The observed dispersion relationship for North Pacific Rossby wave motions. Journal of Physical Oceanography 29, 21832190.

Zantopp, R. J., Lee, T. N., Johns, W. E., 1989a. Technical Report 89-001: Moored current meter observations east of Abaco, The Bahamas (STACS-8 Array). Tech. rep., University of Miami.

Zantopp, R. J., Lee, T. N., Johns, W. E., 1989b. Technical Report 89-002: Moored current meter observations east of Abaco, The Bahamas (STACS-7 Array). Tech. rep., University of Miami.

Zantopp, R. J., Lee, T. N., Johns, W. E., 1990. Technical Report 90-002: Moored current meter observations east of Abaco, The Bahamas (STACS-10 Array). Tech. rep., University of Miami.

Zantopp, R. J., Lee, T. N., Johns, W. E., 1993. Technical Report 93-006: Moored current meter observations east of Abaco, The Bahamas (WATTS Array). Tech. rep., University of Miami.

Zantopp, R. J., Lee, T. N., Johns, W. E., 1996. Technical Report 96-001: Moored current meter observations east of Abaco, The Bahamas (ACCP-1 Array). Tech. rep., University of Miami.

Zantopp, R. J., Lee, T. N., Johns, W. E., 1998a. Technical Report 98-005: Moored current meter observations east of Abaco, The Bahamas (ACCP-2 Array. Tech. rep., University of Miami.

Zantopp, R. J., Lee, T. N., Johns, W. E., 1998b. Technical Report 98-006: Moored current meter observations east of Abaco, The Bahamas (ACCP-3 Array. Tech. rep., University of Miami.